NASA CONTRACTOR REPORT

NASA CR-2217

ANALYTICAL METHOD FOR PREDICTING THE PRESSURE DISTRIBUTION ABOUT A NACELLE AT TRANSONIC SPEEDS

by J. S. Keith, D. R. Ferguson, C. L. Merkle, P. H. Heck, and D. J. Lahti

Prepared by
GENERAL ELECTRIC COMPANY
Cincinnati, Ohio 45215
for Langley Research Center

NATIONAL AERONAUTICS AND SPACE ADMINISTRATION • WASHINGTON, D. C. • JULY 1973

1. Report No. NASA CR-2217	2. Government Accession No.	3. Recipient's Catalog No.
4. Title and Subtitle Analytical Method for Predicting the Pressure Distribution About a Nacelle at Transonic Speeds		5. Report Date July 1973
		6. Performing Organization Code
7. Author(s) J.S. Keith, D.R. Ferguson, C.L. Merkle, P.H. Heck, D.J. Lahti		8. Performing Organization Report No.
		10. Work Unit No.
9. Performing Organization Name and Address General Electric Company Aircraft Engine Group Cincinnati, Ohio		11. Contract or Grant No. NAS1-10804
		13. Type of Report and Period Covered Final Report
12. Sponsoring Agency Name and Address National Aeronautics and Space Administration Langley Research Center Hampton, Virginia		14. Sponsoring Agency Code
15. Supplementary Notes		

16. Abstract

This report describes the formulation and development of a computer analysis for the calculation of streamlines and pressure distributions around two-dimensional (planar and axisymmetric) isolated nacelles at transonic speeds. The computerized flow field analysis is designed to predict the transonic flow around long and short high-bypass-ratio fan duct nacelles with inlet flows and with exhaust flows having appropriate aerothermodynamic properties. The flow field boundaries are located as far upstream and downstream as necessary to obtain minimum disturbances at the boundary. The far-field lateral flow field boundary is analytically defined to exactly represent free-flight conditions or solid wind tunnel wall effects.

The inviscid solution technique is based on a Streamtube Curvature Analysis. The computer program utilizes an automatic grid refinement procedure and solves the flow field equations with a matrix relaxation technique. The boundary layer displacement effects and the onset of turbulent separation are included, based on the compressible turbulent boundary layer solution method of Stratford and Beavers and on the turbulent separation prediction method of Stratford.

This computer program has the capability of calculating the pressure distributions and flow fields, including viscous displacement effects, on a variety of internal and external shapes. The location of incipient turbulent boundary layer separation is identified, if and when the calculated pressure gradients are sufficient to cause it. The computing times are relatively short (2-6 minutes on a CDC 6600) depending on the complexity of the problem. The predicted pressure distributions have been compared with the through-flow nacelle test results from the NASA-Langley 16-foot tunnel.

17. Key Words (Suggested by Author(s)) Streamtube Curvature Computer Program Inlets, Nacelles, Transonic Flow Viscous Flow, Separation	18. Distribution Statement		
19. Security Classif. (of this report) Unclassified	20. Security Classif. (of this page) Unclassified	21. No. of Pages 156	22. Price* $3.00

TABLE OF CONTENTS

TABLE OF CONTENTS (Concluded)

LIST OF ILLUSTRATIONS

LIST OF ILLUSTRATIONS (Continued)

LIST OF TABLES

SUMMARY

This report describes the formulation and development of a computer analysis for the calculation of streamlines and pressure distributions around two-dimensional (planar and axisymmetric) isolated nacelles at transonic speeds. The computerized flow field analysis is designed to predict the transonic flow around long and short high-bypass-ratio fan duct nacelles with inlet flows and with exhaust flows having appropriate aerothermodynamic properties. The flow field boundaries are located as far upstream and downstream as necessary to obtain minimum disturbances at the boundary. The far-field lateral flow field boundary is analytically defined to exactly represent free-flight conditions or solid wind tunnel wall effects.

The inviscid solution technique is based on a Streamtube Curvature Analysis. The computer program utilizes an automatic grid refinement procedure and solves the flow field equations with a matrix relaxation technique. The boundary layer displacement effects and the onset of turbulent separation are included, based on the compressible turbulent boundary layer solution method of Stratford and Beavers and on the turbulent separation prediction method of Stratford.

This computer program has the capability of calculating the pressure distributions and flow fields, including viscous displacement effects, on a variety of internal and external shapes. The location of incipient turbulent boundary layer separation is identified, if and when the calculated pressure gradients are sufficient to cause it. The computing times are relatively short (2-6 minutes on a CDC 6600) depending on the complexity of the problem. The predicted pressure distributions have been compared with the through-flow nacelle test results from the NASA-Langley 16-foot tunnel.

ANALYTICAL METHOD FOR PREDICTING THE PRESSURE DISTRIBUTION ABOUT A NACELLE
AT TRANSONIC SPEEDS

PART I - STREAMTUBE CURVATURE ANALYSIS
J.S. Keith, D.R. Ferguson, C.L. Merkle, and P.H. Heck
General Electric, Aircraft Engine Group
Evendale, Ohio   45215

1.0 INTRODUCTION

Aircraft are being designed with the NASA-developed supercritical wing
to fly at cruise Mach numbers approaching one. The need for low-installed
drag and high-drag-divergence Mach number nacelle installations is extremely
critical to the success of this design. Design techniques are required to
evaluate these nacelles on an isolated basis and then on an installed or
integrated basis.

For this reason NASA has begun a program to provide design information
for low-drag, high-drag-divergence Mach number isolated nacelles suitable
for use with advanced high-bypass-ratio turbofan engines. One element of
such a program is the development of a method to predict the inviscid pres-
sure distribution and flow field about an arbitrary axisymmetric ducted body
at transonic speeds. The prediction technique will provide the means to
conduct parametric studies so that the nacelle design criteria could be
evaluated to select configurations for further experimental investigations.
The prediction technique would provide guidance during wind tunnel testing
to develop nacelle shapes which would minimize drag within given design
restraints.

Several techniques of solving the inviscid equations of motion about
arbitrary two- or three-dimensional bodies at transonic speeds are presently
available; however, there are no computer programs available which treat air
inlet or nacelle configurations. The objective of the development of this
computer analysis was the prediction of flow fields about isolated nacelles
at transonic conditions. The solution technique was further specified to
give accurate results consistent with the requirement of relatively short
computing time per input case as compared to that required for a time-
dependent finite difference method of solution. The method utilized to com-
pute the flow field is the Streamtube Curvature Relaxation technique.

The Streamtube Curvature Method (STC) of solving planar and axisym-
metric external flows has not been discussed significantly in the literature;
however, the method is a very natural one. For example, engineers frequently
rely on one-dimensional compressible flow relationships for a first-order
solution to ducted flows. The STC approach is similar except that a number
of confluent streamtubes, with slightly different properties, are added to-
gether to obtain the total flow in the channel. Each streamtube is handled
in much the same way as is the one streamtube in the one-dimensional problem.
In the limit, as the size of the individual streamtubes approaches zero, the
STC method satisfies the inviscid equations of motion exactly.

This report describes the method of analysis used to apply the Stream-tube Curvature Relaxation technique, the numerical procedure for computer-ization of the analysis, and examples of correlations of predicted flow fields on nacelles at transonic speeds with wind tunnel test data.

The computer program source deck, together with a user's manual, is available from COSMIC (Computer Softwear and Information Center), Burrows Hall, University of Georgia, Athens, Georgia 30601. The program is written in CDC Fortran 2.3 source language, except for three subroutines in Compose 1.1 language. The computer program has been checked out for the CDC 6600 machine.

2.0 SELECTION OF THE METHOD

Known methods for solving transonic flow fields may be divided into two categories -- time-dependent and iterative. Time-dependent methods have achieved much popularity because both the subsonic and supersonic portions of the flow field, in most cases, are solved by the same algorithm. Thus, with a rather simple calculating procedure a difficult mathematical problem is computed. In the iterative method, however, the calculation formula must reflect the mathematical nature of the equation and a switching, depending upon Mach number, to the appropriate formula is required at each calculation point. It is in this way that the different physical characteristics of the subsonic and supersonic regions come into play.

Iterative methods are quite new. To the authors' knowledge, the first demonstration of a general, numerically consistent, iterative method for solving transonic flows occurred in 1970 (ref. 1). This was the small perturbation method of Murman and Cole for flow past airfoils without lift. Recently, extensions to the method have been presented by Stegger and Lomax (ref. 2).

Although there undoubtedly are many variations, we may think of an iterative method as one in which the equation for the unknown fluid dynamic property at each of the net points is solved by: (1) writing a linear approximation to this equation and, (2) solving the resulting system of equations simultaneously. Because of the linear approximation, this process is repeated several times (say 3 to 10) before convergence is obtained.

In contrast to solving the field simultaneously, time-dependent methods compute the wave motion of a disturbance as it travels from one part of the flow field to the other. A steady-state result is obtained only after all wave reflections have dissipated to a relatively small level. Although the time-dependent method of updating the flow properties can be likened to an iteration process, clearly the most rapid solution will be obtained when the flow field variables are all corrected simultaneously and when this correction is not limited by (computationally) slow wave transits. Therefore, as a rapid analysis tool, the iterative method is most attractive.

Of the many different representations of the fluid dynamic equations, the number which can be solved by the iterative method across the transonic region are, perhaps, limited. Here the simplest and most general forms of the equations are chosen, namely, those which apply along streamlines (Ψ = constant lines) and those which apply along lines which are orthogonal to the streamlines (ξ = constant lines).

Across the streamlines, the continuity and momentum equations are:

Continuity:

$$\partial A = \frac{\partial \Psi}{\rho V} \qquad\qquad (\xi = \text{Const}) \qquad (1)$$

3

Momentum:

    (a) Normal form:

$$\frac{\partial p}{\partial n} = C\rho V^2 \qquad\qquad (\xi = \text{Const}) \qquad (2a)$$

    (b) Crocco form:

$$\frac{1}{2}\frac{\partial(V^2)}{\partial n} = -CV^2 + \frac{\partial H}{\partial n} - T\frac{\partial S}{\partial n} \qquad (\xi = \text{Const}) \qquad (2b)$$

Along the streamlines the energy and momentum equations are:

Momentum:

$$\frac{DS}{Ds} = 0 \qquad\qquad (\Psi = \text{Const}) \qquad (3)$$

Energy:

$$\frac{DH}{Ds} = 0 \qquad\qquad (\Psi = \text{Const}) \qquad (4)$$

where, the independent variables s and n are the distances measured along and across the streamlines, respectively.

The solution method is an extension of the streamline curvature method. It may be briefly described as follows: First, a crude grid of streamlines and orthogonal lines is assumed (refer to Figure 1); second, the curvature of the streamlines at each of the grid points is evaluated; third, the momentum equation is integrated along a line normal to the streamlines to obtain velocity, and the continuity equation is integrated to determine the "correct" streamline positions (for the assumed curvature field). These are indicated by the "x" in Figure 1. Fourth, an adjustment (δn) is computed by considering: (1) the difference between the computed and assumed streamline positions and, (2) the effect of the implied curvature modification in the integrated momentum equation. Finally, the streamlines are repositioned by the δn values.

Because the movement of any one grid point alters the velocity at nearby points through a change in curvature, it is highly desirable to account for these interrelating point adjustments simultaneously. The utilization of a simultaneous solution procedure, employed here, is not part of the classical streamline curvature method (refs. 3, 4, 5). In comparison, the classical method yields calculation times which are very slow, especially for a closely spaced calculation grid. In concept, the set of simultaneous equations for the normal streamline adjustments is formulated from the finite difference equivalent of the following equation:

4

1. Assume a Crude Grid
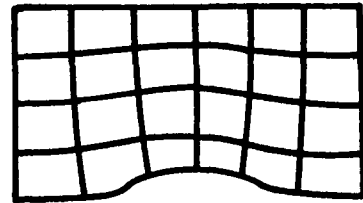
2. Evaluate Curvature
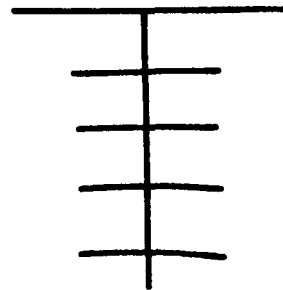
3. Integrate the Cross-Stream
    Momentum Equation and the
    Continuity Equation to Determine
    the "Correct" Streamline Positions.
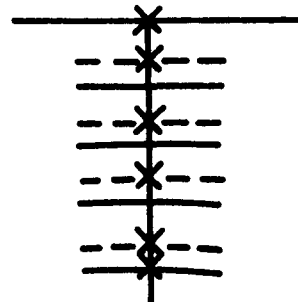
4. Solve the Matrix Equation for
    δn and Move the Grid Points.

Figure 1. Solution Technique.

$$\frac{\partial^2(\delta n)}{\partial \Psi^2} + \frac{(1-M^2)}{(\rho V)^2} \frac{\partial^2(\delta n)}{\partial s^2} = F \qquad (5)$$

where:

δn = Required streamline adjustment in the normal direction

Ψ = Stream function

s = Curvilinear distance along a given streamline

M = Mach number

ρV = Flow per unit area

F = Driving (or error) function derived from the solution to the integral continuity and normal momentum equations

This equation is derived in Appendix A for the special case of isentropic two-dimensional flow. (These limiting assumptions are utilized only to maintain simplicity of illustration; they are not part of the computer program.) From a mathematical point of view, the above equation is similar to the small perturbation form of the velocity potential equation employed by Murman and Cole (ref. 1).

$$\frac{\partial^2 \phi}{\partial y^2} + (1-M^2) \frac{\partial^2 \phi}{\partial x^2} = 0 \qquad (6)$$

$$\frac{v}{a} \ll 1, \quad M \approx \frac{u}{a}$$

In either case, it is possible to numerically solve the equations for either subsonic flow or supersonic flow by changing the finite difference star from a subsonic representation to a supersonic representation as illustrated in Figure 2. Notice that the supersonic representation includes no points downstream of the cross-stream line, reflecting the physical reality that disturbances downstream will not be felt upstream. The star-switching process is directly related to the coefficient $(1-M^2)$; and, because this coefficient is zero at unity Mach number, the switch from one star to the other is performed smoothly.

The extended streamline curvature method, here referred to as the Streamtube Curvature (STC) method, appears to have the advantage that it is applicable to the calculation of nonsmall perturbation transonic flows. Considerable complexity is introduced when Equation 6 is expanded to allow the vertical component of velocity, v, to be the order of magnitude of the axial component u. In this case when the grid system is not aligned with the flow direction, a cross-derivative term:
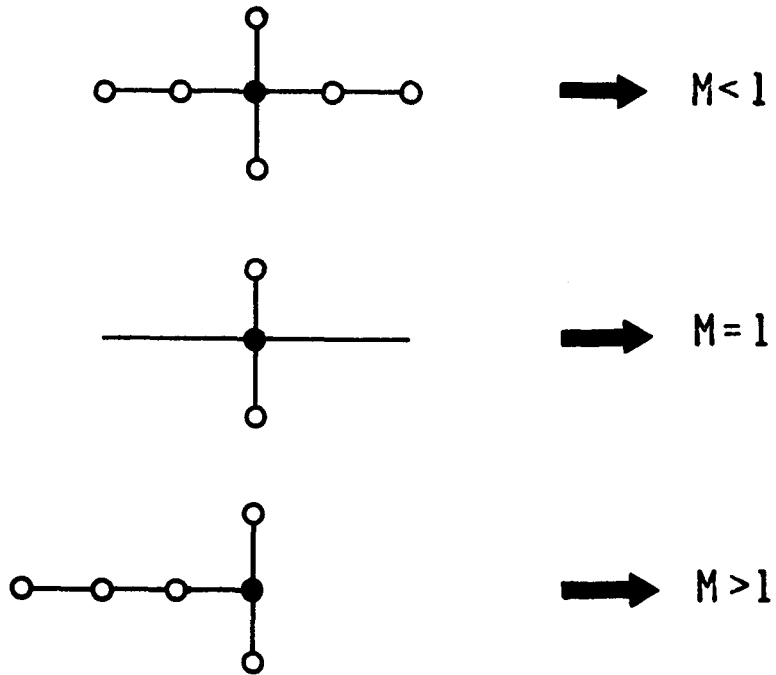
Figure 2. Finite Difference Stars for Subsonic
and Supersonic Flow.

$$\frac{uv}{a^2} \frac{\partial^2 \phi}{\partial x \partial y}$$

appears in the differential equation, and the star-switching concept (as explained above) cannot be applied. On the other hand, with the intrinsic coordinate system utilized in the STC procedure, the arms of the star are always oriented in the streamwise and cross-stream directions, and the star-switching algorithm is always appropriate.

Star switching is one of the requirements for the numerical solution to either Equations 5 or 6 in a mixed subsonic and supersonic region. A second requirement is a reasonably accurate evaluation of the nonlinear coefficient term $(1-M^2)$. In this respect, the velocity potential method is superior. During the current contract, it has been found that the coefficient term in the differential equation (Equation 5 above) cannot readily be evaluated to the accuracy necessary for a convergent transonic solution when the streamwise spacing between the calculation points is too small. This evidently is due to the method used for evaluating the velocity (and Mach number) at field mesh points. The velocity calculation, using Equation 2b, requires the evaluation of curvature by a second-order numerical differentiation which is subject to large errors (order of $1/\Delta S^2$) when the streamwise spacing (ΔS) is small.

Aside from the limitation just cited, the streamtube curvature method is extremely powerful as indicated by the following features:

● No additional complexities arise when the flow is rotational.

● The slip line between an exhaust jet and the external flow can be handled precisely. (The procedure is to consider two coincident streamlines. Their position and pressure are the same; their velocity and stagnation properties may be different.)

● The streamline/orthogonal line grid provides a mapping of the flow field into a rectangular domain. This is helpful from the standpoint of computer program organization.

The STC Program has also been designed to:

● Handle multiple streams

● Place grid points at locations in the flow field where they are needed, as determined by local variations of the dependent variables

● Allow external flow analysis by incorporating matched near-field and far-field solutions. The far-field solutions are obtained analytically utilizing small perturbation theory.

3.0 AN OUTLINE OF THE CALCULATION STEPS

The operations performed by the STC Program may be outlined as follows:

1. Define the flow regions and locate (approximately) the "primary" orthogonals and the streamlines which divide the internal and external flows.

2. Refine the grid as required by inserting additional streamlines and orthogonal lines between those already existing.

3. Compute the streamline angles and curvatures.

4. Compute the orthogonal line angles and move the grid points along the streamlines to obtain orthogonality.

5. Compute the velocities on the "far-field" boundary.

6. Adjust the flow rates in the exhaust streams, if any, to meet the calculated choking flow rate.

7. Integrate along each orthogonal the momentum and continuity equations (Equations 1 and 2).

8. Determine if the streamline positions are within a "rough tolerance." If so, return to Step 2 for additional grid refinement (unless grid refinement limits have already been reached). Otherwise, continue to Step 9.

9. Determine if the streamline positions are within final tolerance. If so, jump to Step 13. Otherwise continue to Step 10.

10. Set up the matrix equation for the streamline correction, δn.

11. Solve the matrix equation.

12. Modify the streamline positions by δn, and return to Step 3.

13. Calculate and print the output quantities; then return to Step 1 for the next case, if any.

The first operation includes reading the card input for a description of the geometry and flow properties. The computer program has been written to have general capability for analyzing a great variety of configurations. The first step in the programmed logic is to develop a table of orthogonals or calculation stations for each of the several flow regions. The regions are determined as illustrated in Figure 3, so the calculation can proceed from upstream to downstream. The boundary of each region is defined as a primary orthogonal. As shown in Figure 4, the initial grid which is developed contains only the primary orthogonals and the double streamlines which separate the various streams.
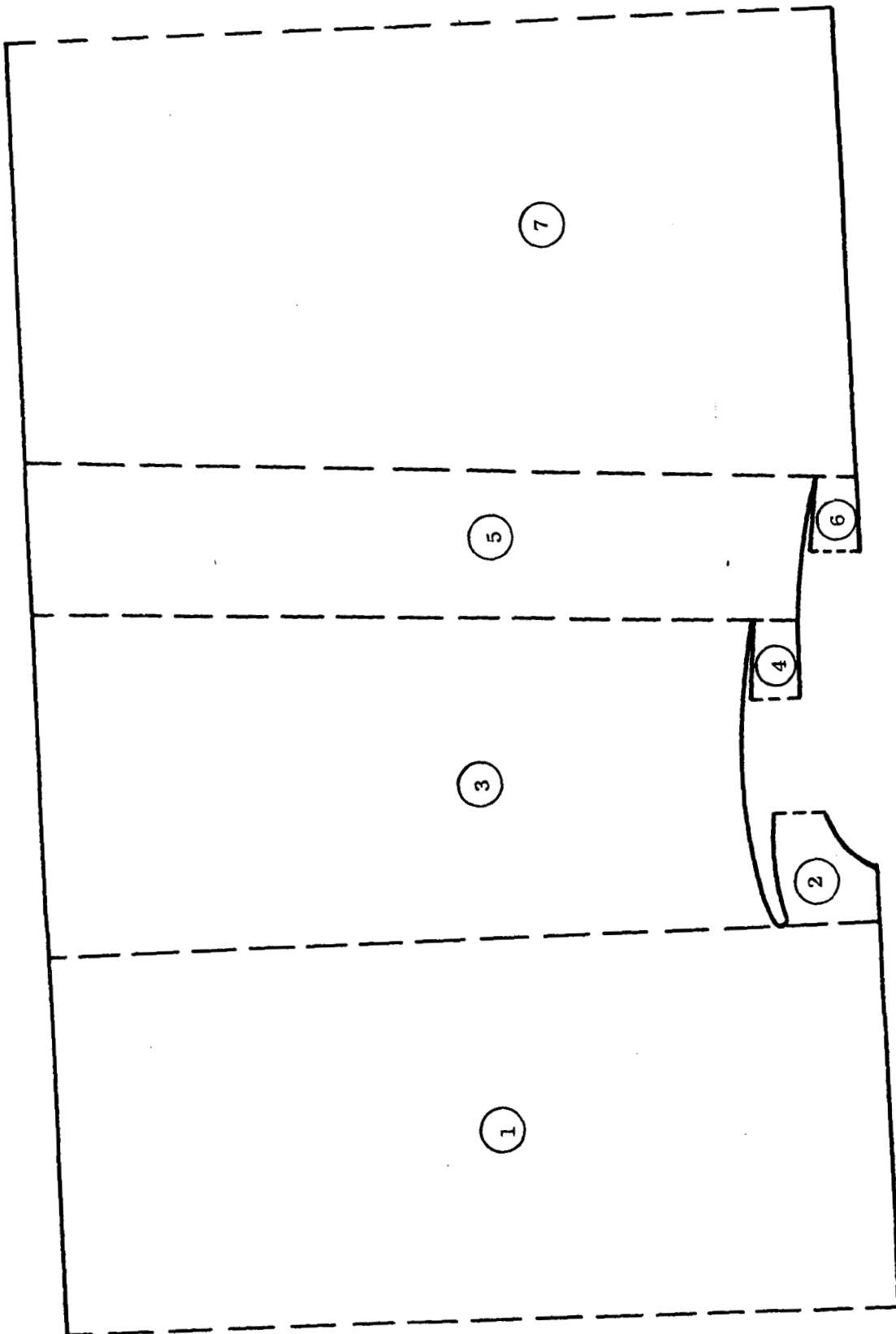
Figure 3. Subdivision of the Flow Field into Regions.

10

Primary Orthogonals

External Flow
Channel

Dividing Streamlines
Between Channels

Bypass Jet

Primary Jet

Inlet Channel
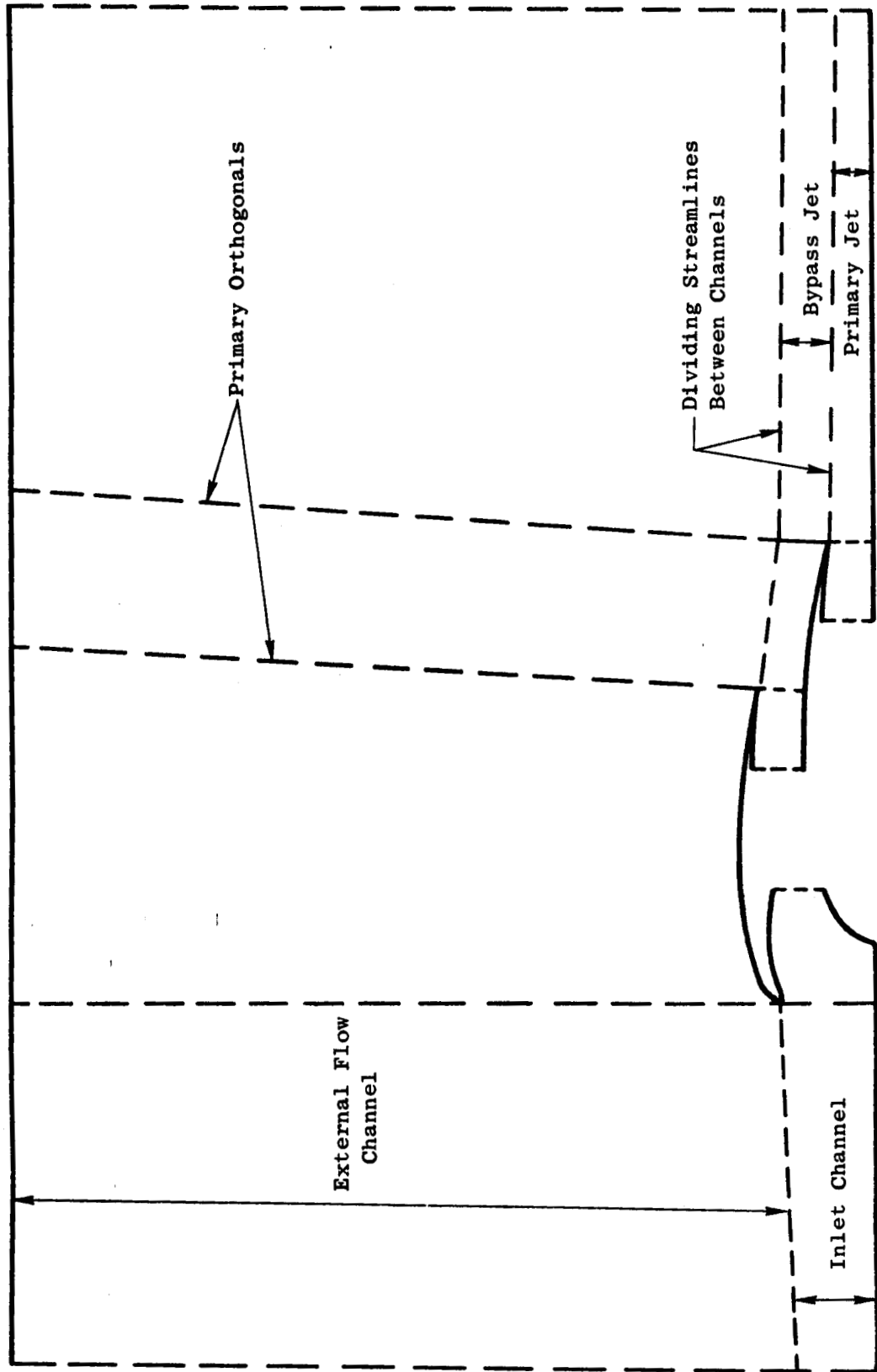
Figure 4. Initial Streamline/Orthogonal Grid Before the First Refinement.

11

The second step in the computational procedure is the grid refinement. The very crude grid, obtained in Step 1, is refined before the first solution of the flow field equations is executed. A new orthogonal is placed within each region and, likewise, a streamline is inserted in the middle of each channel. In the external channel, additional streamlines are placed close to the body. After the solution has been obtained for this net, the grid intervals are halved as required. This may be likened to the steps taken when one "flux plots" a flow field by hand. First, major flow lines and normals are sketched in, and then more and more streamlines and orthogonal lines are added until the desired resolution is obtained. At each step in the process, the positions of the lines are adjusted to meet the correct solution requirements. The procedure automatically provides for grid refinement in regions of high curvature and high acceleration or deceleration. The streamline and orthogonal lines which are added between existing lines are not required to span the field if only local refinement, near the body, is required. The refinement procedure presently built into the program uses a criteria involving the distance and velocity increment between grid points. These refinement criteria are discussed in detail in Reference 16.

The third step in the method is to determine the angles and curvatures of the streamlines at each grid point. For subsonic portions of the flow field, this is performed by fitting a piecewise continuous cubic polynominal in a coordinate system which is locally rotated for each interval. The resulting fit is analogous to the curve produced by a beam which is loaded by discrete forces to pass through the given grid points. The locally rotated coordinate system removes the restriction that requires the slope to be small. For grid points located in a supersonic region, backward difference formulas are employed. Either 3-point or 4-point formulas may be optionally selected. Again the coordinate system is rotated so that slopes in the curve-fitting coordinate system are small.

In the fourth step, the orthogonality of the grid points is checked and points are moved along the spline curve as required to achieve normal intersections between the two sets of lines. Also, the normal distance, n, is computed for each grid point as measured from the lower boundary of the orthogonal.

When the initial grid is set up, a boundary is placed some distance away from the body. This boundary becomes the interface between the near-field and the far-field solutions. The near-field is computed by the stream-tube curvature method, and the far-field is computed by linear small perturbation theory. In the process of iterating, this boundary (which is also a streamline) will float so that its shape and velocity distribution are matched by both the inner and outer solutions. In practice, the shape of the interface streamline (also referred to as the far-field boundary) is first assumed. Using the far-field equations, the velocity distribution is calculated. This is Step 5. These velocities are subsequently employed in the near-field analysis and from this comes a revised shape for the interface streamline. Revised velocities will then be computed in Step 5 during the following iteration cycle, and so forth.

12

Step 6 is the modification, as required, of the flow rates of the exhaust streams. For boattail analysis of nacelles, the internal geometry of the exhaust passage is required input to the STC program. Because of streamline curvature effects, the discharge coefficient for the nozzle will be somewhat less than unity. The user, however, may input a flow rate based on unity discharge flow coefficient or, for that matter, any approximate value. Determination of the velocity distribution across the throat of the nozzle will be determined within the STC framework, and the evaluation of the maximum "choked" flow rate is Step 6 of the calculation procedure.

Step 7 is the solution of the flow field equations per se. This section of the program is referred to as the "flow balance;" Equations 1 and 2 are integrated. In the external regions of the field, the momentum equation is integrated from the far-field interface boundary to the body (or to the centerline or lower boundary, whichever exists). The integral form of the momentum equation is:

$$\ln V_k{}^2 - \ln V_N^2 = 2 \int_{n_k}^{n_N} C \, dn \tag{7}$$

where:

V_N = Velocity as determined in Step 5 along the far-field streamline

V_k = Velocity at any streamline with orthogonal distance n_k

n_N = Distance measured along the orthogonal to the far-field streamline

Although not reflected in Equation 7, the effect of varying total pressure behind a shock wave is also included. The method for handling this is presented in Section 5.5. Also, if a slip-line occurs in the field, the velocity jump equations

$$P_S = P_{T+} \left(\frac{T_{S+}}{T_{T+}} \right)^{\frac{\gamma}{\gamma - 1}} = P_{T-} \left(\frac{T_{S-}}{T_{T-}} \right)^{\frac{\gamma}{\gamma - 1}} \tag{8a}$$

$$\left(C_{p+} T_{T+} \right) + \frac{V_+^2}{2} = H_+ \tag{8b}$$

$$\left(C_{p-} T_{T-} \right) + \frac{V_-^2}{2} = H_- \tag{8c}$$

are employed where the subscripts (+) and (−) denote conditions on the streamlines above and below the slip-line, respectively.

The velocity, total temperature, and total pressure allow determination of the density at each grid point, and the inverse product of density and velocity is integrated to find flow area.

$$A_2 - A_1 = \int_{\Psi_1}^{\Psi_2} \frac{\partial \Psi}{\rho V} \tag{9}$$

The cumulative flow areas calculated by Equation 9 are compared with the geometric areas of the streamlines used in Step 3. The difference between these two values is used as a convergence check (Steps 8 and 9) and in the streamline correction equation, Step 10.

For internal flow orthogonals, the velocity at the outer boundary (V_{FF} in Equation 7) is not known. Instead, an iteration process is employed whereby the outer boundary velocity is varied to obtain a match in the calculated geometric passage area.

In Steps 10 and 11, the proper adjustment of the streamline positions is determined; and, in Step 12, the grid points are moved in the normal direction by this computed adjustment.

The iterative sequence is to start with a crude grid, as noted above, and to repeat Steps 3 through 12 until the flow balance error is small. This is often accomplished in one or two iterations. The grid is then refined to the next level, and the field is reconverged. The refinement/convergence process is continued until the grid refinement criteria is satisfied, or alternately, until computer storage limits are reached. At this point, additional loops through Steps 3 to 12 may be performed until the flow balance error is satisfactory.

In the next section, examples are shown of STC predictions; and, in Section 5, the details of the numerical procedures are presented.

4.0 EXAMPLE RESULTS

4.1 SHORT DUCT FAN INSTALLATION

The development of this computer analysis has been addressed to transonic pressure distributions on typical jet engine installations in isolated nacelles. The analysis was required to handle inlet flows and exhaust flows with correct aerothermodynamic properties. An example which demonstrates the capabilities is the short duct fan installation.

The installation and the predicted flow field at $M_O = 0.5$ are shown in Figure 5. Four flows are present in this example: 1) the free-stream or external flow at $M_O = 0.5$, 2) the inlet flow for a mass-flow ratio of 1.0, 3) the fan nozzle flow, and 4) the core nozzle flow. The fan nozzle and core nozzle flow have temperature and pressure profiles typical of this type of jet engine.

The details of the fan nozzle flow at a supercritical nozzle pressure ratio are shown in Figure 6. The external flow is at $M_O = 0.02$ to represent a near-static nozzle expansion. The radial shifting of the streamlines due to flow curvature is very evident.

4.2 TWO-DIMENSIONAL INLET

The two-dimensional inlet with the ramp adjacent to the aircraft fuselage (typical of two-dimensional fighter-type inlet with boundary layer bleed) is shown in Figure 7. The flow field for this inlet was calculated with three flows. The initial free-stream Mach number was $M_O = 0.8$. The inlet flow was choked at the inlet throat.

The pressure distribution on the external surface of the cowl is shown in Figure 8. The maximum surface Mach number was 0.998.

The pressure distributions on the ramp and the upper wall of the inlet are plotted in Figure 9. The local Mach numbers exceed unity as the ramp turns toward the axial direction in the throat. The walls downstream of the throat were defined as straight in this example, and the pressure levels show uniform flow at Mach = 1.0.

4.3 DATA COMPARISONS - AXISYMMETRIC INLETS

The NASA inlet No. 8 (NASA 1-85-100), with an internal contraction ratio of $A_{HL}/A_{Throat} = 1.093$, was selected as the configuration for data comparisons. This inlet represents a typical flight-type installation for high transonic flight Mach numbers. The geometry consists of a NACA 1 series external contour with an $x/D_{max.} = 1.0$ and a $D_{HL}/D_{max.} = 0.8535$ as shown in Figure 10. The projected area distributed is shown in Figure 11. This inlet was tested in the 16-foot transonic wind tunnel at NASA-Langley.
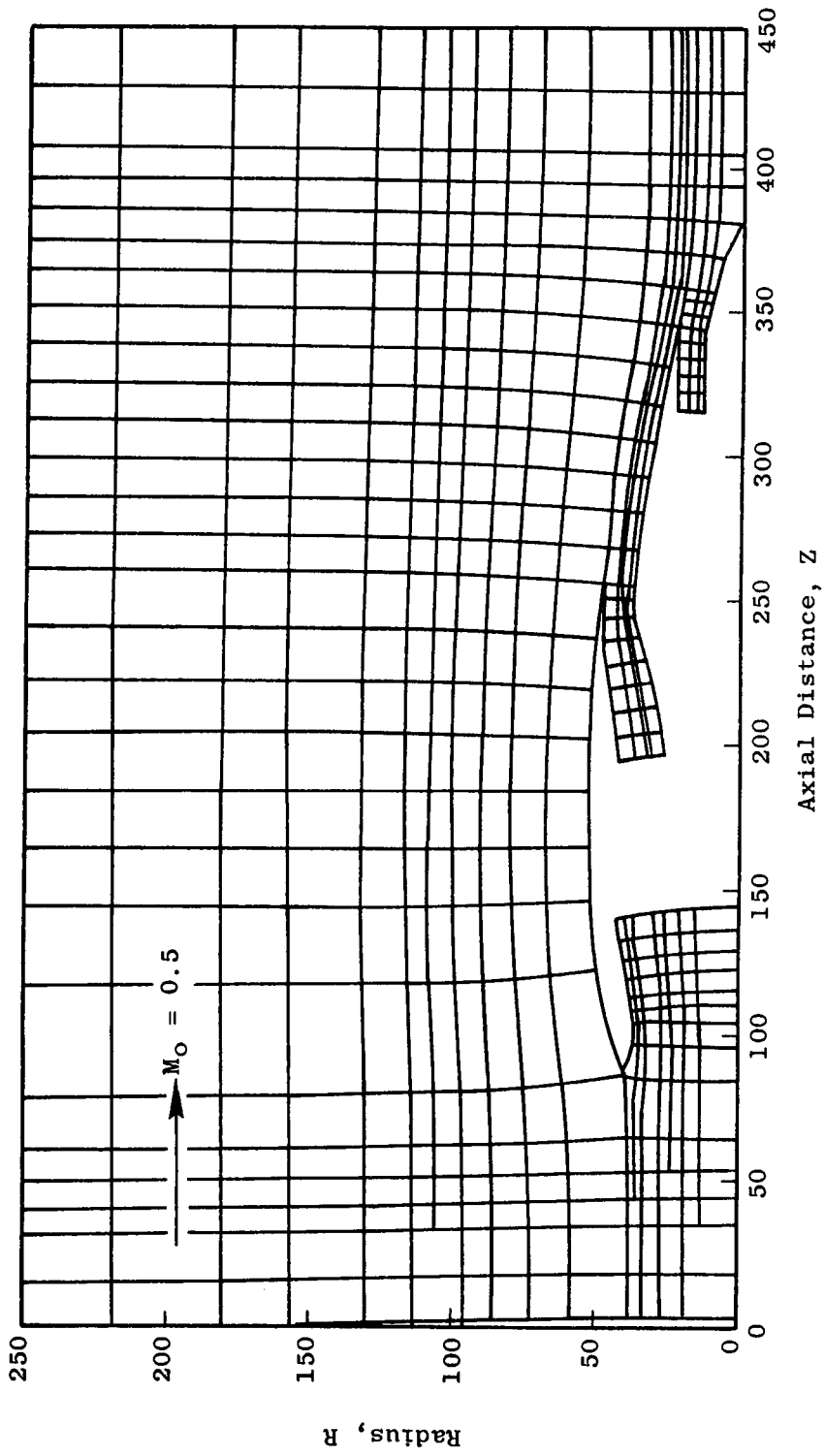
Figure 5. Short Duct Fan Installation Flow Field.

Axial Distance, Z

Radius, R

$M_O = 0.5$
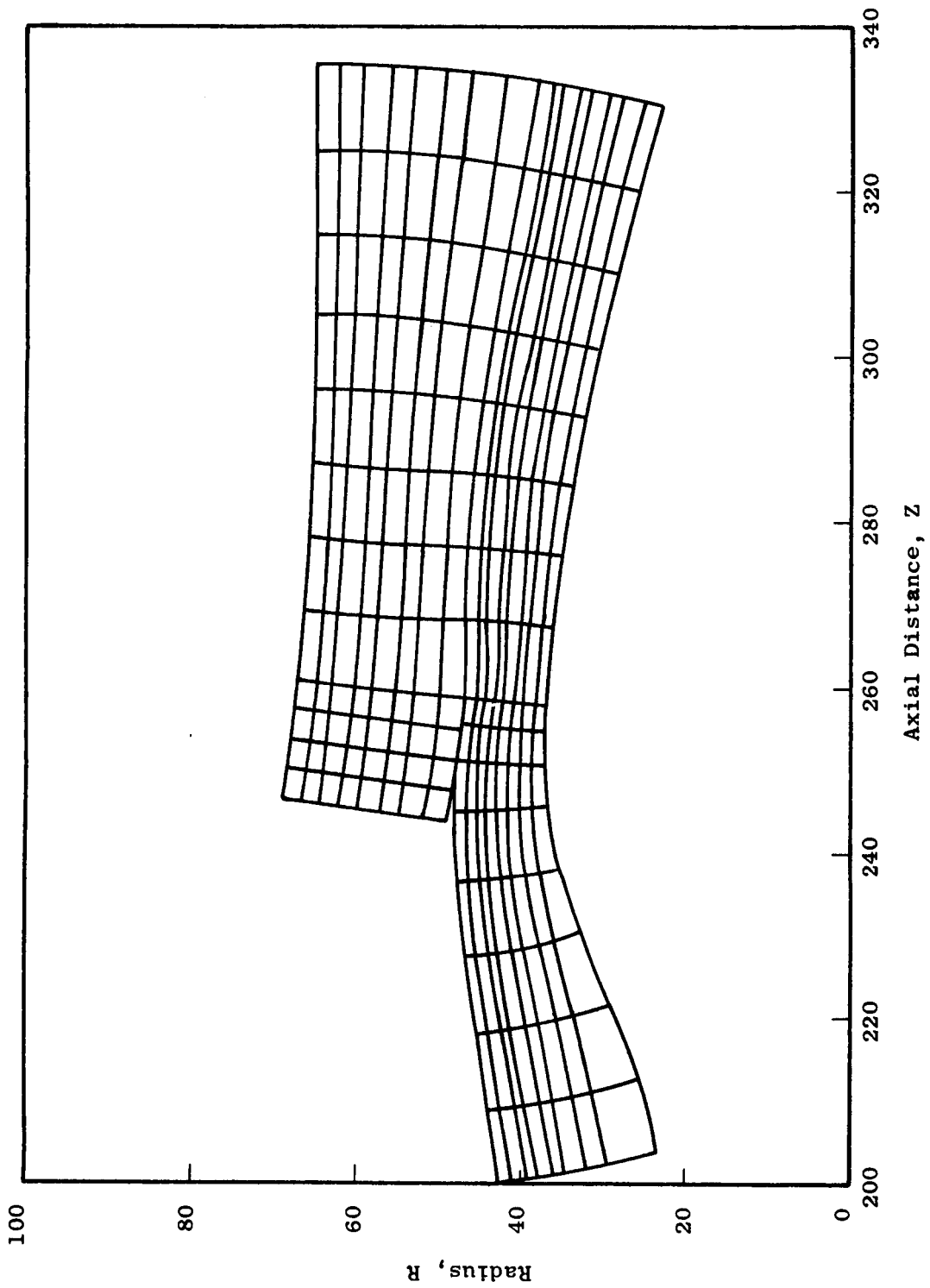
Figure 6. Fan Nozzle Flow, Supercritical Nozzle Pressure Ratio.

17
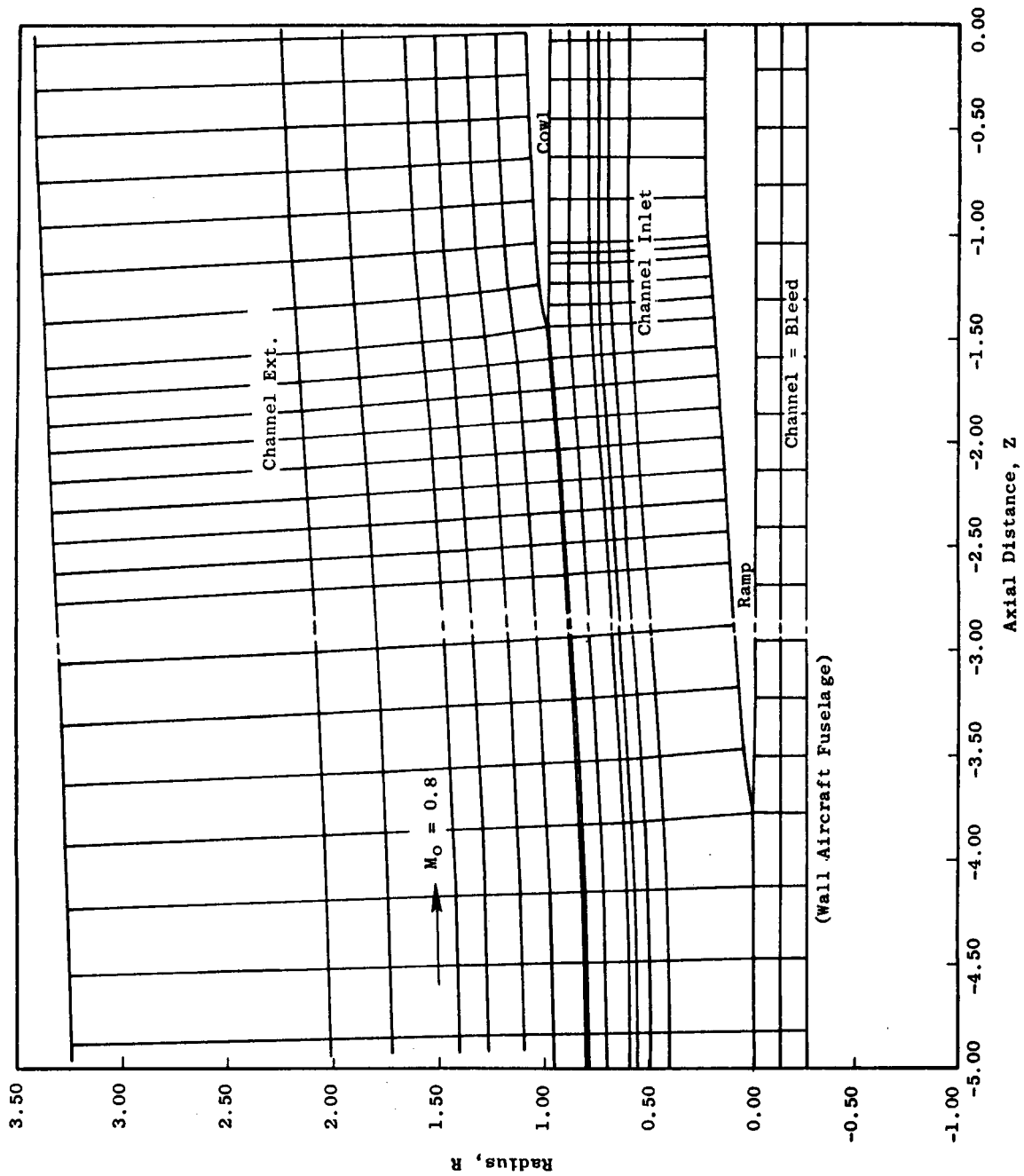
Figure 7. Two-Dimensional (Planar) Inlet.
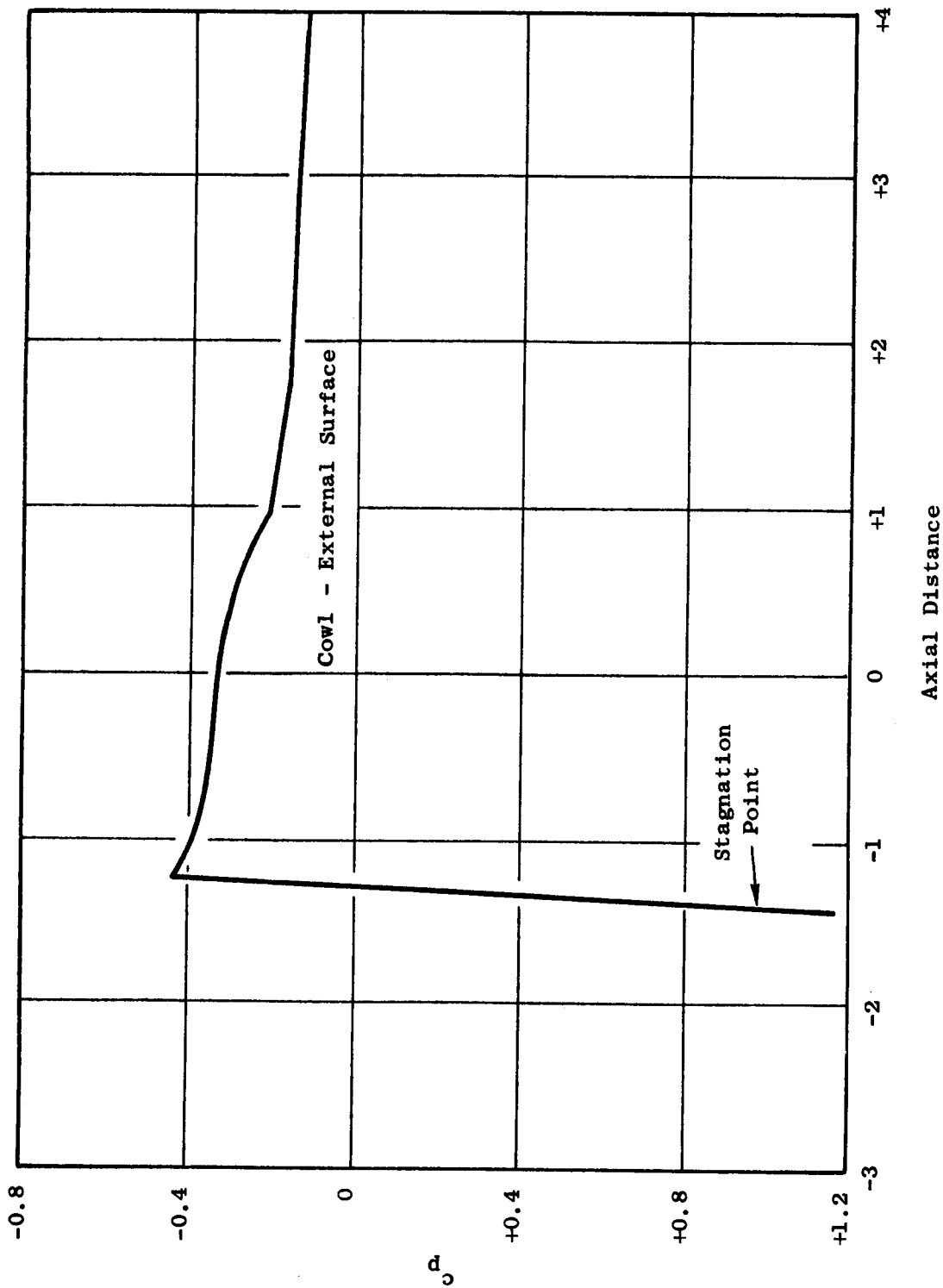
Figure 8. Two-Dimensional Inlet Pressure Distribution, External Channel.

19
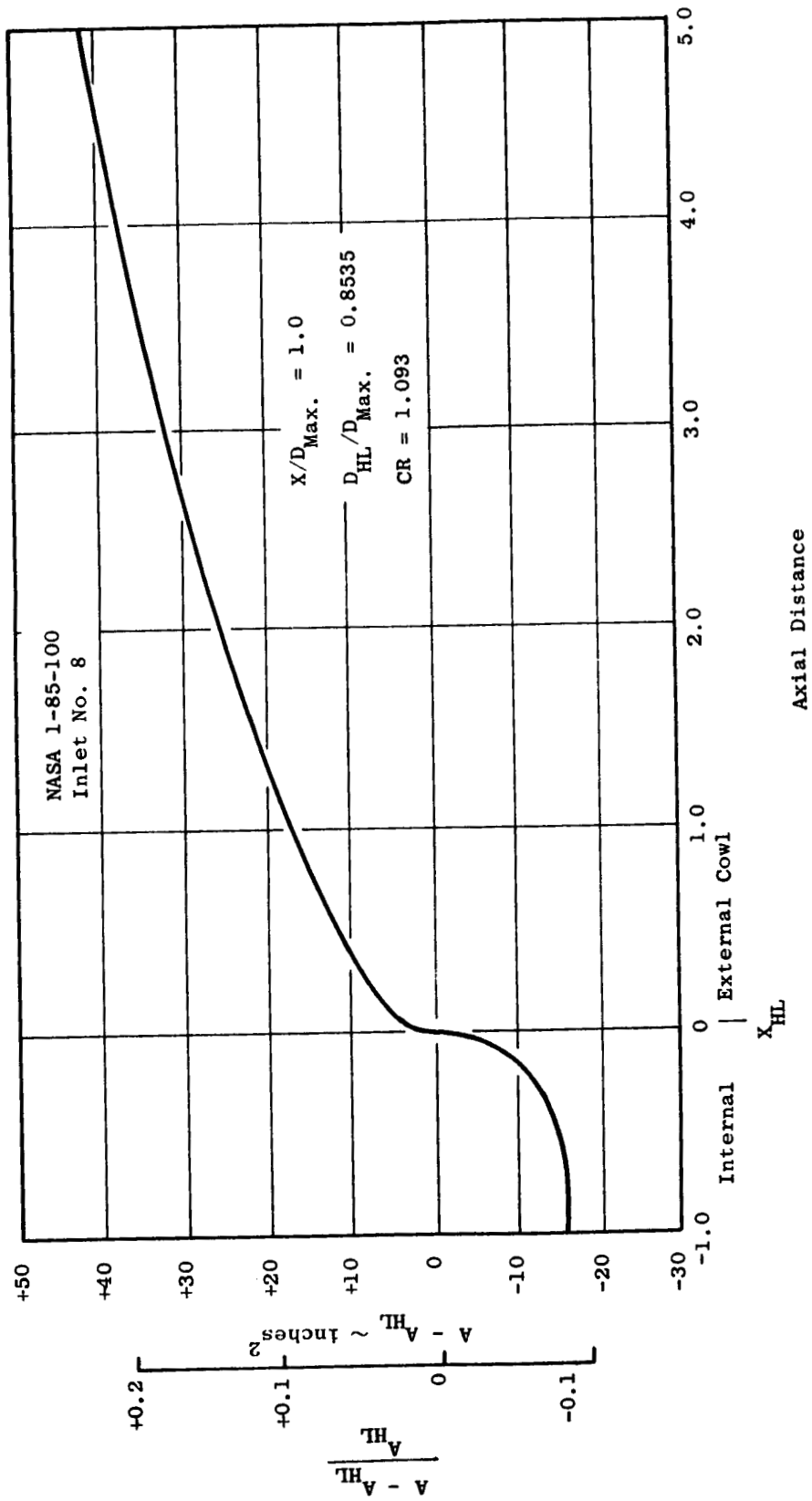
Figure 11. NASA 1-85-100 No. 8 Inlet Projected Area Distribution.

NASA 1-85-100
Inlet No. 8

$X/D_{Max.} = 1.0$

$D_{HL}/D_{Max.} = 0.8535$

$CR = 1.093$

Internal | External Cowl

X_{HL}

Axial Distance

$A - A_{HL} \sim$ inches^2

$\dfrac{A - A_{HL}}{A_{HL}}$

22

The inlet No. 8 was analyzed with the streamtube curvature analysis for three Mach numbers and two mass flow ratios. The selected Mach numbers were nominally 0.8, 0.85, and 0.90, and the mass flow ratios were nominally 0.8 and 0.88. The actual values were set to match the measured test results for Mach number and mass flow ratio. No mass flows below 0.80 were considered because inspection of test data indicated that flow separation was present on the external surface lip.

The STC analysis is an inviscid flow prediction. Viscous effects such as boundary layer displacement thickness and separation have to be accounted for in a separate analysis. A turbulent boundary layer technique (SAB) has been incorporated in the transonic analysis (see Addendum). Some of the predicted results shown here will include viscous effects. These results will be discussed more fully in the Addendum.

A typical predicted flow field, after 12 grid refinements, is shown in Figure 12 for the inlet at $M_O = 0.92$ and a mass flow ratio of 0.88. This is not one of the Mach numbers included above, but is used for demonstrating the calculation results. The extra grid refinement in the lip stagnation region is evident.

The comparison of the predicted pressure on the cowl surface with the measured pressures is shown in Figure 13. The measured pressures consist of three lines of static taps at three circumferential positions (0°, 90°, and 180° forward looking aft). Note that the flow is symmetric over the nacelle cowl. The comparison plot is arranged so that the highlight diameter occurs at an axial distance of zero, and the internal surface of the cowl lip is shown as a negative distance. Thus, the surface pressure distribution can be represented as a continuous curve.

The predicted results from STC show that the stagnation point is located exactly, and that the pressure distribution is predicted quite accurately. The sonic pressure coefficient, C_p*, is indicated, and the comparison shows that a shock is present on the inner surface. The mass flow ratio is relatively high so that there is little acceleration over the external surface.

The comparisons of predicted pressure distributions from the STC analysis with the NASA-Langley test results from the 16-foot wind tunnel are shown in Figures 14 through 20. These cover the range of Mach numbers and mass flows listed above.

At $M_o = 0.8$, the comparisons are generally good for a solution representing 700 grid points (solid lines in Figures 14 and 15.) When 1100 grid points were used for a mass flow ratio of 0.81, the local oscillations in the inviscid flow were evident. The test data indicate that viscous effects on the wall eliminate this pressure fluctuation. Later analysis with the viscous analysis predicted local separation (see Addendum).

At $M_o = 0.85$ and a mass flow ratio of 0.8819, the correlations between measured and predicted still show good agreement (Figure 16). For a mass flow ratio of 0.8064 at $M_o = 0.85$, the effects of compression waves and
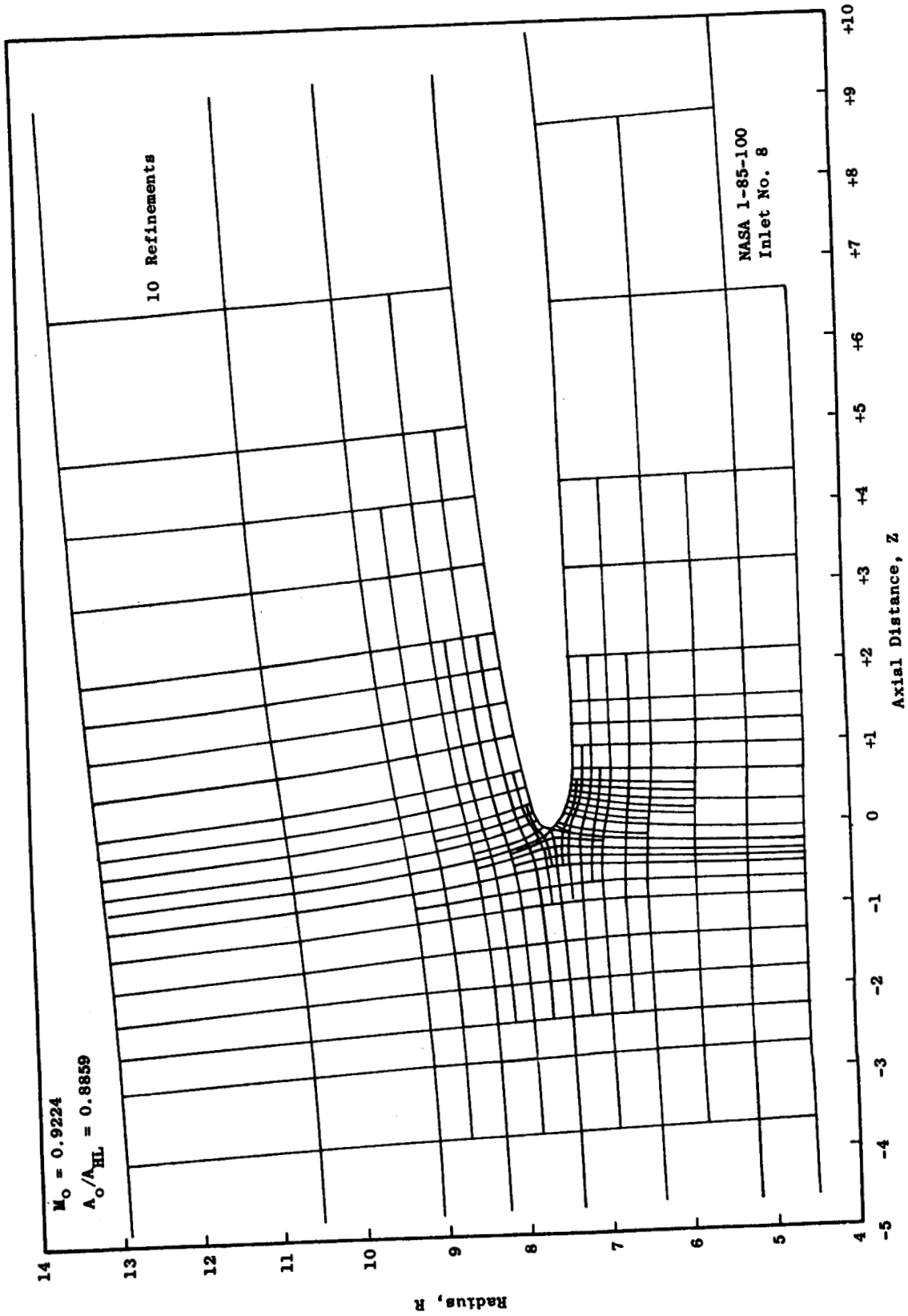
Figure 12. NASA 1-85-100 No. 8 Inlet Predicted Flow Field.

$M_0 = 0.9224$

$A_0/A_{HL} = 0.8859$

10 Refinements

NASA 1-85-100
Inlet No. 8

Axial Distance, Z

Radius, R

24
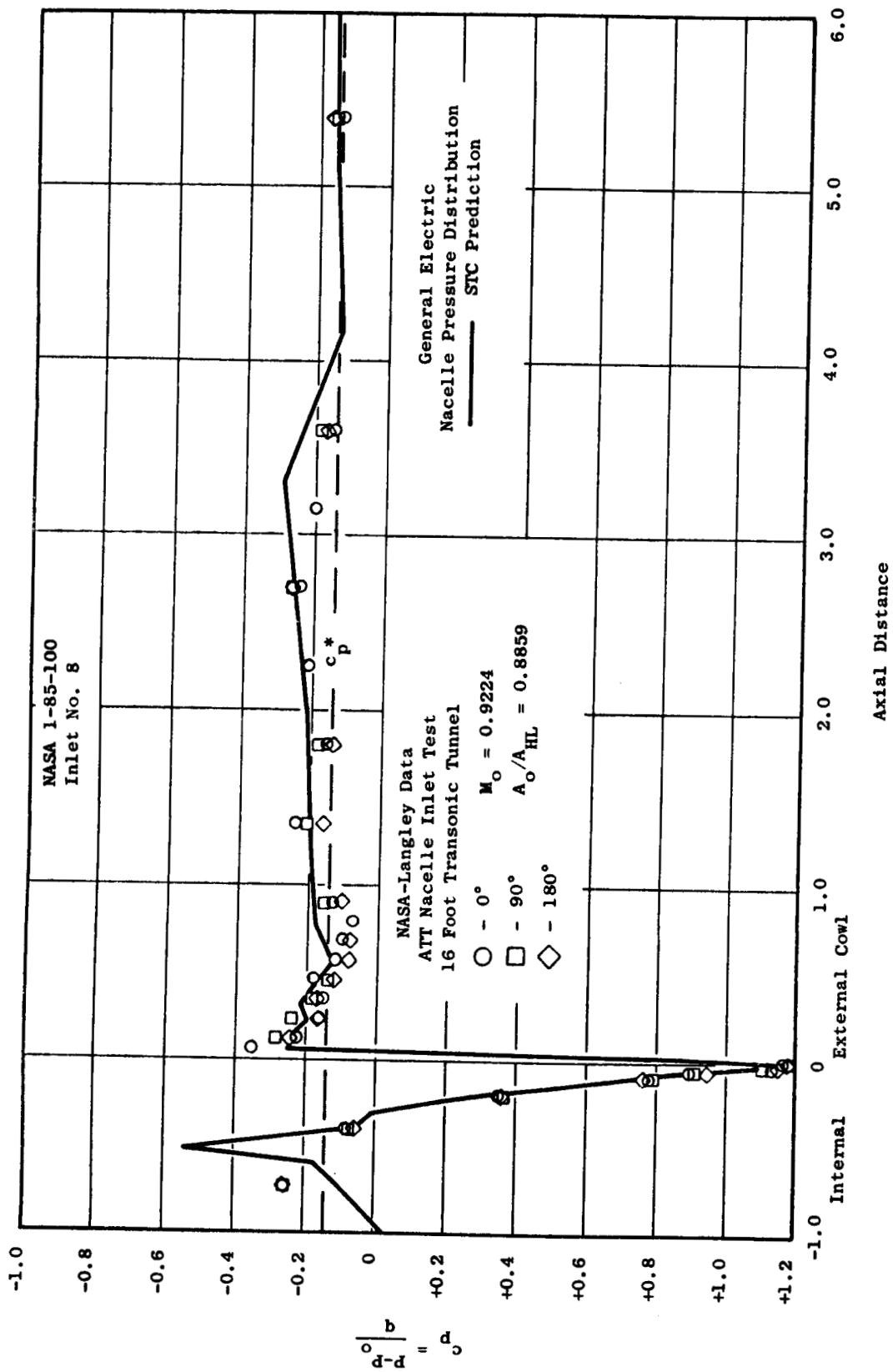
Figure 13. NASA 1-85-100 No. 8 Inlet Nacelle Pressure Distribution @ $M_O = 0.9224$.
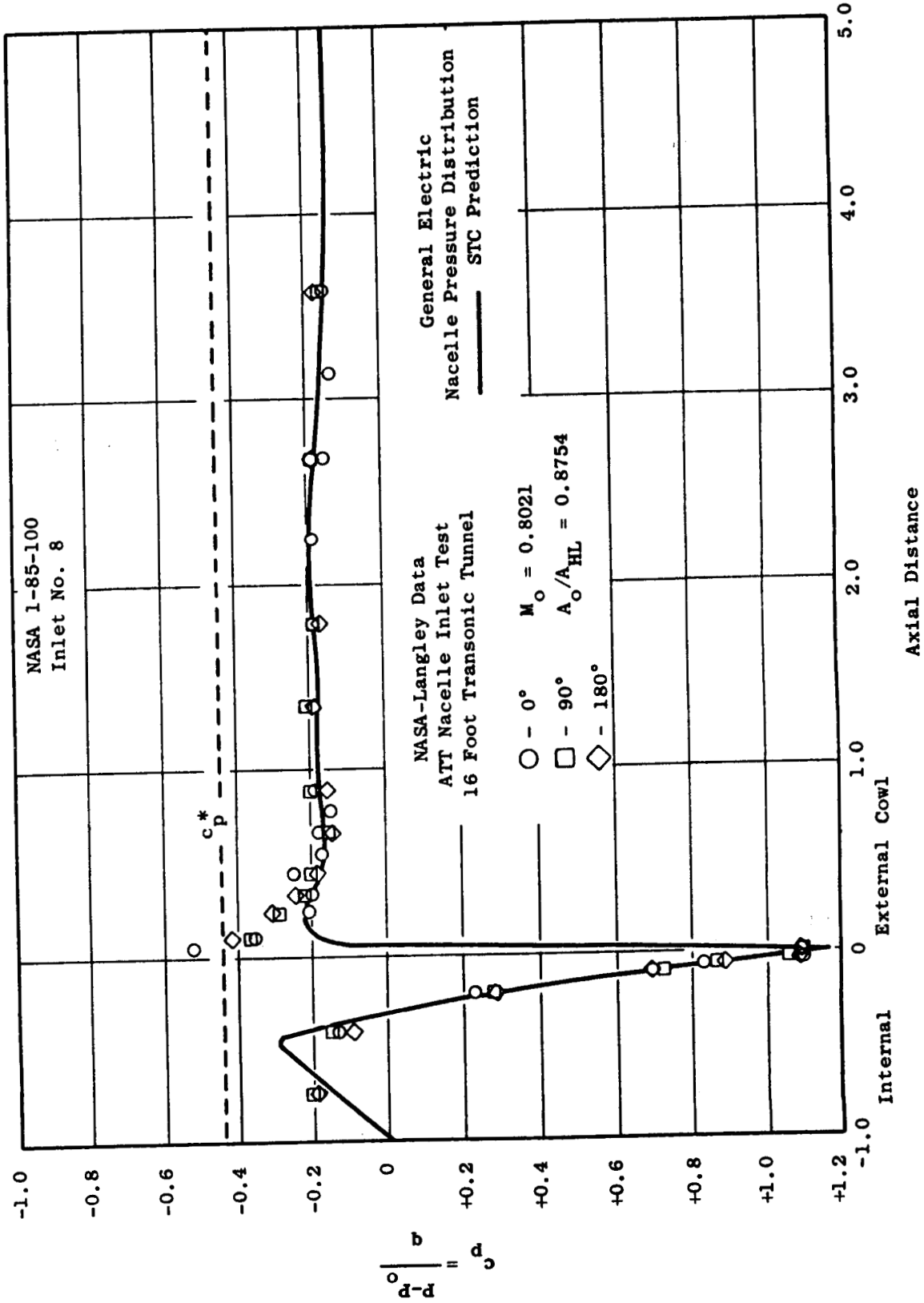
Figure 14.   NASA 1-85-100 No. 8 Inlet Nacelle Pressure Distribution.

NASA 1-85-100
Inlet No. 8

General Electric
Nacelle Pressure Distribution
STC Prediction

NASA-Langley Data
ATT Nacelle Inlet Test
16 Foot Transonic Tunnel

$M_O = 0.8021$

$A_O/A_{HL} = 0.8754$

○ – 0°
□ – 90°
◇ – 180°

c_p^*

$c_p = \dfrac{p - p_o}{q_o}$

Internal   External Cowl

Axial Distance

NASA 1-85-100 No. 8 Inlet Nacelle Pressure Distribution @ $M_O = 0.8021$.
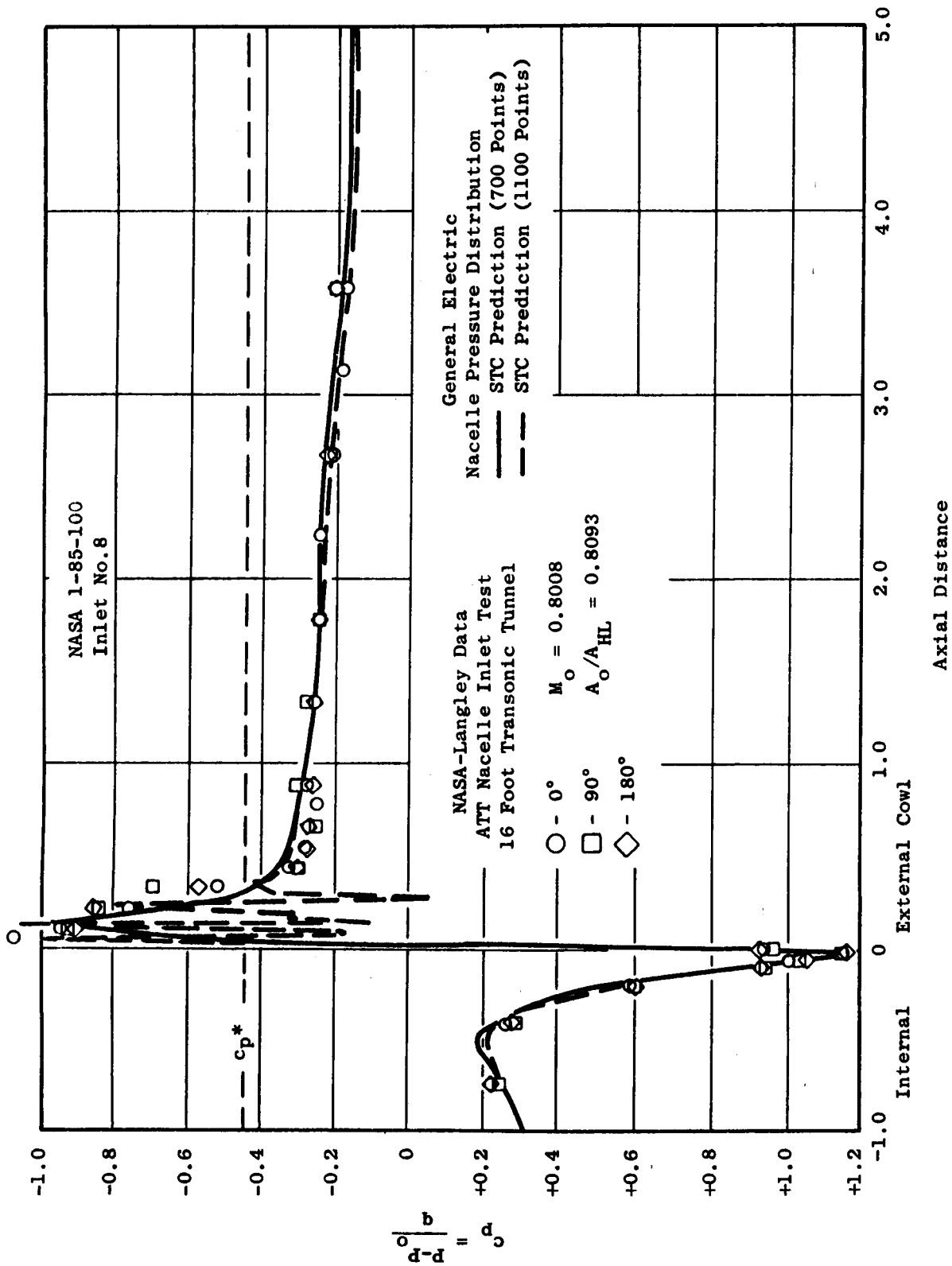
Figure 15. NASA 1-85-100 No. 8 Inlet Nacelle Pressure Distribution @ $M_o = 0.8008$.
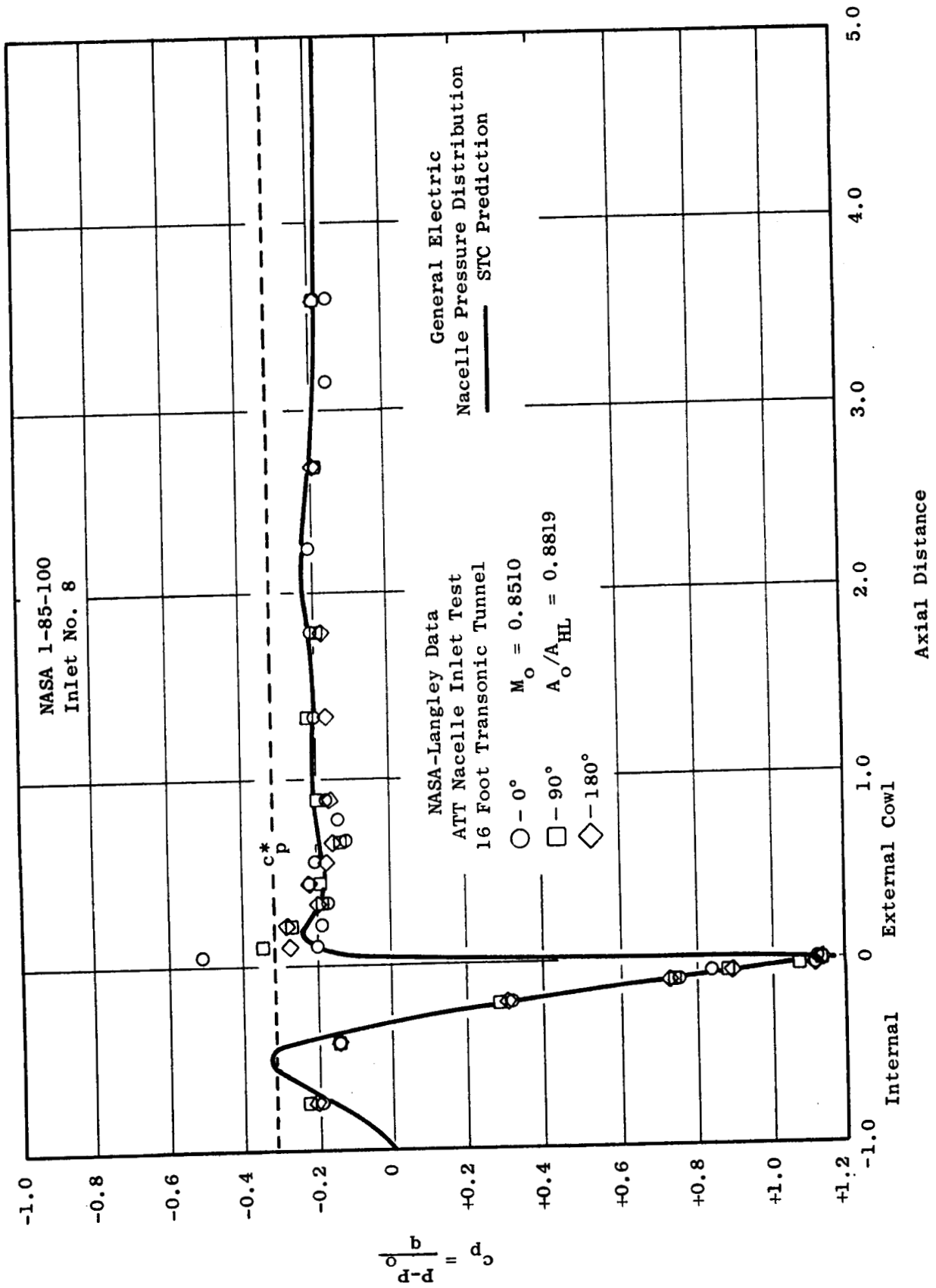
Figure 16. NASA 1-85-100 No. 8 Inlet Nacelle Pressure Distribution @ M_o = 0.8510.

viscous interactions are evident (Figure 17). The inviscid pressure distribution predicted by the STC analysis indicates compression waves, both with 700 grid points and with 900 grid points including viscous effects. Also, local separation is predicted after the first compression wave. From the experimental pressure measurements, it is not evident that the flow separation exists over a large region. Once the flow reattaches, there is excellent agreement between the measured and predicted pressures. In the local region on the cowl lip, there is evidence of viscous shock interactions, and the inviscid flow calculated by the STC analysis will not correlate with the test data.

The comparisons at $M_O = 0.90$ indicate that viscous effects are more important. The predicted flow field at a mass flow ratio of 0.885 agrees much better when boundary layer displacement thickness is included (Figure 18). At a mass flow ratio of 0.81 (Figure 19), the predicted pressure distribution shows several strong compression waves, and separation is indicated. From the experimental pressure measurements, there is evidence that the flow separation exists over the initial portion of the cowl lip. The measurements appear to show a gradual recompression followed by a weaker wave at an axial distance of 1.5. The viscous effects are very evident, and the inviscid analysis needs to be augmented with a detailed boundary layer analysis.

For a fully subsonic flow, the inviscid analysis by STC predicts the wall surface pressures excellently. Figure 20 shows a comparison of $M_O = 0.70$ and a mass flow ratio of 0.87.

The integrated pressure forces, both measured and predicted, are summarized in Table I. The integrated pressure drag on the external surface, normalized by free-stream dynamic pressure and maximum nacelle area, is noted as C_{D_P}. For STC, the integration starts at the calculated stagnation point and extends over the external surface to the maximum diameter. The integrated pressure drag from the NASA-Langley test data is the sum of the pressure integrals from the three rows of static taps ($0°$, $90°$, and $180°$) applied to the complete nacelle (where the $90°$ row is assumed for the $270°$ row). The equation is as follows:

$$C_{D_P} = \frac{\int \left(P - P_o\right) d\, A_{Proj}}{q\, A_{Max.}} \tag{10}$$

The total pressure drag on the inlet is predicted by summing the pressure integral on the stagnation streamline (additive drag) and the pressure integral on the external surface. This total force is again normalized by the free-stream dynamic pressure and the maximum area. There are no comparable measured drag data, since the force balance includes the friction force on the external surface. Also shown in Table I are the number of grid points used in the solution and whether the viscous effects (SAB) were included.
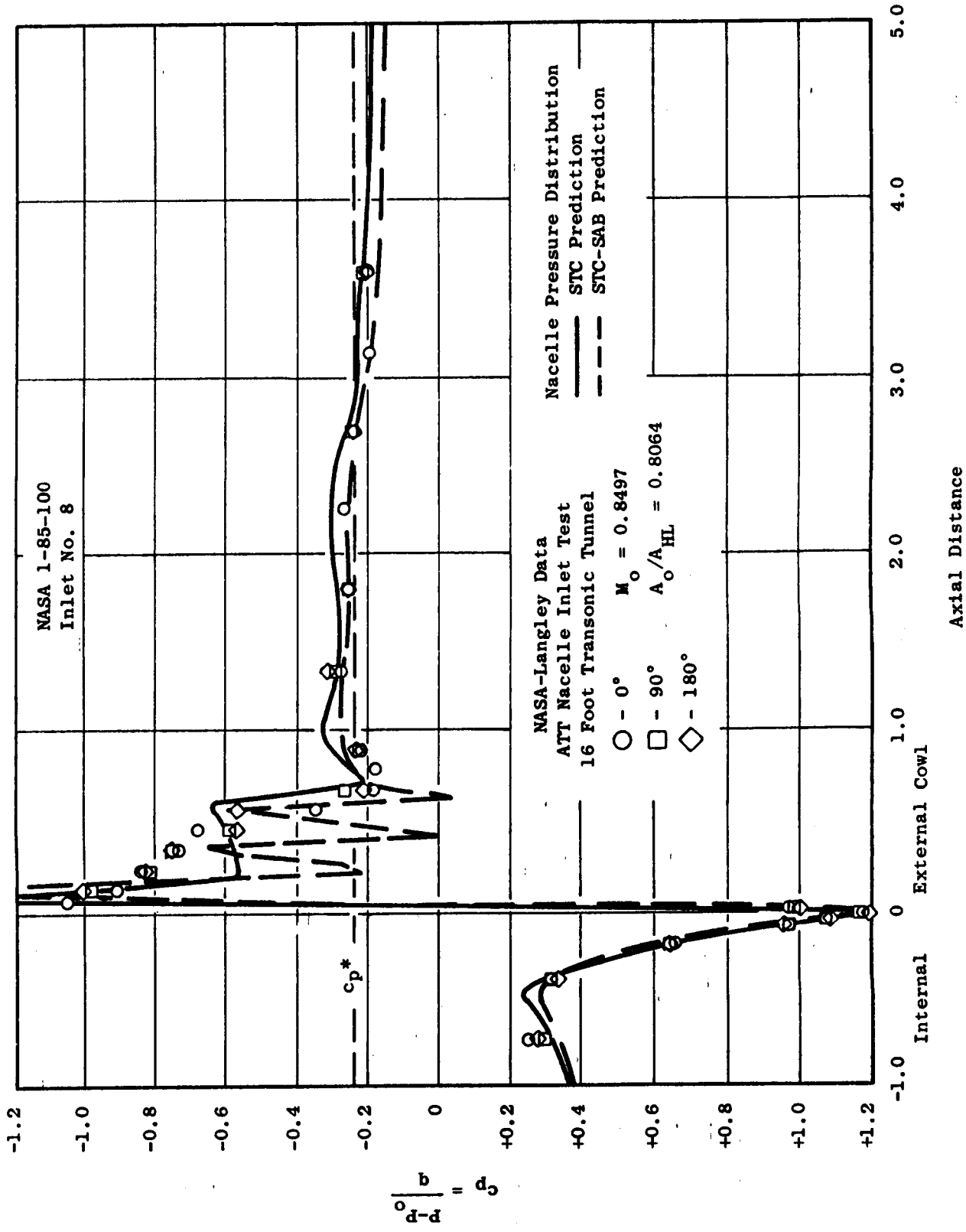
Figure 17. NASA 1-85-100 No. 8 Inlet Nacelle Pressure Distribution @ $M_O = 0.8497$.

30
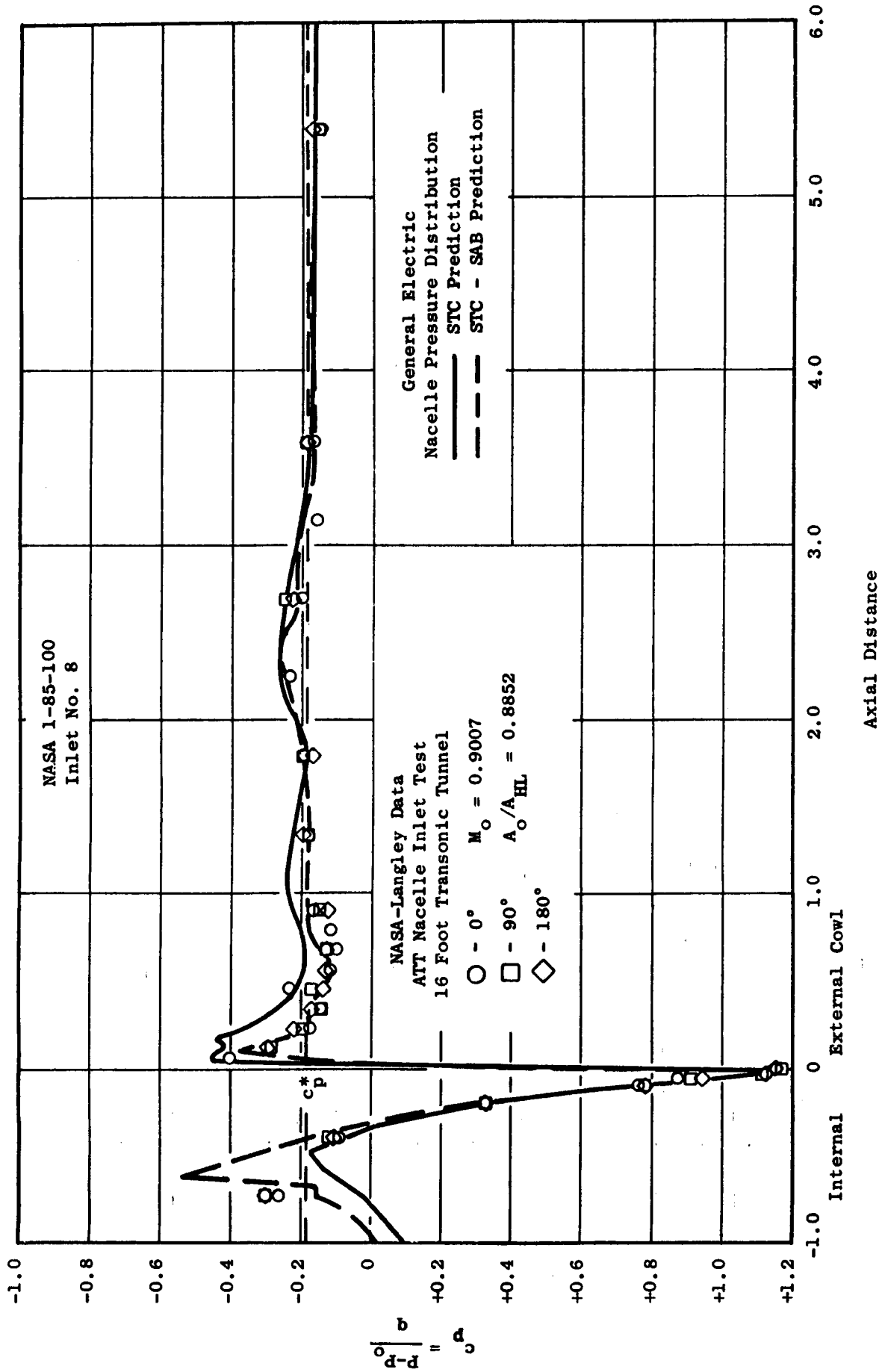
Figure 18. NASA 1-85-100 No. 8 Inlet Nacelle Pressure Distribution @ $M_O = 0.9007$.

31
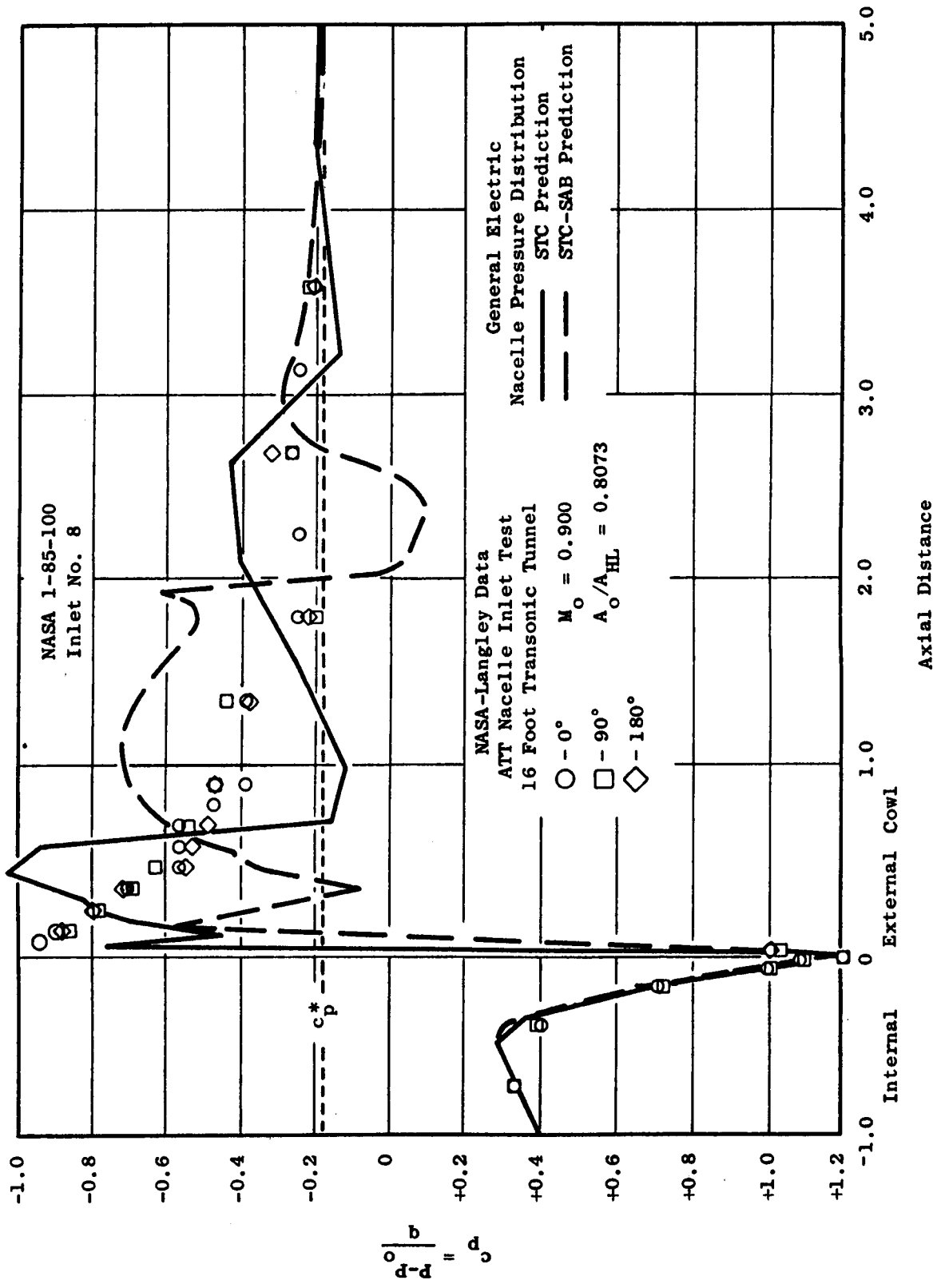
Figure 19. NASA 1-85-100 No. 8 Inlet Nacelle Pressure Distribution @ M_o = 0.900.

32
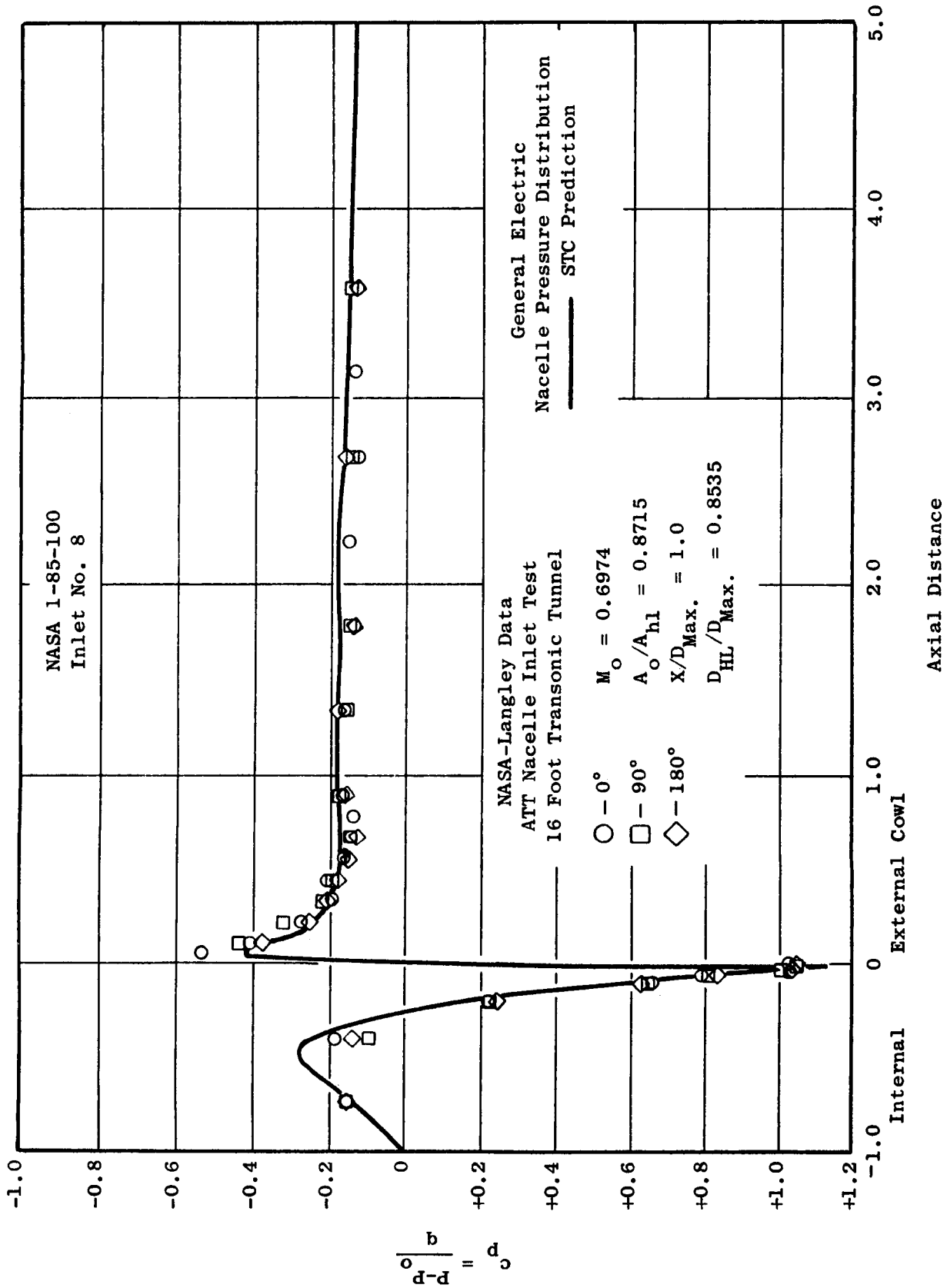
Figure 20. NASA 1-85-100 No. 8 Inlet Nacelle Pressure Distribution @ M_O = 0.6974.

NASA 1-85-100
Inlet No. 8

General Electric
Nacelle Pressure Distribution
——— STC Prediction

NASA-Langley Data
ATT Nacelle Inlet Test
16 Foot Transonic Tunnel

○ — 0°	M_O = 0.6974
□ — 90°	A_O/A_{hl} = 0.8715
◇ — 180°	$X/D_{Max.}$ = 1.0
	$D_{HL}/D_{Max.}$ = 0.8535

Internal   External Cowl   Axial Distance

$$C_p = \frac{P-P_o}{q_o}$$

-1.0
-0.8
-0.6
-0.4
-0.2
0
+0.2
+0.4
+0.6
+0.8
+1.0
+1.2

-1.0   0   1.0   2.0   3.0   4.0   5.0

Table I. Integrated Pressure Forces.

M_o	A_o/A_{HL}	C_{D_P} Measured	C_{D_P} Predicted	Total C_{D_P}	Grid Points	SAB
0.6974	0.8715	-0.023	-0.034	-0.008	715	No
0.8021	0.8754	-0.025	-0.023	0.006	626	No
0.8008	0.8093	-0.039	-0.044	0.009	656	No
		-0.039	-0.040	0.010	1091	No
0.8008	0.8093	-0.039	-0.047	0.004	997	Yes
0.8510	0.8819	-0.025	-0.030	-0.001	758	No
0.8497	0.8064	-0.044	-0.053	0.003	906	Yes
		-0.044	-0.059	-0.028	717	No
0.9007	0.8852	-0.0257	-0.022	0.009	700	Yes
		-0.0257	-0.031	-0.001	928	Yes
0.9001	0.8073	-0.050	-0.054	0.009	782	Yes

Overall, the inviscid analysis by STC is in general agreement with the test measurements, except where viscous interactions are significant. The need to include viscous effects is obvious. Further work is necessary to properly define the separation bubble and the point of reattachment.

4.4 AFTERBODY WITH SHOCK

A nacelle afterbody with a 24° boattail angle was analyzed with the Streamtube Curvature Analysis. The geometry, shown in Figure 21, represents the high subsonic cruise configuration of a nacelle afterbody designed for supersonic operation. The afterbody model was tested with a sting-mounted forebody at a Mach number of 0.90. A comparison of the experimental results and the predicted pressure distribution is shown in Figure 22.

The predicted pressures indicate a pressure drop or local acceleration around the radius onto the 24° boattail, then a sharp compression or shock. The location of this compression is a result of the numerical star-switching procedures built into the STC analysis, when the velocity changes from supersonic to subsonic. The strength of the shock is related to the local change in curvature across the orthogonal line defining the star switch. The exact Rankine-Hugoniot equations are not included in order to not over-constrain the problem. The entropy rise across the shock or compression wave on any streamline can be defined, based on the static pressure rise defined by the flow field. In this particular case, the upstream Mach number was 1.31 and the downstream Mach number was 0.78. This corresponds to a normal shock at the body surface. Thus, without including the exact shock relations, the predicted compression represents the location and strength of a normal shock.

The experimental results show that the predicted compression wave or shock is correctly positioned, but that the boundary layer separated at the shock. Once the flow separates, the static pressure is nearly ambient over the remainder of the boattail and no effect of the remaining boattail geometry or jet plume compression is evident. Thus, the STC analysis can locate the shock position and specify its approximate strength.

Dimensionless Distance from Nozzle Exit, $x/D_{Max.}$
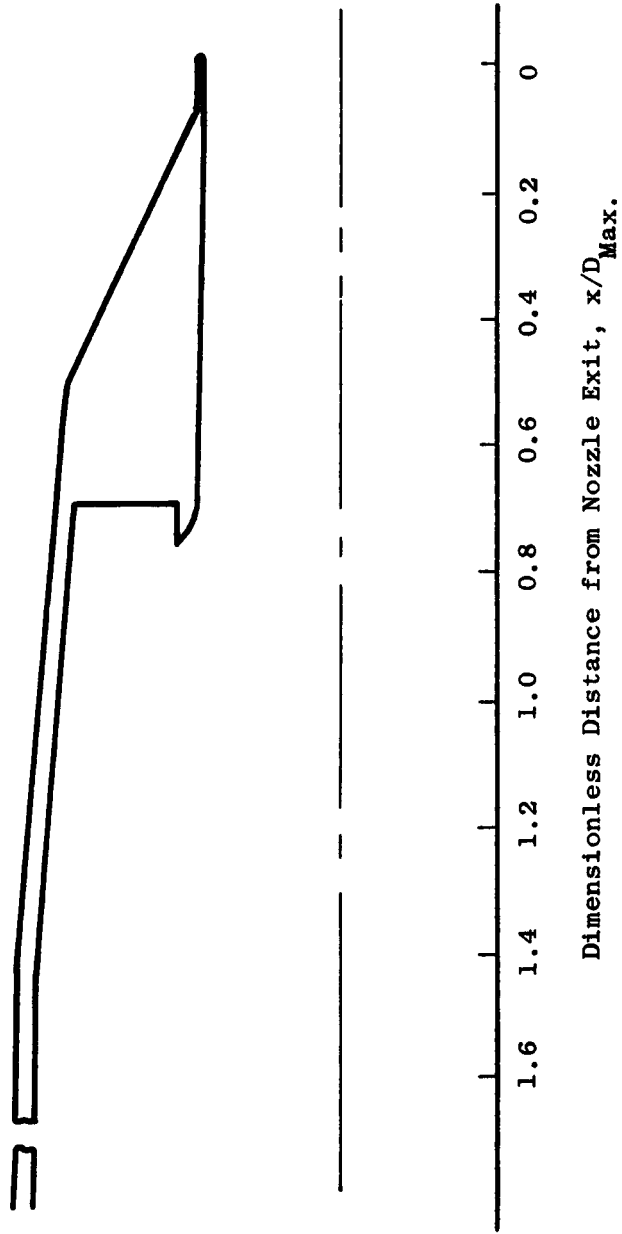
Figure 21. Nacelle Afterbody Cruise Nozzle Configuration.
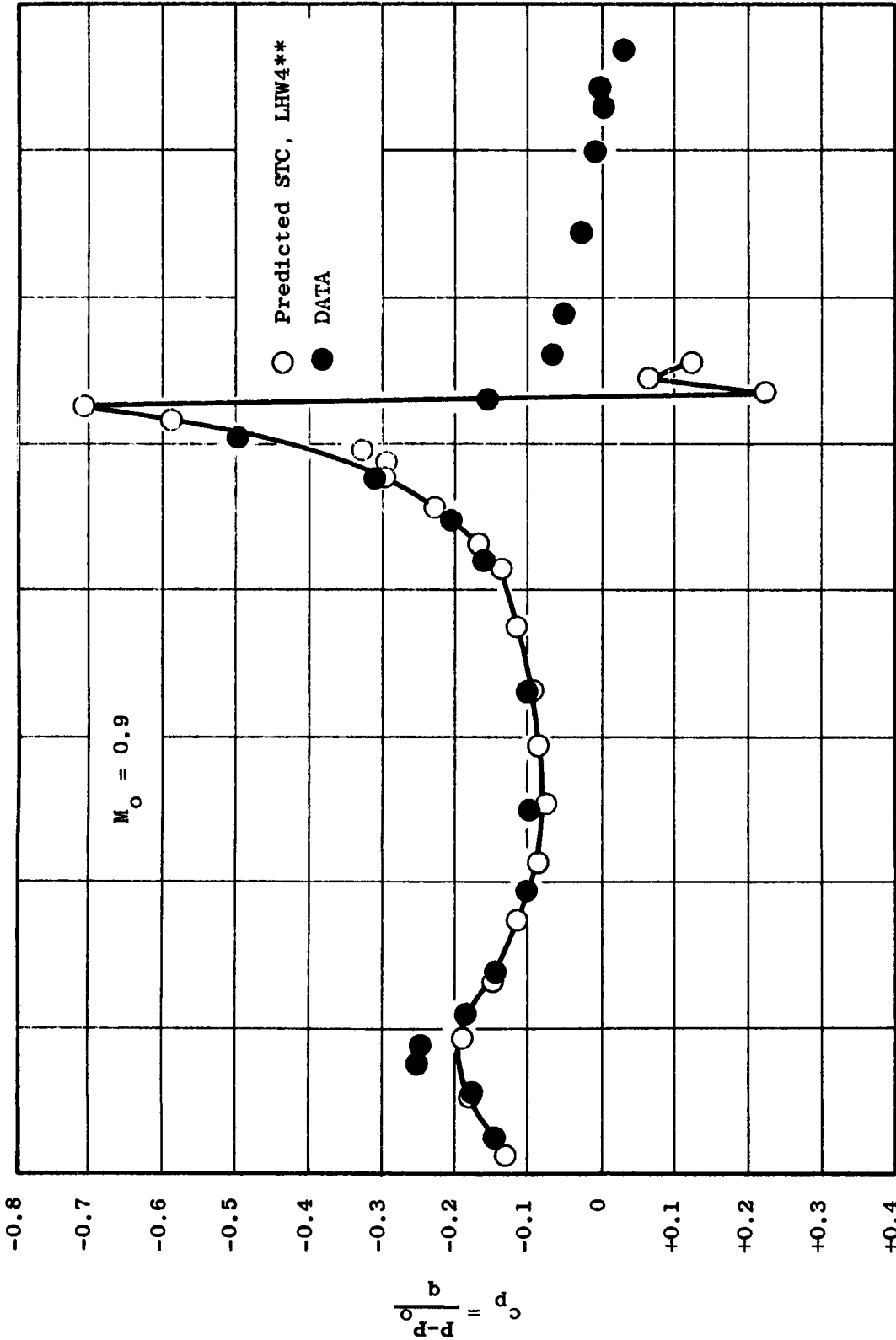
Axial Distance

Figure 22. Afterbody Pressure Distribution.

37

5.0 DETAILS OF THE NUMERICAL PROCEDURE

In this section the details of the numerical procedures employed in the Streamtube Curvature program are presented.

5.1 GRID COORDINATE SYSTEM

When the original grid is established (as shown in Figure 4) ξ_1 and ξ_2 coordinates are assigned to each orthogonal line and streamline. These values remain attached to the same line throughout the calculation procedure. ξ_1 generally has a value of zero at the upstream boundary and increases by 8.0 or 16.0 across each region. Similarly, the ξ_2 coordinate is zero on the lower boundary and is incremented by 8.0 across each channel. Double streamlines are used to separate the channels and each has the same value of ξ_2.

As the grid is subdivided during the refinement process, the new lines are given coordinate values half way between those on either side. As a result, each grid point has a ξ_1, ξ_2 coordinate. However, these coordinates are for notational and bookkeeping purposes only. ξ_1 and ξ_2 values do not enter into the solution of the equations. They are employed in the STC Program because, with the conventional counting system (such as the streamline number or the orthogonal line index) the value associated with a given line would be changed when new lines are inserted into the field, whereas the ξ_1, ξ_2 values are not.

The ξ_1 values always increase in the downstream direction, and the ξ_2 values always increase when one proceeds across the field (to the left after facing downstream). Because of the possibility of multiple channels, the streamline and orthogonal line index values are not so ordered.

Reference will be made to the ξ_1 coordinate in Section 5.3, where the ξ_1 value is used to establish the relative spacing between orthogonal lines.

5.2 CURVATURE OF THE STREAMLINES

5.2.1 The Beam Fit

The third step in the calculation procedure as outlined in Section 3 is the determination of the streamline curvatures, angles, and cumulative curvilinear lengths at each grid point. An accurate and rapid method for accomplishing this is to fit a draftsman's spline or, equivalently, to use the formulas which apply to a beam loaded at discrete points. The classical relation which is applicable here is that the moment, M, varies linearly, or:

$$\frac{d^2y}{dx^2} = \frac{M}{EI} = bx \tag{11}$$

In Equation 11, y is the vertical displacement, E is the modulus of elasticity, I is the cross-sectional moment of inertia, and b is a constant. A limitation on Equation 11 is that:

$$\left(\frac{dy}{dx}\right)^2 \ll 1$$

To ensure that this condition is satisfied, the coordinate system in which the equation for the beam centerline is written is rotated as shown in Figure 23. As indicated, the curve-fit equations utilize a different coordinate frame for each interval. For the interval between point i and i+1, the origin is placed at point i and the x-axis passes through point i+1.

The displacement equation for a beam with point loading is a cubic polynominal and may be expressed as:

$$y = b_i x + c_i x^2 + d_i x^3 \qquad \text{(for the } i^{th} \text{ internal)}$$

A more convenient form of the cubic which passes through both points i and i+1 is:

$$\frac{y}{\Delta x} = y_a' \left(-g^3 + g^2\right) + y_b' \left(f^3 - f^2\right) \qquad (12)$$

where:

$$y_a' = \text{Slope at } x = 0$$

$$y_b' = \text{Slope at } x = \Delta x$$

$$f = x/\Delta x$$

$$g = (\Delta x - x)/\Delta x = 1-f$$

The cubic fit to the adjacent intervals must be matched so that, at the junction points, the angle and curvature are the same. As is illustrated in Figure 23, this requires:

$$\tan^{-1}\left[y_{b(i-1)}'\right] = \tan^{-1}\left[y_{a(i)}'\right] + \Delta\alpha_i \qquad (13)$$

$$\frac{y_{b(i-1)}''}{\left[1 + y_{b(i-1)}'^2\right]^{\frac{3}{2}}} = \frac{y_{a(i)}''}{\left[1 + y_{a(i)}'^2\right]^{\frac{3}{2}}} \qquad (14)$$

Good approximations to Equations 13 and 14, providing $\Delta\alpha$ is $10°$ or less, are:

Point b (Interval i)

i^{th} Interval Cubic Polynominal
$$y = b_i x + c_i x^2 + d_i x^3$$

Matching Conditions

1. $\tan^{-1}[y'_{b(i-1)}] = \tan^{-1}[y'_{a(i)}] + \Delta\alpha_i$

2. $\dfrac{y''_{b(i-1)}}{\left[1 + y'^2_{b(i-1)}\right]^{3/2}} = \dfrac{y''_{a(i)}}{\left[1 + y'^2_{a(i)}\right]^{3/2}}$

x

y

$\Delta\alpha_i$

Δr_i

Point a (Interval i)
Point b (Interval i-1)
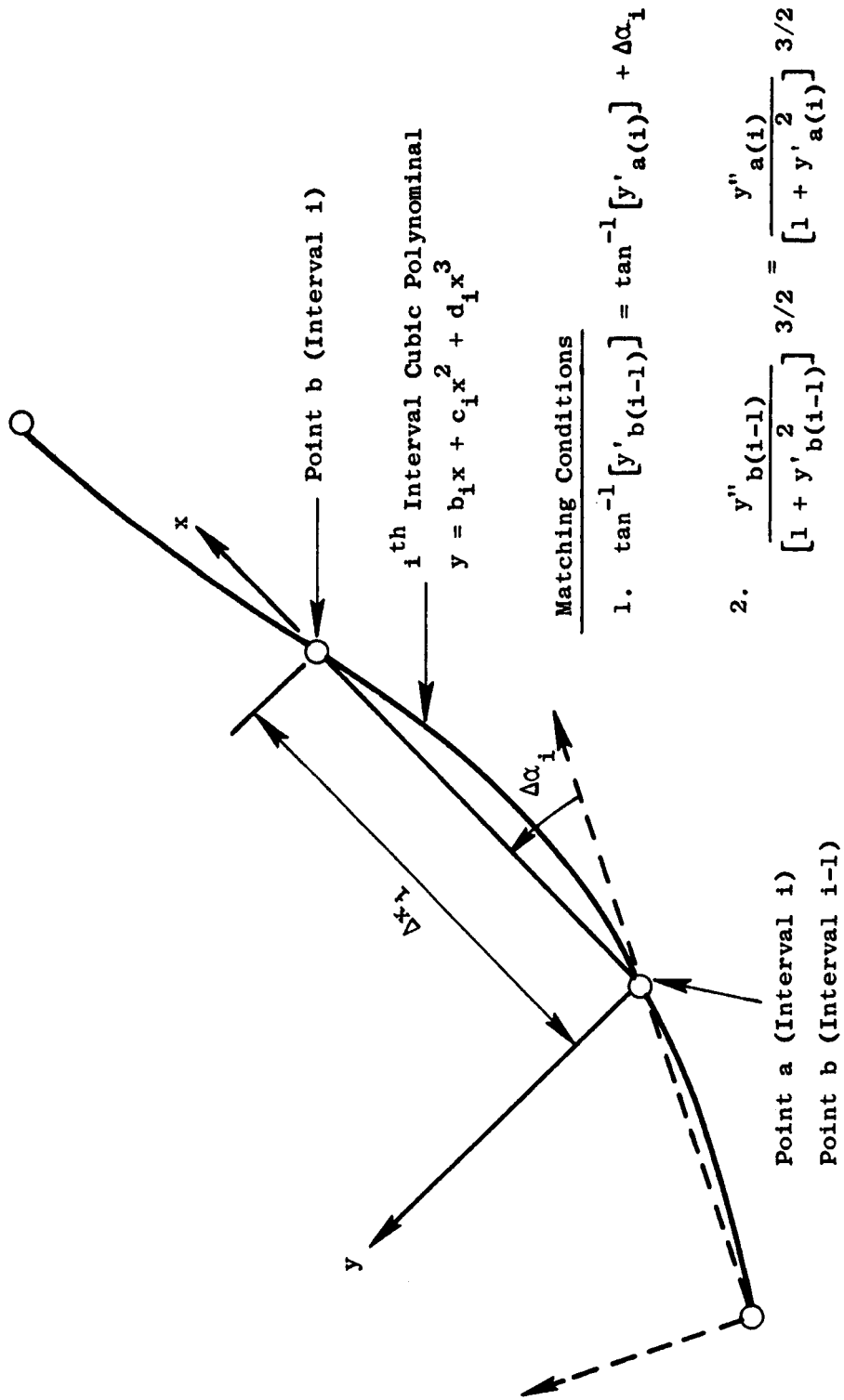
Figure 23. Curve-Fit Algorithm.

40

$$y'_{b(i)} = y'_{a(i+1)} + \Delta\alpha_{(i+1)} \tag{15}$$

and:

$$\frac{y''_{b(i-1)}}{1 + \frac{3}{2} y'^2_{b(i-1)}} = \frac{y''_{a(i)}}{1 + \frac{3}{2} y'^2_{a(i)}} \tag{16}$$

Substitution of Equation 15 into Equation 12, and the result differentiated gives:

$$\frac{d^2y}{dx^2} = \frac{1}{\Delta x_i} \left\{ y'_{a(i)} (6f-4) + \left[y'_{a(i+1)} + \Delta\alpha_{(i+1)} \right] (6f-2) \right\} \tag{17}$$

At point i, but for the i-1 interval, it follows from Equation 17 that:

$$y''_{b(i-1)} = \frac{1}{\Delta x_{(i-1)}} \left\{ 2y'_{a(i-1)} + 4 \left[y'_{a(i)} + \Delta\alpha_i \right] \right\} \tag{18}$$

For the same point, but for the ith interval, we have:

$$y''_{a(i)} = \frac{1}{\Delta x_i} \left\{ -4y'_{a(i)} - 2 \left[y'_{a(i+1)} + \Delta\alpha_{(i+1)} \right] \right\} \tag{19}$$

Equations 18 and 19, substituted into Equation 16 and rearranged, give the following recurrence equation for $y'_{a(i)} = b'_1$:

$$A_{1i} b_i + 2\left(A_{1i} + A_{3i}\right) b_i + A_{3i} b_{(i+1)} = -2A_{1i} \Delta\alpha_i - A_{3i} \Delta\alpha_{(i+1)} \tag{20}$$

$$(i = 2,3,4.....N-1)$$

where:

$$A_{1i} = \Delta x_i \left[1 + \frac{3}{2} y'^2_{a(i)} \right] \tag{21a}$$

$$A_{3i} = \Delta x_{(i-1)} \left[1 + \frac{3}{2} y'^2_{b(i-1)} \right] \tag{21b}$$

Note that b_i is used in place of $y'_{a(i)}$ to simplify the notation. Notice that because of the y'_a and y'_b dependency, the values of A cannot be evaluated directly; instead, they are determined by iteration. However, because y'_a is always very small, two passes (one correction pass) are generally sufficient for their determination.

Given A_{1i} and A_{3i}, together with the boundary condition equations presented below, the set of equations given by Equation 20 yields a tridiagonal matrix equation which is solved by standard procedures. y_b' is then evaluated using Equation 15. Likewise, the ordinate at any intermediate point can be computed by Equation 12; and Equation 16, together with Equation 19, gives the curvature at each point.

The curvilinear distance over the interval is given by the expression:

$$\int_i^{i+1} ds = \Delta x_i \int_0^1 \left(1 + y'\right)^{\frac{1}{2}} df \tag{22}$$

The first two terms of the binominal expansion are:

$$\left(1 + y'\right)^{\frac{1}{2}} = 1 + \tfrac{1}{2}y' + \dots \tag{23}$$

Using Equations 12 and 23 in Equation 22 yields:

$$S_{(i+1)} - S_i = \Delta x_i \left[1 + \left(y_a'^2 + \tfrac{1}{2}y_a'y_b' + y_b'^2\right)\Big/15\right] \tag{24}$$

This equation is employed to calculate the cumulative curvilinear distance along the streamlines.

5.2.2 Beam End Condition Options

Three different end options are available with the beam curve fit:

● The angle may be specified.

● The curvature may be specified.

● The ratio of y''' (the rate of change of curvature) at the end point to the value at the next-to-end point may be specified.

As a ground rule, the second option is used for fitting the streamlines. For those streamlines which extend to the flow inlet or flow exit boundary, the end curvature is taken as zero. (A constant value of curvature, different from zero, can also be enforced by user input.) If a streamline terminates within the field, the end curvature is interpolated from the curvature of the streamlines above and below.

The equations for the three end options, derived from the formulas listed in Section 5.2.1, for the first end are given below:

a) Specified Angle:

$$b_1 = \tan\left(\phi_1 - \alpha_1\right) \tag{25}$$

42

b) Specified Curvature:

$$4b_1 + 2b_2 = -2\Delta\alpha_2 + \Delta X_1 \, C_1 \left[1 + \frac{3}{2} y^2_{a(1)}\right] \tag{26}$$

c) F specified where $y_1''' = F \, y_2'''$

$$(\Delta X_2)^2 b_1 + \left[(\Delta X_2)^2 - F(\Delta X_1)^2\right] b_2 - F(\Delta X_1)^2 b_3 \tag{27}$$

$$= F \, \Delta\alpha_3 (\Delta X_1)^2 - \Delta\alpha_2 (\Delta X_2)^2$$

where:

ϕ_1 = Specified angle

c_1 = Specified curvature $(= - d^2y/dx^2)$

α_1 = Angle of the chord between points 1 and 2.

The parameter F can be given the following interpretation. When F = 0, the curvature in the end interval is constant. Hence, the end interval polynominal in this case reduces to a parabola. When F = 1, the third derivative in the first interval is equal to the third derivative in the second interval. In this case, since angle, curvature, and y''' are all continuous at the second point, the same cubic equation spans the first two intervals (at least to a good approximation for small $\Delta\alpha_2$).

Similar equations to Equations 25, 26, and 27 can be written for the downstream (or second) end of the beam fit. However, they are omitted here for brevity.

5.2.3 The Stagnation Point End Condition

The curvatures for points on a body surface are computed from the input geometry data, as will be discussed in another section. The curvature at a trailing edge point is taken to be the same as the body surface curvature; although, in reality, there may be a weak singularity at this point because of a finite wedge angle. Just downstream of the trailing edge, if the flow is subsonic, the curvatures are computed by the beam formulas where, at the trailing edge point, the third option (F = 0) is used for the upstream end condition.

The leading edge is handled in a slightly more complex way. It is a requirement in the STC Program that the leading edge be rounded and that a complete numerical description of the leading edge shape be supplied. At the stagnation point, then, the streamlines are required to turn a 90° corner. Two coincident stagnation streamlines are employed. One turns up and goes over the body; the other turns down and goes below. The location of the stagnation point is found iteratively. As shown on Figure 24, the
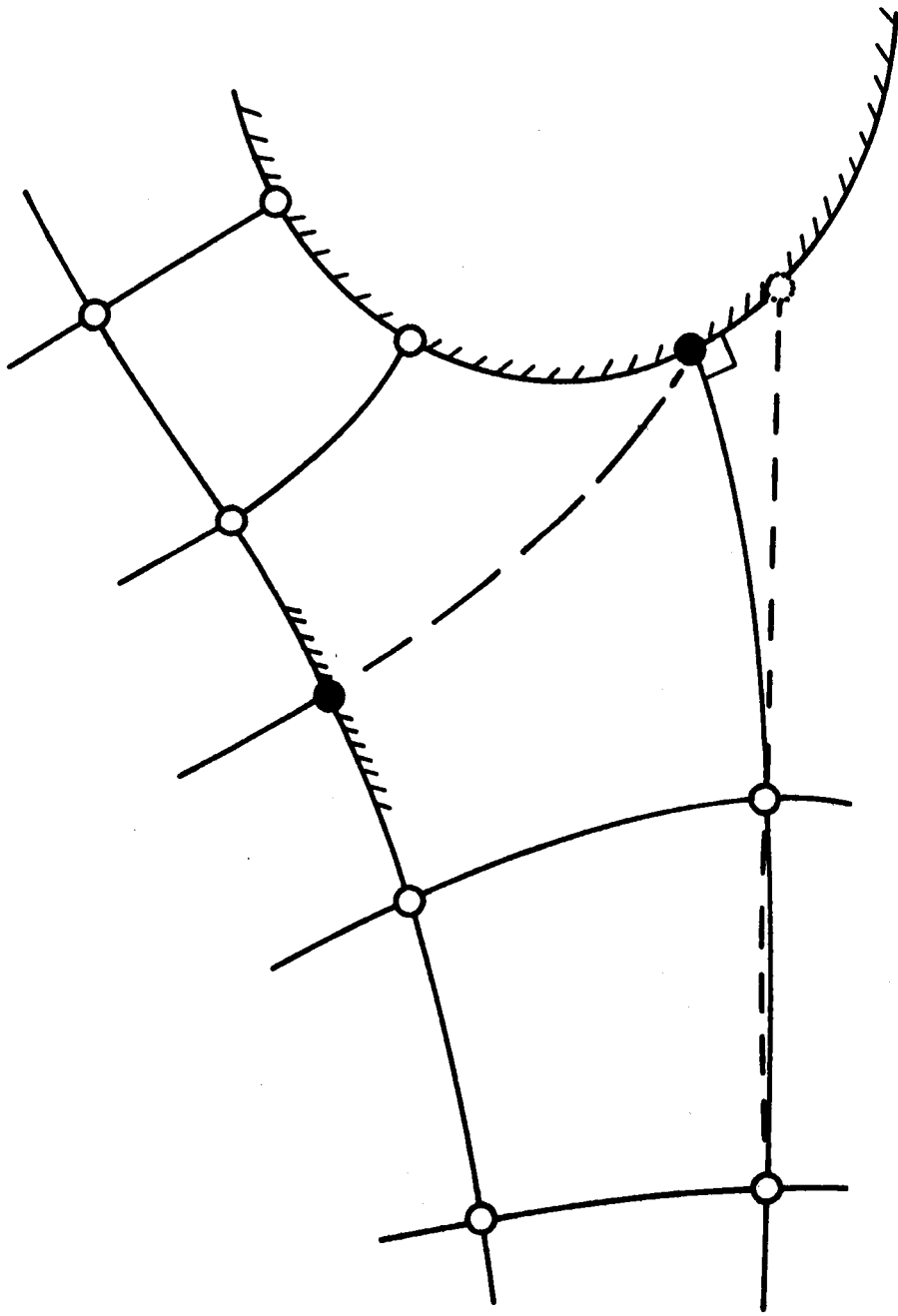
● Points Repositioned in the Streamline
Curvature Calculation Routine

Figure 24. Stagnation Point Iteration.

point is moved along the contour so that the intersection angle with the body surface is 90°. The streamline angle at the stagnation point is found by utilizing the spline fit with the third option (F = 1) for the downstream end condition.

5.2.4 Backward Curve Fits for Supersonic Regions

When the flow at a particular grid point is supersonic, the "complete" beam fit (or central difference) formula is not appropriate for the evaluation of curvature. To be consistent with the physical character of supersonic flow, the curvature at point i cannot be influenced by any points downstream of that point, such as the i+1 or i+2 points.

Therefore, to evaluate curvature at supersonic points, the "beam" is fitted to only 3 or 4 points to obtain a curvature at the last of these points. The beam-fit is moved along (by dropping a point at the upstream end and picking one up downstream) to calculate the curvature at sequential points on the streamline. Used in this way the beam formulas essentially represent either a parabolic (3-point) or a cubic (4-point) curve fit. The cubic fit is obtained when F at both ends, for the 4-point fit, is set to unity. Actually, more favorable agreement with theory (in the case of a two-dimensional Prandtl-Meyer turn) is obtained when F is set to about 0.75, and these are the standard values of F present in the STC program for the 4-point formula. F is automatically set to zero when the 3-point option is selected.

For pure supersonic flows, the 4-point curve fit (which is second order accurate) gives much better results than does the 3-point (first order accurate) formula. But for mixed flows, it is found that the 4-point formula generally leads to divergence and, therefore, the 3-point formula is always used for transonic cases.

5.2.5 The Evaluation of Curvature Very Close to a Sonic Line

In the STC method, the curvature must be known at the sonic (or near sonic) points just as at any other point in the field for use in the cross-stream momentum equation, Equation 7. This is in contrast to the velocity potential method of Murman and Cole where the second streamwise derivative of ϕ is insignificant because the coefficient $(1-M^2)$ is zero. Therefore, the following procedure is used to evaluate the streamline curvature at points close to a sonic line.

The point at which the sonic line crosses each orthogonal is identified by referring to the value of velocity (or, in reality, the coefficient B) from the previous iteration. Then, for some distance above and below the sonic line, the curvatures are taken to vary linearly between the values calculated according to Sections 5.2.1 to 5.2.4. This is illustrated in Figure 25. The extent of this linearly assumed variation is controlled by an input variable (TSIC).
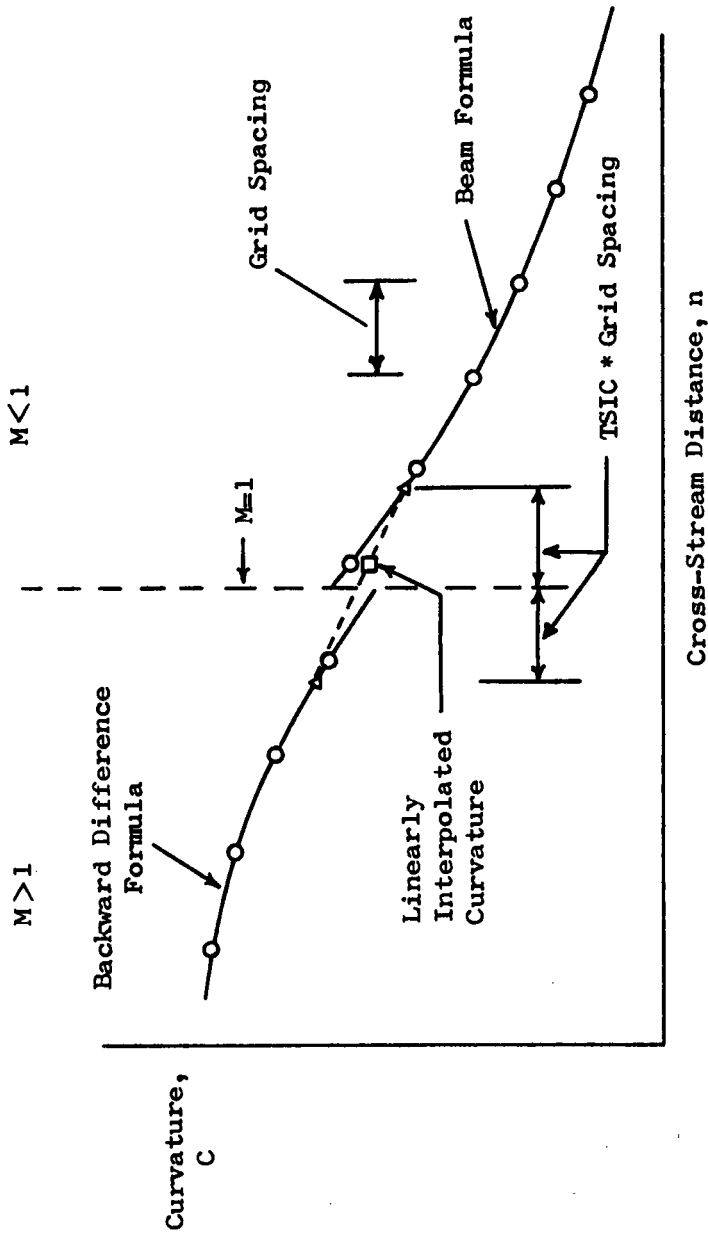
Figure 25. Evaluation of Curvature Near a Sonic Line.

5.2.6 Special Interior Points at Orthogonal Ends

As mentioned earlier, it is not required that a newly inserted orthog-
onal line span the field if the numerical resolution near the boundaries
is already satisfactory. In this case the orthogonal line will terminate
within the field on a streamline. These are considered special points and
they are not used in the curve fits described in Sections 5.2.1 and 5.2.4.
Instead, after the curve fit is obtained, the position, angle, and curvature
at the special points are interpolated.

Another place where this procedure is used is in the positioning of
points adjacent to a stagnation point, as indicated by the solid circle in
Figure 24. In this case the interpolation procedure replaces the integra-
tion of the momentum and continuity equations in the interval containing
the singularity at the stagnation point.

5.3 POSITIONING THE ORTHOGONALS

The cross-stream momentum and continuity equations are written in a
direction normal to the streamlines. Hence, before these equations are ap-
plied, it is necessary to move the grid points along the streamlines to ob-
tain orthogonality. This is easily accomplished as follows (refer to Figure
26). In each region a boundary or dividing streamline is chosen as a "control"
streamline. Along this line the spacing between orthogonals is chosen pro-
portional to $\Delta\xi_1$. To correct the nonorthogonality, the points on each orthog-
onal are first fitted with a spline (using the equations of Section 5.2 and
the end condition $F = 0$) to obtain the angles ϕ_2. The angle deviation from
the streamline normals is then integrated with respect to the cross-stream
distance n, from the control streamline to the point in question, to obtain
the relative movement D_s. The points are then moved to the new positions by
utilizing the streamline curve-fit equations. The coordinates, ϕ_1 angles,
curvatures, and cumulative s-distances are modified as appropriate. The
constant of integration, A_{DS}, in the integral for D_s positions the orthog-
onal on a control streamline so that a reference position is maintained.

5.4 FAR-FIELD SOLUTION

The boundary condition on the external flow is that the velocity approach
the undisturbed velocity, V_∞, and the flow angularity approach zero as the
spacial coordinates approach infinity. To economically meet this condition,
the field is divided into an "inner" and an "outer" region, illustrated in
Figure 27. The inner region is the region near the body where flow distur-
bances are large and/or the typical nonlinear transonic effects are encoun-
tered. Flow properties in this inner region are calculated by the streamtube
curvature technique which uses the full nonlinear equations of motion.

The outer region is the region extending from the outside edge of the
STC integration domain to infinity. In this region, an asymptotic form of
the equations of motion is applied. These asymptotic equations are solved
analytically. On the interface boundary between the two regions, it is re-
quired that the velocities, as calculated in the two separate regions, must
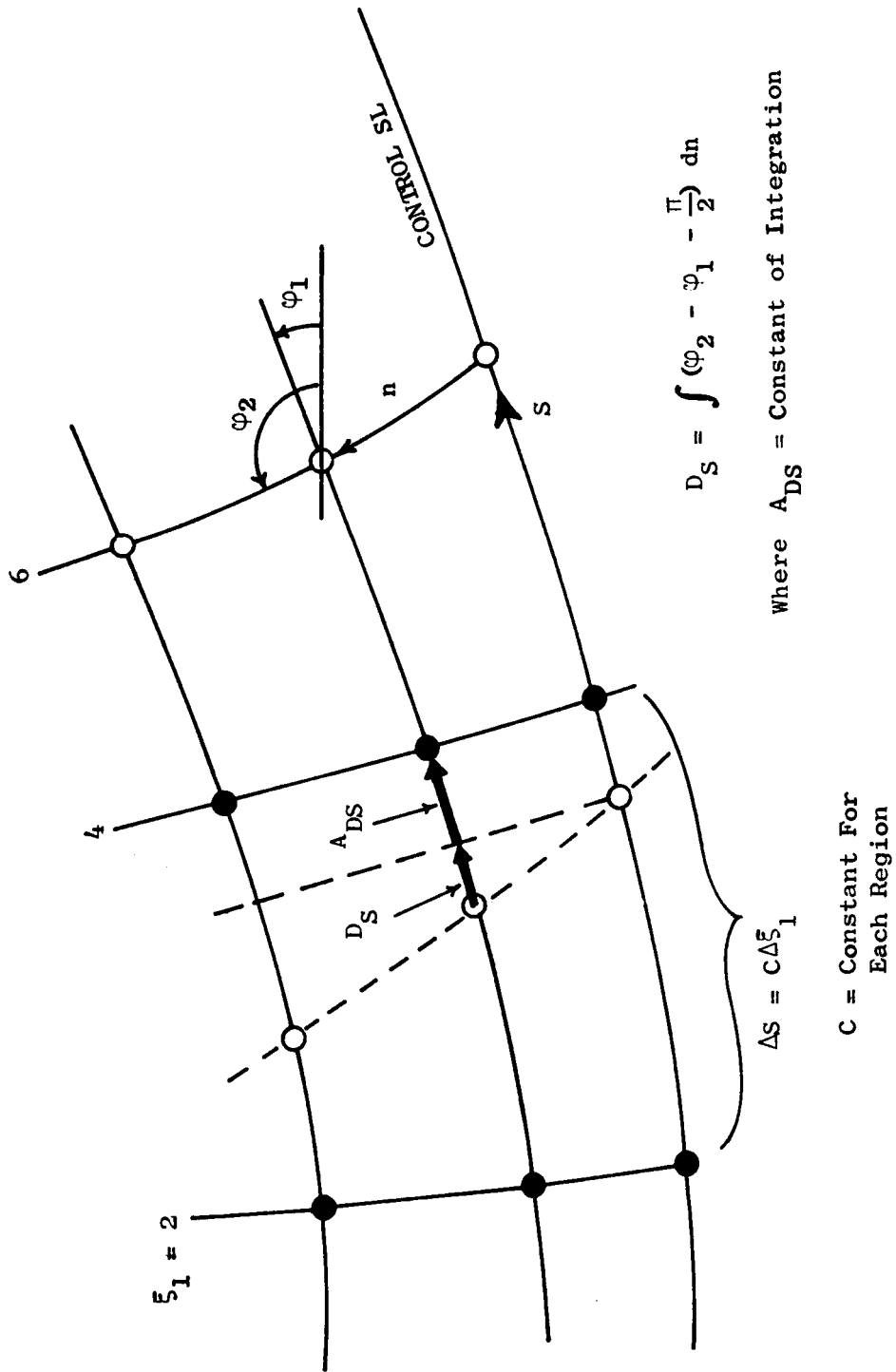
Figure 26. General Positioning of the Orthogonals and Point Movement for Obtaining Lines Normal to the Streamlines.

$$D_S = \int \left(\varphi_2 - \varphi_1 - \frac{\pi}{2} \right) dn$$

Where A_{DS} = Constant of Integration

$\Delta S = C \Delta \xi_1$

C = Constant For Each Region
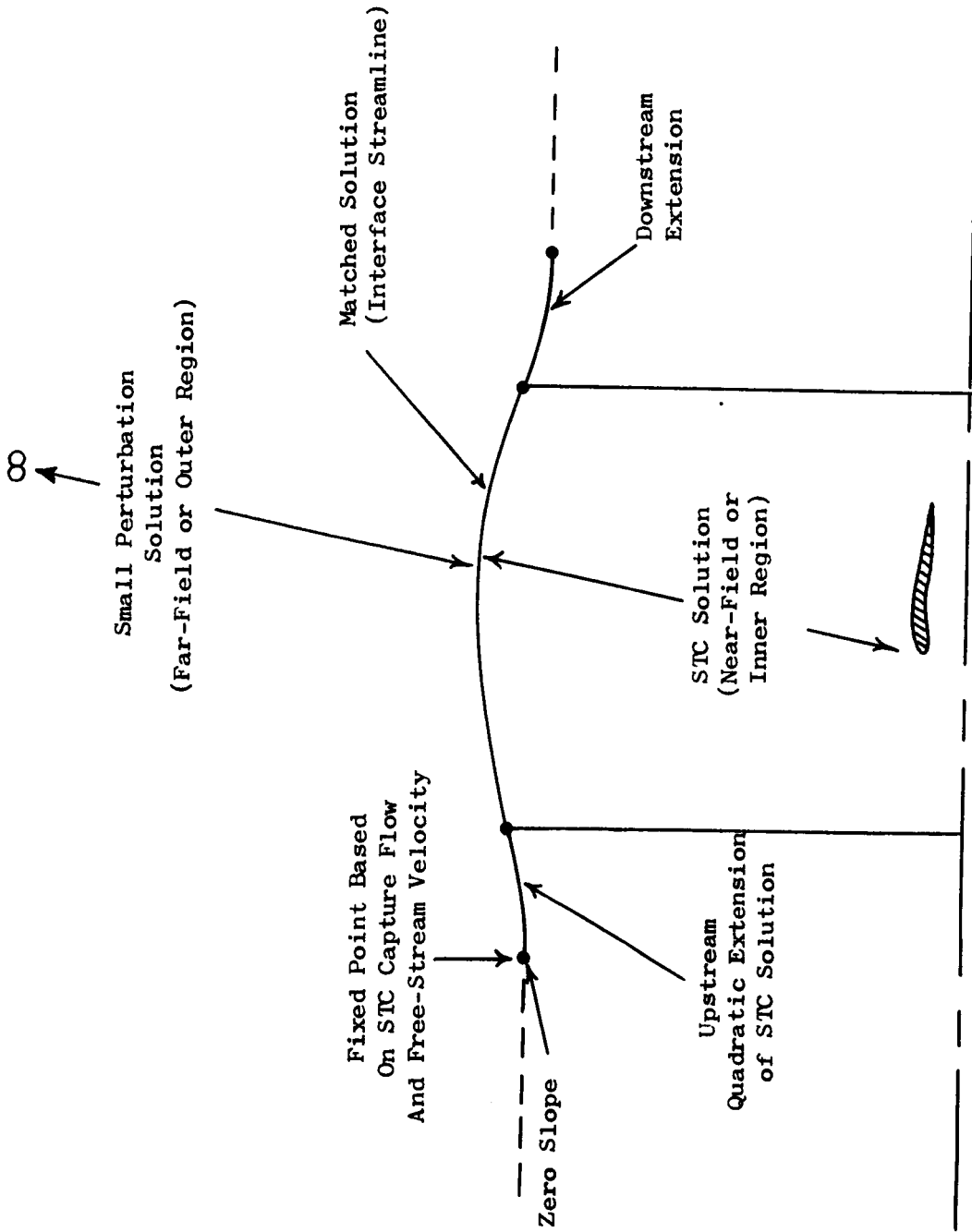
Figure 27. Illustration of Far-Field and Near-Field Solution Domain.

49

match in both magnitude and direction. Consequently both the velocity on the boundary and the shape of the boundary are matched. This manner of applying the boundary condition is analogous to the familiar inner-outer expansion method of asymptotic theory (ref. 6).

To achieve a matched solution on the interface boundary, there are really two questions to be answered. First, for a particular interface streamline shape, what is the velocity distribution? The determination of this velocity distribution is the fifth step in the calculation procedure outlined in Section 3.0, and these velocities are used as boundary conditions on the momentum equation in the sixth step. The second question is: if the interface streamline position is altered slightly (by moving the points outward or inward), what will be the change in velocity at any given point? This is required in the matrix formulation of the streamline correction equation, Section 5.6.4. In this section only the first question is considered.

In the present procedure, the far-field region is approximated by a linear differential equation, the solution to which can be computed very rapidly. The linear formulation, however, also requires that the disturbance of β^2 be small in the outer region compared to the free-stream value, β_∞^2, where $\beta^2 = (1-M^2)$. Thus, the far-field boundary must be sufficiently far from the body to satisfy this condition. (Alternate far-field solution procedures which allow a relatively large β_2 disturbance could, perhaps, be employed as mentioned at the end of this section.)

The calculation method is a simplified version of the Douglas-Neumann procedure which was developed by Smith and co-workers (refs. 7 and 8) at the Douglas Aircraft Company. Two separate versions of the analysis have been formulated, one for axisymmetric flow, the other for two-dimensional flow. Both of these analyses are similar in nature, but the mathematics of the two-dimensional solution is much simpler. In fact, the two-dimensional analysis degenerates to a simple thin airfoil calculation. Because it is simpler, the two-dimensional analysis will be presented first.

Since the "body" of interest in the outer region really represents the outer streamline of the STC numerical integration domain, it is reasonable to expect that its "thickness" (i.e., the vertical displacement of the interface streamline from its undisturbed state) will be small. Further, all angles on the "body" surface (i.e., flow angles on the interface streamline) are also expected to be small. The assumption of small deflections and angles and the assumption of small transonic effects allows us to use the classical small perturbation equations of subsonic flow theory to describe the outer flow field. Thus, the problem of finding the velocity on a surface which is only slightly perturbed from a straight line is just the thin airfoil problem.

As discussed in any aerodynamics text (for example, see ref. 9, Chapter 7), the velocity potential for the flow past a thin airfoil is governed by the equation:

$$\beta^2 \frac{\partial^2 \Phi}{\partial x^2} + \frac{\partial^2 \Phi}{\partial y^2} = 0 \tag{28}$$

which can be converted to Laplace's equation, $\nabla^2 \Phi = 0$, by a Prandtl-Glauert transformation. The solution, for the thin airfoil approximation, is obtained by putting a series of mass sources on the original unperturbed straight line and matching the velocity tangency condition there rather than on the actual perturbed boundary which describes the body shape. We can then write the solution for the velocity potential, Φ, and the perturbation velocities $u-u_\infty$ and v as:

$$\Phi(x,y) = \frac{1}{\beta\pi} \int_{LE}^{TE} \sigma(\xi) \ln\left[(x-\xi)^2 + \beta^2(y-\eta)^2\right]^{\frac{1}{2}} d\xi \tag{29}$$

$$u-u_\infty = \frac{\partial \Phi}{\partial x} = \frac{1}{\beta\pi} \int_{LE}^{TE} \frac{\sigma(\xi)(x-\xi)}{(x-\xi)^2 + \beta^2(y-\eta)^2} d\xi \tag{30}$$

$$v = \frac{\partial \Phi}{\partial y} = \frac{1}{\pi} \int_{LE}^{TE} \frac{\sigma(\xi)\beta(y-\eta)}{(x-\xi)^2 + \beta^2(y-\eta)^2} d\xi \tag{31}$$

where ξ, η is the location of the source point and where x, y is the field point at which the potential (or velocity) is being calculated.

In the case of the far field, all mass sources are placed on the straight line which corresponds to the undisturbed interface boundary. We are interested in finding the velocity on this same line. Thus all calculations are made on the line $\eta = y_s$. (The subscript, s, refers to the location of the undisturbed interface streamline.) The velocity distribution on the body can be found by evaluating Equation 30 at $y = y_s$, and $\eta = y_s$. Thus, we have:

$$u(x,y_s)-u_\infty = \frac{1}{\beta\pi} \int_{LE}^{TE} \frac{\sigma(\xi)d\xi}{(x-\xi)} \tag{32}$$

We now subdivide the interface streamline into a series of N equally spaced intervals. Thus the integral in Equation 32 becomes the summation of N integrals:

$$u(x,y_s)-u_\infty = \frac{1}{\beta\pi} \sum_{j}^{N} \sigma(x_j) \int_{x_{j-\frac{1}{2}}}^{x_{j+\frac{1}{2}}} \frac{d\xi}{x-\xi} \tag{33a}$$

Performing the indicated integration and writing the field point x as the subscripted point x_i, we have:

$$u(x_i, y_s) - u_\infty = \frac{1}{\beta\pi} \sum_{\substack{j \\ j \neq i}}^{N} \sigma(x_j) \ln\left(\frac{x_{j-\frac{1}{2}} - x_i}{x_{j+\frac{1}{2}} - x_i}\right) \qquad (33b)$$

The sum of integrals in Equation 33a includes one integral in which the integrand is singular, namely that interval in which x_i lies. By considering the Cauchy principal value of the integral in this interval, it can be shown that the singular interval's contribution to the velocity is zero. For this reason, the summation in Equation 33b indicates that the interval $j=i$ is to be discarded when calculating the velocity.

A shorthand notation for some of the terms in Equation 33b is now introduced. Let:

$$X_{ij} = \frac{1}{\beta\pi} \ln\left(\frac{x_{j-\frac{1}{2}} - x_i}{x_{j+\frac{1}{2}} - x_i}\right) \qquad (34)$$

so that Equation 33b becomes:

$$u_i - u_\infty = X_{ij} \sigma_j \qquad (35)$$

where u_i and σ_j represent $u(x_i, y_s)$ and $\sigma(x_j)$, respectively.

Determination of the source density is simple in the two-dimensional case. The density is given by:

$$\sigma_j = 2v_j \qquad (36)$$

where v is the vertical component of velocity on the body. This relationship can be obtained from Equation 31 by a careful consideration of the limiting process as y approaches the location of the source, η. Again, the derivation can be found in standard aerodynamic texts. By using the small perturbation assumptions:

$$v = u_\infty \left(\frac{dy}{dx}\right)_s \qquad (37)$$

Finally, for reasons which will become apparent in the axisymmetric analysis, Equations 36 and 37 are combined to define the matrix Y_{ij} such that:

$$\left(\frac{dy}{dx}\right)_{i,s} = Y_{ij} \sigma_j \qquad (38)$$

where Y_{ij} is a diagonal matrix.

We now combine Equations 35 and 38 to obtain a direct equation for the u-velocity component:

$$u_i - u_\infty = X_{ij} \left[Y_{jk}^{-1} \left(\frac{dy}{dx} \right)_{s,k} \right] \qquad (39a)$$

or:

$$u_i - u_\infty = Z_{ij} \left(\frac{dy}{dx} \right)_{sj} \qquad (39b)$$

where,

$$Z_{ij} = X_{ik} Y_{kj}^{-1} \qquad (40)$$

Of course in the thin airfoil approximation where Y_{ij}^{-1} (like Y_{ij}) is a diagonal matrix, Z_{ij} is identical to X_{ij} except for a constant.

It is interesting to note that if the sources were placed on the body surface instead of on the line $y = y_s$, the matrix Y_{ij} would be a completely dense matrix so that finding its inverse would not be trivial. However, for very thin bodies, the off-diagonal terms are very small; i.e., the matrix is strongly diagonally dominant; and, in the limit of a very thin body, Y_{ij} will approach a diagonal matrix. (In the axisymmetric analysis, the matrix Y_{ij} will also be a completely dense matrix.) Placing the source distribution on the body surface, makes the two-dimensional analysis identical with the Douglas-Neumann analysis (ref. 7).

During the iteraction procedure for the Streamtube Curvature solution, the matrix Z_{ij} is calculated only once. Thus, even though the "body" (i.e., the interface streamline) changes shape, the matrix Z_{ij} remains unaffected. This is because the thin airfoil approximation allows sources and the tangency condition to be placed on the straight line $y = y_s$, not on the perturbed interface streamline. The entire effect of the body geometry enters through the vector, $(dy/dx)_{sj}$, which represents the slopes of the body surface.

Before the calculation procedure can be implemented, the upstream and downstream limits of the integration must be specified. We have chosen to place the "leading" and "trailing" edges of the interface streamline upstream and downstream of the numerical (inner) integration boundaries, respectively. This spanwise lengthening of the outer domain over the inner domain is done to ensure that the velocities which are calculated by the outer analytical solution are reasonable and well-behaved at the streamwise extremities of the STC (numerical) integration domain. To allow the streamwise extension of the interface streamline, a quadratic addition is fitted to both ends of the STC-calculated interface streamline. These quadratics are defined by requiring that they have both zero deflection and zero slope at their outer ends, and

that they join continously (but allowing discontinuities in slope) with the ends of the STC streamline.

The analysis of the axisymmetric version of the analytic outer region solution is identical in philosophy to that of the two-dimensional solution. The generation of the matrices X_{ij}, Y_{ij}, and Z_{ij}, however, is more complicated. The details of the axisymmetric analysis have been given by Smith and Pierce (ref. 7). Consequently, only the results will be included here.

In axisymmetric flow, the interface streamline cannot be thought of as a thin airfoil, and it certainly cannot be considered to be a slender body. Instead, the interface streamline appears as an outward perturbation on what would otherwise be a right circular cylinder. As in two-dimensional flow, we assume that a series of mass sources can be placed on the straight surface of the cylinder itself rather than exactly on the interface streamlines. These sources must not be simple mass sources, but rather must be "ring" sources. The potential field which is induced by a ring source of radius a, at the axial location ζ, is:

$$d\Phi(Z,r) = 2a\sigma d\zeta \int_o^\pi \frac{d\theta}{\left[(z-\zeta)^2 + r^2+a^2 - 2ar\cos\theta\right]^{\frac{1}{2}}} \tag{41}$$

By placing a continuous distribution of these sources on the cylinder $r = a$, and then breaking it up into a number of small segments as in the two-dimensional case, we obtain the following equations for the matrices X_{ij}, Y_{ij} (see refs. 7 and 8):

$$X_{ij} = -4a \int_{j-\frac{1}{2}}^{j+\frac{1}{2}} \frac{E(m)\ d\zeta}{\left[4a^2 + (z_{i-\zeta})^2\right]^{\frac{1}{2}} (z_{i-\zeta})} \qquad (i \neq j) \tag{42}$$

$$X_{ij} = 0 \qquad (i=j)$$

and:

$$Y_{ij} = -2 \int_{j-\frac{1}{2}}^{j+\frac{1}{2}} \frac{K(m) - E(m)}{\left[4a^2 + (z_i-\zeta)^2\right]^{\frac{1}{2}}}\ d\zeta \qquad (i \neq j) \tag{43}$$

$$Y_{ij} = -2\pi + 2D \ln\frac{D}{8} - \frac{D^3}{8}\left(1 + \ln\frac{D}{8}\right) \qquad (i=j)$$

where:

$$m = \frac{4a^2}{4a^2 + (z_i-\zeta)^2} \quad , \quad D = \frac{z_{i+\frac{1}{2}} - z_{i-\frac{1}{2}}}{2a}$$

and where $K(m)$ and $E(m)$ are the complete elliptic integrals of the first and second kind, respectively.

As in the two-dimensional theory, we now calculate the u component of the velocity in the outer region from Equation 39b:

$$u_i - u_\infty = Z_{ij}\left(\frac{dr}{dz}\right)_{sj} \qquad \text{(repeat of Equation 39b)}$$

where, as before:

$$Z_{ij} = X_{ik} \, Y_{kj}^{-1} \qquad (44)$$

Note in this axisymmetric case, that Y_{kj} is not a diagonal matrix, and that Y_{kj}^{-1} must be found from a numerical matrix inversion algorithm. However, the only geometrical terms which enter the Y_{ij} matrix are the undisturbed radius of the outer streamline and the total axial length of the outer region. Again, as in the two-dimensional theory, the effects of the displacement of the interface streamline enter only through the vectors $(dy/dx)_{sj}$. This is a direct result of placing the ring sources at the constant radius a, rather than exactly on the interface streamline itself. Consequently, the Z_{ij} matrix can again be calculated once for an entire STC iteration history, despite the fact that the shape of the interface streamline is changing.

It is helpful to compare the approximations in the above formulation to those of Murman and Cole (refs. 1 and 10). Their formulation is similar to the one described above, except that their solution domain includes both the near and far fields. They include the nonlinear term by means of a series of transonic sources distributed throughout the numerical integration domain. But in the region which corresponds to the far field, the transonic source terms are neglected. (In fact, they cannot be included because the information required to compute the distributed source strength is not available.) Therefore, their method, like the method presented here, neglects the nonlinear effects in the outer region.

Despite these justifications, some inclusion of the nonlinear effects in the far-field solution would be advantageous. The local linearization method of Sprieter (refs. 11 and 12) would allow these effects to be included in an approximate manner, and could be included in future program development activity.

Typical results of the far-field matched solution are now illustrated. As anticipated, the proximity effect of the numeric field outer boundary is small when the analytic far-field solution is employed. Figure 28 illustrates the variation of peak Mach number on a body of revolution as the position of the outer boundary is changed. Notice that, for this test case, the induced Mach number error is less than 0.01, even when the outer boundary is reduced to twice the body radius ($R_{outer} = 1.0$).

Also illustrated in Figure 28 are the solutions obtained by utilizing hard wall and constant pressure boundary conditions as a function of R_{outer}.
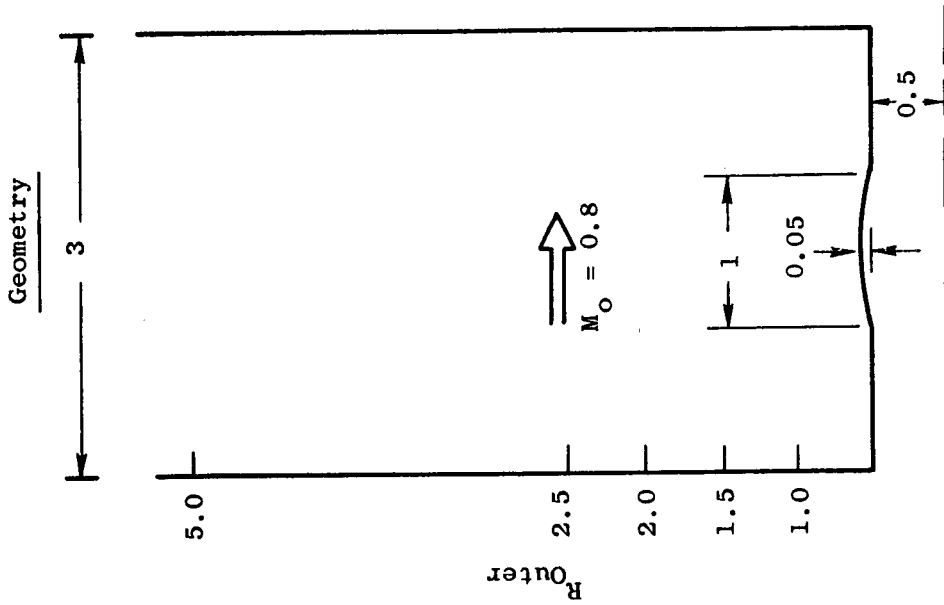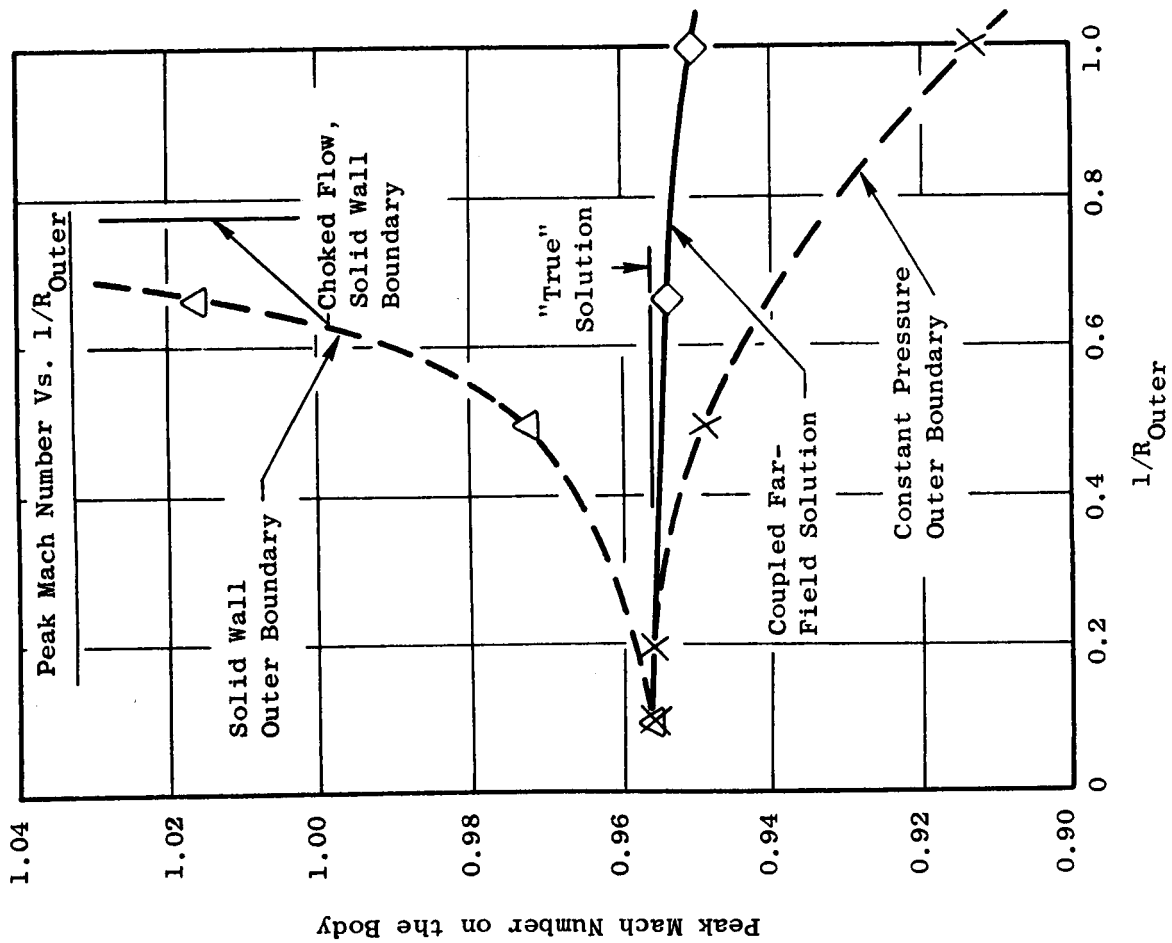
Figure 28. Peak Mach Number for Far-Field, Constant Pressure, and Solid Wall Boundaries.

By comparison, the utilization of the far-field solution allows a significant reduction of boundary radius, for the same accuracy, yielding an efficient computational procedure.

5.5 INTEGRATION OF THE CONTINUITY AND MOMENTUM EQUATIONS

In this section the numerical procedure for integrating the full non-isentropic and variable energy form of the equations of motion is developed. Only a portion of this generality is required, since external flows are isoenergetic and only slight entropy variations arise downstream of shock waves. For completeness, however, the formulation for general flow properties is retained.

The "heart" of the STC method is the integration of the momentum and continuity equations, which are repeated here:

Momentum:

$$\frac{1}{2} \frac{\partial (V^2)}{\partial n} = -CV^2 + \frac{\partial H}{\partial n} - T\frac{\partial S}{\partial n} \tag{2b}$$

Continuity:

$$\partial A = \frac{\partial W}{\rho V} \tag{1}$$

Equation 2b is the basic Crocco form of the momentum equation containing the variables H and S (enthalpy and entropy). These variables may be replaced by total temperature and total pressure for greater engineering convenience. If it is also assumed that the specific heat is constant, then the following equation is equivalent to Equation 2b:

$$\frac{1}{2} \frac{\partial (V^2)}{\partial n} = -CV^2 + \frac{1}{2} \frac{V^2}{T_T} \frac{\partial T_T}{\partial n} + \frac{R_g T}{P_T} \frac{\partial P_T}{\partial n} \tag{45}$$

The above momentum equation is integrated by parts. First, we rewrite Equation 45 as:

$$\frac{1}{2} dv^2 = \frac{1}{2} V^2 \left(-2Cdn + d\ln T_T \right) + R_g T \frac{dP_T}{P_T} \tag{46}$$

The formula for integrating by parts is:

$$dv = -\frac{v}{u} du + \frac{1}{u} d(uv) \tag{47}$$

By comparing Equation 47 with Equation 46, it follows that:

$$v = \frac{1}{2} V^2 \tag{48a}$$

$$\frac{du}{u} = 2Cdn - dlnT_T \tag{48b}$$

and,

$$\frac{1}{u} d(uv) = R_g T \frac{dP_T}{P_T} \tag{48c}$$

Since the total temperature and streamline curvature are assumed known, Equation 48b can be integrated from the first to the kth streamline to obtain:

$$u_k = \frac{T_{T_1}}{T_{T_k}} e^{2\int_1^k Cdn} \qquad (u_1 = 1) \tag{49}$$

Equation 48c is then integrated to yield an expression for the product of u and velocity squared.

$$\frac{1}{2} u_k V_k^2 - \frac{1}{2} u_{k+1} V_{k+1}^2 = \int_{k+1}^k u R_g T \frac{dP_T}{P_T} \tag{50}$$

Equation 50 represents the integration across one streamtube bounded by streamlines k and k+1. The integration is performed from the outside toward the center because, frequently, the velocity is known on the outside boundary. The finite-difference form of Equation 50, employed in the computer program, is:

$$u_k V_k^2 - u_{k+1} V_{k+1}^2 = \sqrt{u_k u_{k+1}} \ R_g \left(\frac{T_k}{P_{T_k}} + \frac{T_{k+1}}{P_{T_{k+1}}} \right) \left(P_{T_k} - P_{T_{k+1}} \right) \tag{51}$$

Note that this expression is explicit when no total pressure gradient exists; otherwise the expression (Equation 51) is implicit because the static temperature which appears on the right-hand side is a direct function of velocity.

$$T_k = T_{T_k} - \frac{V_k^2}{2C_p} \tag{52}$$

However, the implicit nature is very weak up to transonic speeds, and a simple successive approximation procedure is utilized to update the right-hand side until the computed fractional velocity change (on each streamline) is less than 1×10^{-5}.

The numerical integration of the momentum equation, then, is a two-step process: first the integration of Equation 49 is performed followed by the integration of Equation 50. In Equation 49, the integral of curvature is evaluated by fitting a second-order polynominal in each interval. (The second derivative of that polynominal is established by a least square fit to the two nearby points.) Implied in the integration is the fact that total temperature and total pressure are known as a function of the streamline index k and, hence, as a function of the cross-stream distance n_o. This is in slight contradiction to the streamwise momentum and energy equations, Equations 3 and 4 of Section 2.0, since total properties are correctly related only to the cumulative flow rate ($\Psi = W$). However, this slight error is automatically corrected in the later stages of the iteration when the assumed streamline positions are effectively coincident with the true streamlines.

As noted above, the integration starts from the outer boundary and proceeds inward. For external flows, the velocity on the outer boundary is obtained from the far-field equations of Section 5.4. For internal channels, this outer boundary velocity is found iteratively as will be discussed below. Velocity changes across slip lines are obtained by Equations 8a, 8b, and 8c as discussed previously.

Following the momentum equation, the continuity equation is integrated by the algorithm:

$$A_{k+1} - A_k = \frac{W_{k+1} - W_k}{\langle \rho V \rangle} \tag{53a}$$

The average value of mass flow per unit area, in the denominator of Equation 53a, may be approximated two ways:

$$\langle \rho V \rangle = \frac{1}{2} \left[(\rho V)_k + (\rho V)_{k+1} \right] \tag{53b}$$

$$\langle \rho V \rangle = \left[(\rho V)_k \, (\rho V)_{k+1} \right]^{\frac{1}{2}} \tag{53c}$$

If the variation of (ρV) between streamlines is small, then the two expressions give similar results. Although Equation 53b is somewhat faster to compute, Equation 53c has been found more reliable for some special cases. Consequently, an approximation to Equation 53c is employed in the computer code.

If the cumulative cross-stream areas are being computed for an internal station, it is required that the last area, A_N, equal the geometric area of the passage at that location. To accomplish this, the value of V_N used as an initial condition in the momentum integration is varied. Figure 29 shows a typical variation of Area, A_N, with velocity, V_N. Obviously, there are two solutions -- one for the subsonic branch and another for the supersonic branch. Although the choice of branch may be controlled by user input, the subsonic branch solution is always employed with an inlet/nacelle configuration.
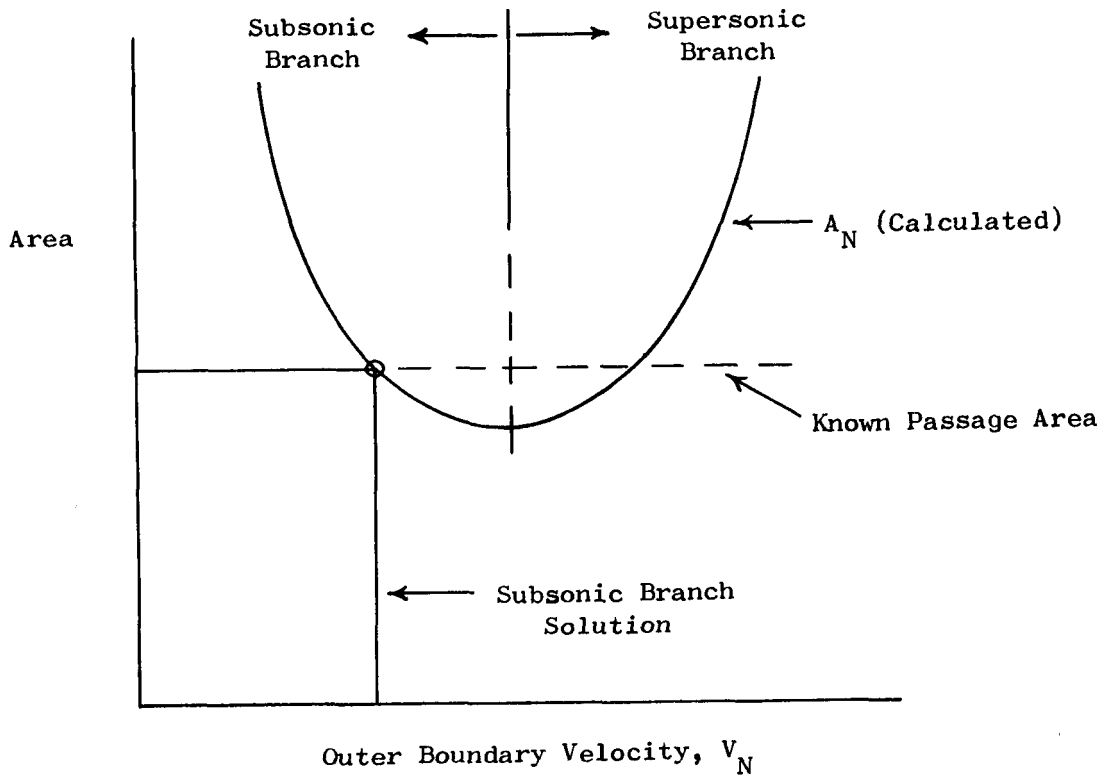
Figure 29. Illustration of Method for Choosing Outer Boundary
Velocity in a Confined Passage.

A third possibility is that the geometric passage area is below the minimum computed area, A_N. In this case, the flow is said to be choked, and the flow is adjusted so that the minimum calculated area will be exactly equal to the geometric area. This logic is utilized, for example, in the throat of the nozzle discharge passage.

5.5.1 Stagnation Points

If a sharp concave corner is encountered, the flow velocity is known to be zero. Such a situation cannot easily be handled with the equations as formulated above. Hence, the integration of both the momentum and continuity equations is omitted in the interval adjacent to the body, and the first point away from the body is interpolated as indicated in Section 5.2.6.

To replace the omitted equations at the leading edge stagnation point, the derived condition that the stagnation streamline intersect the body at a 90° angle is utilized as discussed in Section 5.2.3. The streamline angle at the stagnation point is, of course, double valued. Consequently, the orthogonal line which passes through the stagnation point is made perpendicular to the average of the two angles, a requirement which is derived from potential theory.

5.5.2 Wakes From Blunt Trailing Edges

Because it is much easier to obtain a valid numerical solution if the flow streamlines are smooth and the curvatures are not excessive, a dead region is allowed to exist behind a trailing edge which has thickness. As shown in Figure 30, the thickness of the "dead" region is gradually reduced to zero as one proceeds downstream. The derivative, db/ds, has a nominal value of 0.1.

To include the wake displacement effect, the wake area is added to the right-hand side of Equation 53a if a channel boundary streamline is crossed. In this way the cumulative streamtube flow area includes the wake displacements. No correction is required in the momentum equation because pressure continuity is always enforced across a slip line.

5.6 STREAMLINE CORRECTION EQUATION

5.6.1 General Formulation

In the STC calculation procedure, we start with an estimate of the streamline positions, that is, a set of z_0, r_0. For the second iteration cycle, z_0, r_0 will be the coordinates determined by the first iteration, and so forth. These "assumed" streamline coordinates are used to compute the cumulative width of the streamtubes (n_0), curvature, velocity, and density and, then, a second set of cumulative streamtube widths (n_x). This is illustrated in the following listings:
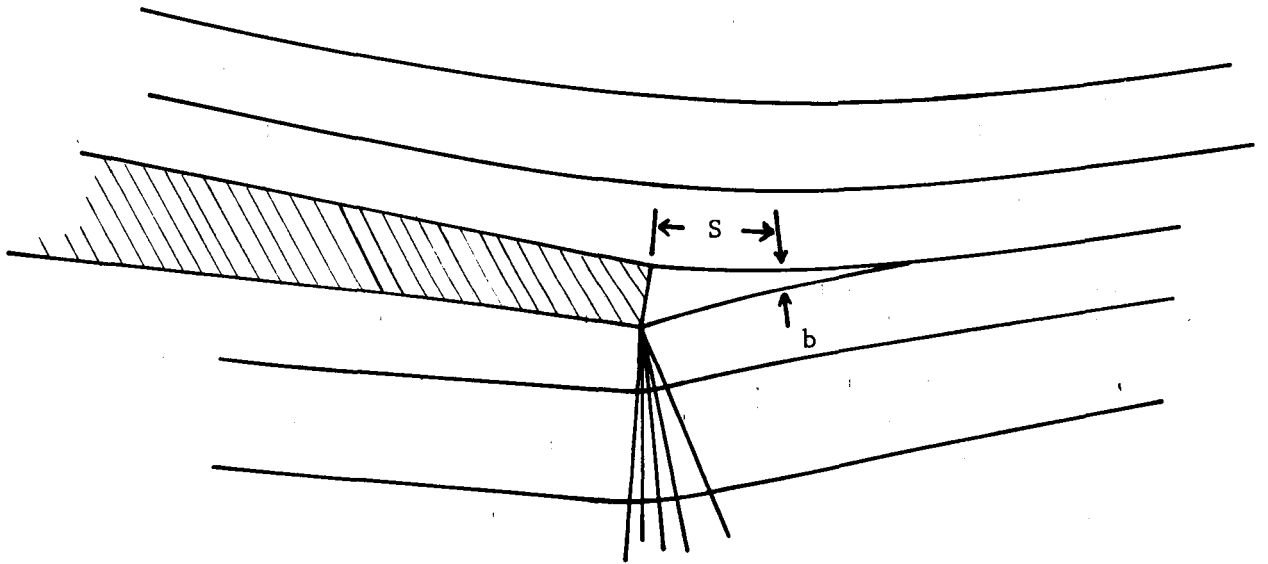
Figure 30. Trailing Edge Region.

Given	Operation	Compute
z_o, r_o	Streamline Curve Fitting	C_o
z_o, r_o	Orthogonal Line Curve Fitting	n_o, A_o
C_o, n_o	Momentum Equation	V_o
V_o	Energy, Entropy, and Eq. of State	ρ_o
ρ_o, V_o	Continuity Equation	A_x, n_x

If n_x equals n_o, the solution is converged. If n_x is different from n_o, then the streamline positions must be adjusted so that the difference between n_x and n_o is reduced. The amount by which the streamlines are to be adjusted is denoted by δn, the equations for which are formulated in the present section.

The calculation formulas to this point have utilized the full nonlinear equations of motion. Now we employ an approximate set of linearized equations which will provide for the computation of δn; and, through repeated application, bring the discrepancy $(n_x - n_o)$ to some small neglectable value. The final coverged flow field solution, of course, will be the solution to the nonlinear equations (i.e., Equations 1 through 4).

The continuity equation for one streamtube may be expressed as:

$$W_{k+1} - W_k = \int_k^{k+1} \rho V dA \cong \langle \rho V \rangle_{k+\frac{1}{2}} \left[A_{k+1} - A_k \right] \tag{54}$$

where,

$A = \int 2 \pi r \, dn$ (axisymmetric)

$A = n$ (plane)

$\langle \rho V \rangle_{k+\frac{1}{2}}$ = average flow per unit area for the streamtube bounded by the k and k+1 streamlines

For two adjacent streamtubes:

$$\frac{A_{k+1} - A_k}{W_{k+1} - W_k} = \frac{1}{\langle \rho V \rangle_{k+\frac{1}{2}}} \tag{55}$$

$$\frac{A_k - A_{k-1}}{W_k - W_{k-1}} = \frac{1}{\langle \rho V \rangle_{k-\frac{1}{2}}} \tag{56}$$

The previous two equations are subtracted to obtain the second difference for A, defined as:

$$\frac{\Delta^2 A}{\Delta W} = \frac{A_{k+1} - A_k}{W_{k+1} - W_k} - \frac{A_k - A_{k-1}}{W_k - W_{k-1}} \qquad (57)$$

$$\frac{\Delta^2 A}{\Delta W} = \frac{1}{\langle \rho V \rangle_{k+\frac{1}{2}}} - \frac{1}{\langle \rho V \rangle_{k-\frac{1}{2}}} \qquad (58)$$

Variables A, ρ, and V (i.e., those without subscripts) will be used in this section to represent the "corrected" (or true solution) values. Thus, Equation 58 represents the "correct" solution.

An equivalent expression can be written to represent the continuity equation which was used to predict the x-subscripted areas from the velocities and densities associated with the assumed streamlines. That is:

$$\frac{\Delta^2 A_x}{\Delta W} = \frac{1}{\langle \rho_o V_o \rangle_{k+\frac{1}{2}}} - \frac{1}{\langle \rho_o V_o \rangle_{k-\frac{1}{2}}} \qquad (59)$$

Equations 58 and 59 are now substituted into the following identity:

$$\frac{\Delta^2 (A-A_o)}{\Delta W} + \frac{\Delta^2 A_x}{\Delta W} - \frac{\Delta^2 A}{\Delta W} \equiv \frac{\Delta^2 (A_x - A_o)}{\Delta W} \qquad (60)$$

to obtain:

$$\frac{\Delta^2 (A-A_o)}{\Delta W} - \left[\frac{1}{\langle \rho V \rangle_{k+\frac{1}{2}}} - \frac{1}{\langle \rho_o V_o \rangle_{k+\frac{1}{2}}}\right] + \left[\frac{1}{\langle \rho V \rangle_{k-\frac{1}{2}}} - \frac{1}{\langle \rho_o V_o \rangle_{k-\frac{1}{2}}}\right] = \frac{\Delta^2 (A_x - A_o)}{\Delta W} \qquad (61a)$$

The difference between the "correct" value and the value associated with the assumed streamlines is denoted by δ ( ). In particular:

$$\delta A = A - A_o$$

$$\delta n = n - n_o$$

$$\delta V = V - V_o$$

$$\delta\left(\frac{1}{\rho V}\right) = \frac{1}{\langle \rho V \rangle} - \frac{1}{\langle \rho_o V_o \rangle}$$

$$\delta C = C - C_o$$

Then Equation 61a can be rewritten:

$$\frac{\Delta^2 \delta A}{\Delta W} - \delta\left(\frac{1}{\rho V}\right)_{k+\frac{1}{2}} + \delta\left(\frac{1}{\rho V}\right)_{k-\frac{1}{2}} = \frac{\Delta^2(A_x - A_o)}{\Delta W} \qquad (61b)$$

This equation represents a difference correction form of the continuity equation.

To eliminate the ρV terms in Equation 61b, the momentum equation is introduced. In regions where the rotationality is zero, the momentum equation is:

$$\frac{\partial V}{V} = -Cdn \qquad (62)$$

As illustrated in Figure 31, the outer boundary of the field is denoted as the Nth streamline; and, it is assumed that, between the kth streamline and the Nth streamline, there is a slip line with index j. Integration of Equation 62 from the kth to the jth streamline and then from the jth to the Nth streamline yields:

$$lnV_N - lnV_{ja} + lnV_{jb} - lnV_k = -\int_k^j Cdn - \int_j^N Cdn = -\int_k^N Cdn \qquad (63)$$

where V_{jb} and V_{ja} are the velocities just below and above the slip line. For the assumed curvatures, C_o, the momentum equation is:

$$lnV_{oN} - lnV_{oja} + lnV_{ojb} - lnV_{ok} = -\int_k^N C_o dn \qquad (64)$$

Equation 63 is subtracted from Equation 64, and it is assumed that the lengths of the orthogonals from k to N are not appreciably different.

$$ln\left(\frac{V}{V_o}\right)_k - ln\left(\frac{V}{V_o}\right)_N = \int_k^N (C-C_o)dn + ln\left(\frac{V}{V_o}\right)_{jb} - ln\left(\frac{V}{V_o}\right)_{ja} \qquad (65)$$

Since $V = V_o + \delta V$ we use:

$$ln\left(\frac{V}{V_o}\right) = ln\left(1 + \frac{\delta V}{V_o}\right) \approx \frac{\delta V}{V_o} \qquad \left(\frac{\delta V}{V_o} \ll 1\right)$$

as a first-order linear approximation, and Equation 65 can be written as follows:

$$\left(\frac{\delta V}{V_o}\right)_k - \left(\frac{\delta V}{V_o}\right)_N = \int_k^N \delta Cdn + \left(\frac{\delta V}{V_o}\right)_{jb} - \left(\frac{\delta V}{V_o}\right)_{ja}$$
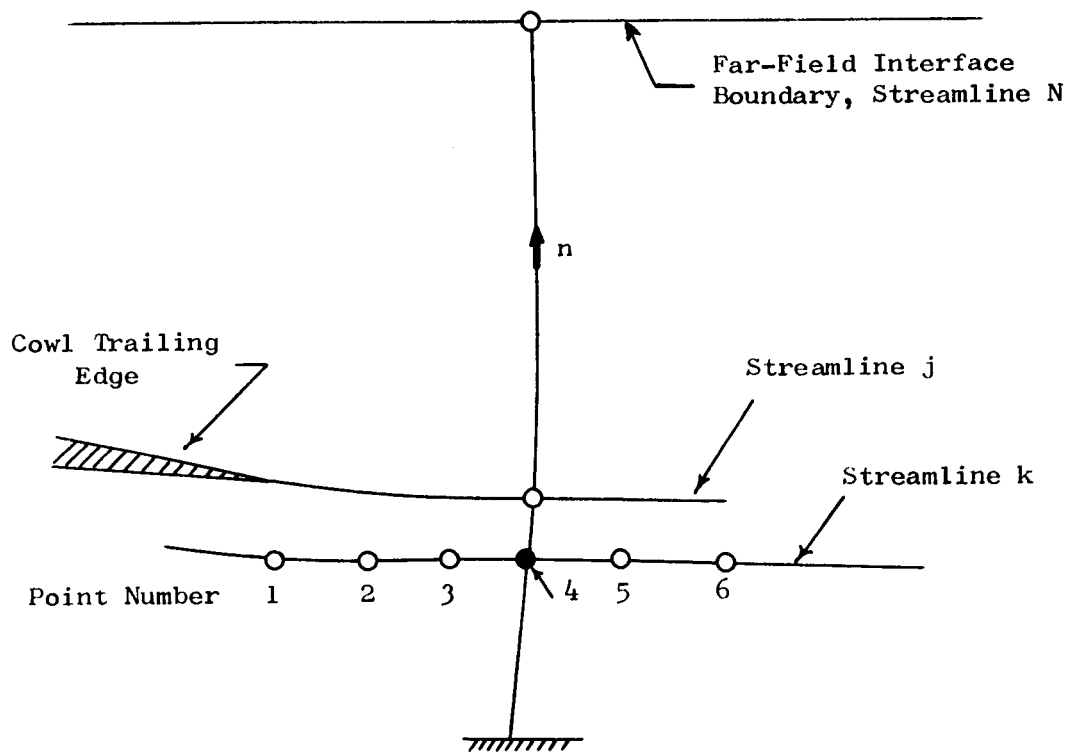
Figure 31. Streamline Subscript Notation.

or,

$$\left(\frac{\delta V}{V_o}\right)_k - \left(\frac{\delta V}{V_o}\right)_N = \int_k^N \delta C dn + \alpha_j \qquad (66)$$

The parameter α_j is introduced to simplify the equations, where:

$$\alpha_j = \left(\frac{\delta V}{V_o}\right)_{jb} - \left(\frac{\delta V}{V_o}\right)_{ja} \qquad (67)$$

Equation 66 is the difference correction form of the momentum equation. With it we can approximate the velocity corrections for the $(k+\frac{1}{2})$ and $(k-\frac{1}{2})$ streamtubes as follows:

$$\left(\frac{\delta V}{V_o}\right)_{k+\frac{1}{2}} = \int_{k+\frac{1}{2}}^N \delta C dn + \left(\frac{\delta V}{V_o}\right)_N + \alpha_j$$

$$\approx \int_k^N \delta C dn - \int_k^{k+\frac{1}{2}} \delta C dn + \left(\frac{\delta V}{V_o}\right)_N + \alpha_j$$

$$\approx \int_k^N \delta C dn - \frac{1}{2}\left(n_{k+1} - n_k\right) \delta C_k + \left(\frac{\delta V}{V_o}\right) + \alpha j \qquad (68a)$$

and

$$\left(\frac{\delta V}{V_o}\right)_{k-\frac{1}{2}} \approx \int_k^N \delta C dn + \frac{1}{2}\left(n_k - n_{k-1}\right) \delta C_k + \left(\frac{\delta V}{V_o}\right) + \alpha_j \qquad (68b)$$

For any given streamline the flow is isentropic, and it can be shown that:

$$d\left(\frac{1}{\rho V}\right) = - \frac{\beta^2}{\rho V} \frac{dV}{V} \qquad (69)$$

where $\beta^2 = 1-M^2$. A discrete linear approximation to Equation 69 is:

$$-\delta\left(\frac{1}{\rho V}\right)_{k+\frac{1}{2}} = \left(\frac{\beta_o^2}{\rho_o V_o}\right)_{k+\frac{1}{2}} \left(\frac{\delta V}{V_o}\right)_{k+\frac{1}{2}} \qquad (70a)$$

and:

$$-\delta\left(\frac{1}{\rho V}\right)_{k-\frac{1}{2}} = \left(\frac{\beta_o^2}{\rho_o V_o}\right)_{k-\frac{1}{2}} \left(\frac{\delta V}{V_o}\right)_{k-\frac{1}{2}} \qquad (70b)$$

Equation 70a is subtracted from Equation 70b, and Equation 68 and 68b are substituted into the result. This yields the following expression for the ρV-terms in the continuity difference correction equation:

$$-\delta\left(\frac{1}{\rho V}\right)_{k+\frac{1}{2}} + \delta\left(\frac{1}{\rho V}\right)_{k-\frac{1}{2}} = \left(\frac{\beta_o}{\rho_o V_o}\right)_{k+\frac{1}{2}} \left[\int_k^N \delta C dn - \frac{1}{2}\left(n_{k+1} - n_k\right) \delta C_k + \left(\frac{\delta V}{V_o}\right)_N + \alpha_j\right]$$

$$- \left(\frac{\beta_o}{\rho_o V_o}\right)_{k-\frac{1}{2}} \left[\int_k^N \delta C dn + \frac{1}{2}\left(n_k - n_{k-1}\right) \delta C_k + \left(\frac{\delta V}{V_o}\right)_N + \alpha_j\right]$$

Rearranging the above, it follows that:

$$-\delta\left(\frac{1}{\rho V}\right)_{k+\frac{1}{2}} + \delta\left(\frac{1}{\rho V}\right)_{k-\frac{1}{2}} = -B_1 \, \delta C_k + B_2\left[\int_k^N \delta C dn + \left(\frac{\delta V}{V_o}\right)_N + \alpha_j\right] \tag{71}$$

where:

$$B_1 = \frac{1}{2}\left[\left(\frac{\beta_o}{\rho_o V_o}\right)_{k+\frac{1}{2}} \left(n_{k+1} - n_k\right) + \left(\frac{\beta_o}{\rho V}\right)_{k-\frac{1}{2}} \left(n_k - n_{k-1}\right)\right] \tag{72a}$$

$$B_2 = \left(\frac{\beta_o}{\rho_o V_o}\right)_{k+\frac{1}{2}} - \left(\frac{\beta_o}{\rho_o V_o}\right)_{k-\frac{1}{2}} \tag{72b}$$

The term α_j, which represents the difference between the velocity correction across a streamline, is now to be evaluated. The definition of α_j, given by Equation 67, is repeated:

$$\alpha_j = \left(\frac{\delta V_b}{V_b} - \frac{\delta V_a}{V_a}\right)_j$$

The subscripts "b" and "a" are used to indicate the value of velocity just below (b) and above (a) the slip line along streamline j; the subscript "o" has been dropped:

$$\alpha_j = \left(\frac{\delta V_a}{V_a}\right)_j \left(\frac{V_a}{V_b} \frac{\delta V_b}{\delta V_a} - 1\right)_j \tag{73}$$

The equations which apply at the slip line are:

$$\frac{1}{2}V_b^2 = C_p\left(T_{Tb} - T_{sb}\right) \tag{74a}$$

$$\frac{1}{2}V_a^2 = C_p\left(T_{Ta} - T_{sa}\right) \tag{74b}$$

$$T_{sb} = T_{Tb} \left(\frac{P_s}{P_{Tb}} \right)^{\frac{\gamma-1}{\gamma}} \tag{75a}$$

$$T_{sa} = T_{Ta} \left(\frac{P_s}{P_{Ta}} \right)^{\frac{\gamma-1}{\gamma}} \tag{75b}$$

These equations are differentiated to obtain:

$$\frac{1}{C_p} V_b \, dV_b = -dT_{sb} = -T_{Tb} \left(\frac{P_s}{P_{Tb}} \right)^{\frac{\gamma-1}{\gamma} - 1} \frac{dP_s}{P_{Tb}}$$

$$\frac{1}{C_p} V_a \, dV_a = -dT_{sa} = -T_{Ta} \left(\frac{P_s}{P_{Ta}} \right)^{\frac{\gamma-1}{\gamma} - 1} \frac{dP_s}{P_{Ta}}$$

Dividing one by the other:

$$\frac{V_b}{V_a} \frac{dV_b}{dV_a} = \frac{T_{Tb}}{T_{Ta}} \left(\frac{P_{Ta}}{P_{Tb}} \right)^{\frac{\gamma-1}{\gamma}} \tag{76}$$

An approximation to Equation 76 is:

$$\frac{V_a}{V_b} \frac{\delta V_b}{\delta V_a} = \frac{V_a^2}{V_b^2} \frac{T_{Tb}}{T_{Ta}} \left(\frac{P_{Ta}}{P_{Tb}} \right)^{\frac{\gamma-1}{\gamma}} \tag{77}$$

and Equation 73 can now be written as:

$$\alpha_j = \left(\frac{\delta V_a}{V_a} \right)_j \left[\frac{V_a^2}{V_b^2} \frac{T_{Tb}}{T_{Ta}} \left(\frac{P_{Ta}}{P_{Tb}} \right)^{\frac{\gamma-1}{\gamma}} - 1 \right]_j \tag{78}$$

Just above the slip line, the velocity variation is given by the integral of the momentum equation (see Equation 66):

$$\left(\frac{\delta V_a}{V_o}\right)_j = \left(\frac{\delta V}{V_o}\right)_N + \int_j^N \delta C \ dn \tag{79}$$

So, αj becomes:

$$\alpha j = \left[\frac{V_a^2}{V_b^2} \ \frac{T_{Tb}}{T_{Ta}} \ \left(\frac{P_{Ta}}{P_{Tb}}\right)^{\frac{\gamma-1}{\gamma}} \ -1\right]_j \left[\left(\frac{\delta V}{V_o}\right)_N + \int_j^N \delta C \ dn\right]$$

$$= B_{3j}\left[\left(\frac{\delta V}{V_o}\right)_N + \int_j^N \delta C \ dn\right] \tag{80}$$

where:

$$B_{3j} = \left(\frac{V_a^2 \ P_{Ta}^{\frac{\gamma-1}{\gamma}}}{T_{Ta}} \middle/ \frac{V_b^2 \ P_{Tb}^{\frac{\gamma-1}{\gamma}}}{T_{Tb}} \ -1\right)_j \tag{81}$$

Equation 81 is now substituted into Equation 71:

$$-\delta\left(\frac{1}{\rho V}\right)_{k+\frac{1}{2}} + \delta\left(\frac{1}{\rho V}\right)_{k-\frac{1}{2}} = - B_1 \delta C_k + B_2 \int_k^N \delta C \ dn + B_2 \left(1 + B_{3j}\right)\left(\frac{\delta V}{V_o}\right)_N +$$

$$B_2 B_{3j} \int_j^N \delta C \ dn$$

And this result is substituted into Equation 61b:

$$\frac{\Delta^2(\delta A)}{\Delta W} - B_1 \delta C_k + B_2 \int_k^N \delta C \ dn + B_2 \left(1 + B_{3j}\right)\left(\frac{\delta V}{V_o}\right)_N + B_2 B_{3j} \int_j^N \delta C \ dn$$

$$= \frac{\Delta^2(A_x - A_o)}{\Delta W} \tag{82}$$

where, again:

$$B_1 = \frac{1}{2} \left[\left(\frac{\beta_o}{\rho_o V_o}\right)_{k+\frac{1}{2}} \left(n_{o_{k+1}} - n_{o_k}\right) + \left(\frac{\beta_o}{\rho_o V_o}\right)_{k-\frac{1}{2}} \left(n_{o_k} - n_{o_{k-1}}\right)\right]$$

$$B_2 = \left(\frac{\beta_0}{\rho_0 V_0}\right)_{k+\frac{1}{2}} - \left(\frac{\beta_0}{\rho_0 V_0}\right)_{k-\frac{1}{2}}$$

$$B_{3j} = \left(\frac{V_0^2 \, P_T^{\frac{\gamma-1}{\gamma}}}{T_T}\right)_{ja} \left(\frac{V_0^2 \, P_T^{\frac{\gamma-1}{\gamma}}}{T_T}\right)_{jb}^{-1} - 1$$

Equation 82 is the desired correction equation. The coefficients B_1, B_2, and B_{3j} are all based on flow properties calculated from the assumed curvatures. They are known quantities. The unknown quantities are δA, δC, and the velocity variation on the outer boundary δV_N. Each of these quantities must be expressed in terms of δn.

Remember that for axisymmetric flow:

$$\delta A = 2\pi \, r_0 \, \delta n \tag{83a}$$

and for plane flow:

$$\delta A = \delta n \tag{83b}$$

Thus, for axisymmetric flow, the second difference of δA is:

$$\frac{\Delta^2(\delta A)}{\Delta W} = 2\pi \left(\frac{r_{k+1}\,\delta n_{k+1} - r_k\,\delta n_k}{W_{k+1} - W_k} - \frac{r_k\,\delta n_k - r_{k-1}\,\delta n_{k-1}}{W_k - W_{k-1}}\right) \tag{84a}$$

and for planar flow:

$$\frac{\Delta^2(\delta A)}{\Delta W} = \frac{\delta n_{k+1} - \delta n_k}{W_{k+1} - W_k} - \frac{\delta n_k - \delta n_{k-1}}{W_k - W_{k-1}} \tag{84b}$$

The curvature correction is:

$$-\delta C_k \approx \frac{D^2(\delta n k)}{Ds2}$$

where s is the curvilinear distance measured along the kth streamline. For any selected curve fit (or finite difference second-derivative formula), the influence coefficients can be represented as follows:

$$\frac{D^2(\delta n_k)}{Ds^2} = G_1 \delta n_{1,k} + G_2 \delta n_{2,k} + G_3 \delta n_{3,k} + G_4 \delta n_{4,k} + G_5 \delta n_{5,k} \qquad (85)$$

$$+ G_6 \delta n_{6,k}$$

Here the numbering scheme shown in Figure 31 has been used. Generally the influence coefficients, G, are computed by assuming a spline curve representation. If the velocity is subsonic, a central point difference equation is used; and, if the velocity is supersonic, a backward difference parabola equation is used.

With Equations 84 and 85 substituted into Equation 82, there results a set of equations for the variables $\delta n_{i,k}$ where i is an orthogonal line index and k is the streamline index. These equations, together with the boundary condition equations presented below, form a solvable set of linear simultaneous equations.

However, this resulting equation is quite cumbersome. The integral terms which appear in Equation 82 lead to a dense coefficient matrix and a computer solution is impractical. Therefore, the terms in Equation 82 which have coefficients B_2 and B_3 are neglected, and the following approximate form of the correction equation is utilized:

$$\frac{\Delta^2(\delta A)}{\Delta W} + B_1 \frac{D^2(\delta n)}{Ds^2} = \frac{\Delta^2(A_x - A_0)}{\Delta W} \qquad (86a)$$

This form is equivalent to the differential form of the correction equation derived in Appendix A. For most flow conditions Equation 86a produces rapid convergence. Hence, the omitted terms seem unnecessary for these cases. In a few cases the direct use of Equation 86a does lead to divergence. This is surmounted by correcting the streamline position by an amount smaller than the calculated δn, or by utilizing an additional factor ρ_c in Equation 86a where ρ_c is a constant which is greater than or equal to unity.

$$\frac{\Delta^2(\delta A)}{\Delta W} + \rho_c B_1 \frac{D^2(\delta n)}{Ds^2} = \frac{\Delta^2(A_x - A_0)}{\Delta W} \qquad (86b)$$

The effect of setting ρ_c to a value larger than one, say 1.5 or 2.0, is to reduce the curvature change between successive iterates and in an approximate manner account for the items which were dropped from Equation 82.

5.6.2 Flow Inlet and Flow Exit Boundaries

Options are provided for two types of boundary conditions at the upstream and downstream field boundaries. Either the flow angle can be specified or the curvature can be specified. The recommended boundary condition for general usage is that the curvature is zero (or, equivalently, the static

pressure is constant). In either case, Equation 86a is applicable. However, for an upstream boundary, the coefficients G_1, G_2 and G_3 in Equation 85 will all be zero. That is, the curvature correction at the central point will be related to the downstream points 4 and 5 only. If a curvature boundary condition is employed, then the curvature correction necessarily will be zero. Hence, all the G coefficients are zero, and the equation is:

$$\frac{\Delta^2(\delta A)}{\Delta W} = \frac{\Delta^2(A_x - A_o)}{\Delta W} \tag{87}$$

The solution to this equation is simply:

$$\delta A = A_x - A_o \tag{88}$$

5.6.3 Body Surface Points

The correction equation for the grid points on a body contour is trivial. The streamlines are already correctly positioned so:

$$\delta n = 0 \tag{89}$$

for each such point.

5.6.4 The Far-Field Interface Streamline Correction Equation

In this section the correction equation for a constant pressure or far-field boundary is formulated. The notation is similar to that of Section 5.6.1 and is illustrated in Figure 32.

Again we begin with the continuity equation. The desired solution is

$$\left(A_N - A_{N-1}\right) \left\langle \rho V \right\rangle_{N-\frac{1}{2}} = W_N - W_{N-1} \tag{90}$$

But for the velocity, V_o, associated with the "assumed" far-field boundary, the equation is:

$$\left(A_{xN} - A_{xN-1}\right) \left\langle \rho_o V_o \right\rangle_{N-\frac{1}{2}} = W_N - W_{N-1} \tag{91}$$

Equation 91 is subtracted from Equation 90.

$$\left(A_N - A_{N-1}\right)\left\langle \rho V \right\rangle_{N-\frac{1}{2}} - \left(A_{xN} - A_{xN-1}\right) \left\langle \rho_o V_o \right\rangle_{N-\frac{1}{2}} = 0 \tag{92}$$

The identities:

$$A_N - A_{N-1} \equiv \left(A_{oN} - A_{oN-1}\right) + \delta A_N - \delta A_{N-1} \tag{93a}$$

$$A_{xN} - A_{xN-1} \equiv \left(A_{oN} - A_{oN-1}\right) + \left(A_x - A_o\right)_N - \left(A_x - A_o\right)_{N-1} \tag{93b}$$
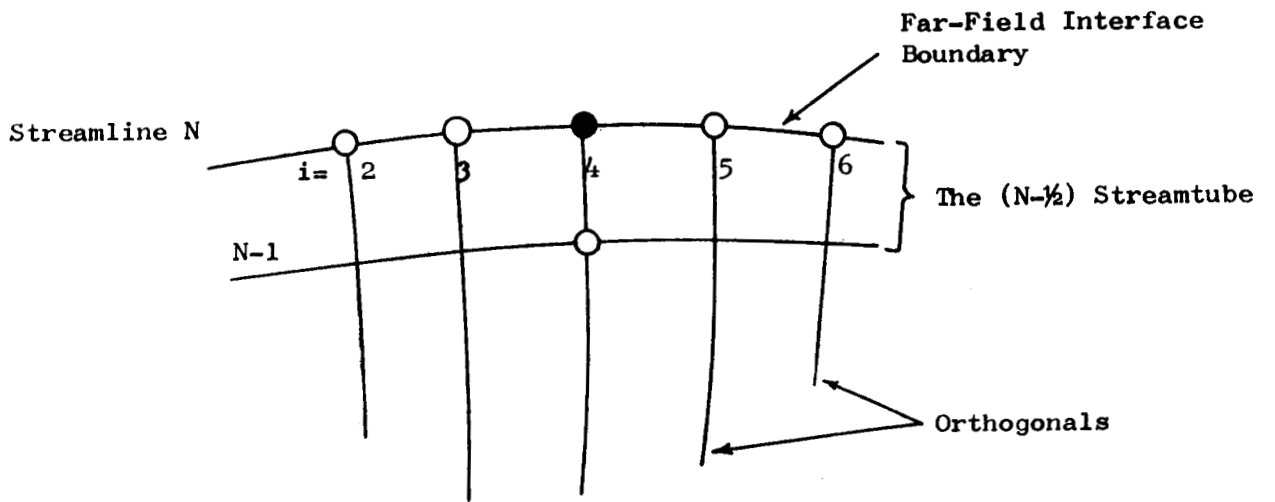
Figure 32. Notation for Section 5.6.4.

and:

$$\delta \langle \rho V \rangle_{N-\frac{1}{2}} \equiv \langle \rho V \rangle_{N-\frac{1}{2}} - \langle \rho_o V_o \rangle_{N-\frac{1}{2}} \tag{93c}$$

are introduced into Equation 92 and the result rearranged to give:

$$\left[\langle \rho_o V_o \rangle_{N-\frac{1}{2}} + \delta \langle \rho V \rangle_{N-\frac{1}{2}} \right] \left(\delta A_N - \delta A_{N-1} \right) + \left(A_{oN} - A_{oN-1} \right) \delta \langle \rho V \rangle_{N-\frac{1}{2}}$$

$$= \langle \rho_o V_o \rangle_{N-\frac{1}{2}} \left[\left(A_x - A_o \right)_N - \left(A_x - A_o \right)_{N-1} \right] \tag{94}$$

Equation 94 represents the continuity form of the correction equation for the outermost streamtube.

The velocity correction is approximated as follows. The average velocity, $V_{N-\frac{1}{2}}$, for the streamtube is related to the boundary velocity by the identity:

$$\delta V_{N-\frac{1}{2}} \equiv \delta V_N + \delta \left(V_{N-\frac{1}{2}} - V_N \right) \tag{95}$$

For a constant pressure boundary δV_N is zero; for the far-field interface streamline:

$$\delta V_N = \frac{V_{oN}}{\sqrt{1-M_{oN}^2}} \quad \sum_{i=2}^{5} \quad G_{FFi} \; \delta n_{i,N} \tag{96}$$

$$G_{FFi} = \frac{0.865}{\Delta S} \begin{pmatrix} 0 \\ -1 \\ 2 \\ -1 \\ 0 \end{pmatrix} \tag{97}$$

Equations 96 and 97 relate the change in velocity at point (i = 4) to the local ordinate changes of the streamline ($\delta n_{i,N}$). Included in this formulation is the contribution from the movement of the point itself and the two upstream and two downstream neighbors. The coefficient $(0.865/\Delta S)$ and the relative factors of $[0, -1, 2, -1, 0]$ were determined (as reasonable approximations) from numerical solutions. ΔS is the average local spacing between points along the interface streamline, and the coefficient $(1-M_o^2)^{-\frac{1}{2}}$ corrects for the compressibility or Mach number effect.

The second term on the right-hand side of Equation 95 is evaluated, as before, by the cross-stream momentum equation:

$$\frac{1}{V} \frac{\partial V}{\partial n} = -C$$

Approximately, for the constant streamtube:

$$\frac{V_N - V_{N-1}}{\frac{1}{2}\left(V_N + V_{N-1}\right)} = -\frac{1}{2}\left(n_N - n_{N-1}\right)\left(C_N + C_{N-1}\right) \tag{98}$$

Define $V_{N-\frac{1}{2}} = \frac{1}{2}(V_N + V_{N-1})$ and $C_{N-\frac{1}{2}} = \frac{1}{2}(C_N + C_{N-1})$, then Equation 98 can also be expressed as follows:

$$\left(V_{N-\frac{1}{2}} - V_N\right) = \frac{1}{2} V_{N-\frac{1}{2}}\left(n_N - n_{N-1}\right) C_{N-\frac{1}{2}} \tag{99}$$

The differential (or small variation form) of Equation 99 is:

$$\delta\left(V_{N-\frac{1}{2}} - V_N\right) = \frac{1}{2} V_{N-\frac{1}{2}}\left(n_N - n_{N-1}\right)\delta C_{N-\frac{1}{2}} + \frac{1}{2} C_{N-\frac{1}{2}}\ \delta\left[V_{N-\frac{1}{2}}\left(n_N - n_{N-1}\right)\right]$$

$$= \frac{1}{2} V_{N-\frac{1}{2}}\left(n_N - n_{N-1}\right)\delta C_{N-\frac{1}{2}} \tag{100}$$

$$+ \frac{1}{2} C_{N-\frac{1}{2}}\left\{\frac{1}{\rho_{N-\frac{1}{2}}}\ \delta\left[\rho_{N-\frac{1}{2}} V_{N-\frac{1}{2}}\left(n_N - n_{N-1}\right)\right] - \frac{V_{N-\frac{1}{2}}\left(n_N - n_{N-1}\right)}{\rho_{N-\frac{1}{2}}}\ \delta\rho_{N-\frac{1}{2}}\right\}$$

From the continuity equation, the first term in the braces is zero. (For the outer streamtube, the effect of a change in radius is neglectable.) The density variation in the second term can be related to the velocity variation:

$$\frac{\delta\rho_{N-\frac{1}{2}}}{\rho_{N-\frac{1}{2}}} = -M^2_{N-\frac{1}{2}}\ \frac{\delta V_{N-\frac{1}{2}}}{V_{N-\frac{1}{2}}} \tag{101}$$

Thus, Equation 100 can be written:

$$\delta\left(V_{N-\frac{1}{2}} - V_N\right) = \frac{1}{2} V_N\left(n_N - n_{N-1}\right)\delta C_{N-\frac{1}{2}} + \frac{1}{2}M^2_{N-\frac{1}{2}} C_{N-\frac{1}{2}}\left(n_N - n_{N-1}\right)\delta V_{N-\frac{1}{2}} \tag{102}$$

Equations 96 and 102 are substituted into Equation 95 to obtain:

$$Q_{N-\frac{1}{2}}\ \delta V_{N-\frac{1}{2}} = \frac{V_{oN}}{\beta_N}\ \sum_{i=2}^{5}\ G_{FFi}\ \delta n_{i,N} + \frac{1}{2} V_{N-\frac{1}{2}}\left(n_N - n_{N-1}\right)\delta C_{N-\frac{1}{2}} \tag{103}$$

where:

$$Q_{N-\frac{1}{2}} = 1 - \frac{1}{2}M^2_{N-\frac{1}{2}} C_{N-\frac{1}{2}}\left(n_N - n_{N-1}\right) \tag{104}$$

The product of curvature and streamtube thickness is expected to be very much less than unity, therefore $Q_{N-\frac{1}{2}}$ is approximately equal to unity. Also:

$$\delta \langle \rho V \rangle_{N-\frac{1}{2}} = \beta^2_{N-\frac{1}{2}} \, \rho_{N-\frac{1}{2}} \, \delta V_{N-\frac{1}{2}} \tag{105}$$

This together with Equation 103 substituted into Equation 94 gives the following for the interface streamline correction equation:

$$\left(\rho V\right)_{N-\frac{1}{2}} \left(\delta A_{N-1} - \delta A_N\right) - \left(A_{oN} - A_{oN-1}\right)\left(\frac{\beta 2 \rho}{Q}\right)_{N-\frac{1}{2}} \left[\frac{V_{oN}}{\beta_N} \sum_{i=2}^{5} G_{FF} \, \delta n_{i,N} \right.$$

$$\left. + \tfrac{1}{2} V_{N-\frac{1}{2}} \left(n_N - n_{N-1}\right) \delta C_{N-\frac{1}{2}}\right] = \left(\rho V\right)_{N-\frac{1}{2}} \left[\left(A_x - A_o\right)_{N-1} - \left(A_x - A_o\right)_N\right] \tag{106}$$

Equation 106 presumes:

$$\langle \rho_o V_o \rangle_{N-\frac{1}{2}} + \delta \langle \rho V \rangle_{N-\frac{1}{2}} \approx \langle \rho_o V_o \rangle_{N-\frac{1}{2}} \approx \langle \rho V \rangle_{N-\frac{1}{2}}$$

Also, to a reasonable approximation:

$$\beta_{N-\frac{1}{2}} \approx \beta_N$$

$$\rho_{N-\frac{1}{2}} \approx \rho_N$$

$$Q_{N-\frac{1}{2}} \approx Q_N$$

$$V_{oN} \approx V_{N-\frac{1}{2}}$$

Equation 106 is divided through by $(\rho V)_{N-\frac{1}{2}}$; and, with the above approximations, the far-field boundary correction equation becomes:

$$\delta A_{N-1} - \delta A_N - (A_{oN} - A_{oN-1}) \frac{\beta_N}{Q_N} \sum_{i=2}^{5} G_{FFi} \, \delta n_{i,N} - \frac{B_N}{Q_N} \delta C_{N-\frac{1}{2}}$$

$$= (A_x - A_o)_{N-1} - (A_x - A_o)_N \tag{107}$$

where:

$$B_N = \tfrac{1}{2}\left(A_{oN} - A_{oN-1}\right) \beta^2_N \left(n_N - n_{N-1}\right) \tag{108}$$

In the present STC code, we further approximate Q_N as unity.

The average streamline curvature is taken to be equal to the boundary curvature:

$$-\delta C_{N-\frac{1}{2}} = -\delta C_N = G_2 \delta n_{2,N} + G_3 \delta n_{3,N} + G_4 \delta n_{4,N} + G_5 \delta n_{5,N} + G_6 \delta n_{6,N} \quad (109)$$

where the G's are the influence coefficients relating streamline point movement to the negative of curvature. Also, it follows that:

$$\delta A_{N-1} - \delta A_N = 2\pi r_{N-1} \, \delta n_{N-1} - 2\pi r_N \delta_n \quad (110a)$$

for axisymmetric flow, and that:

$$\delta A_{N-1} - \delta A_N = \delta n_{N-1} - \delta n_N \quad (110b)$$

for two-dimensional flow.

With Equations 109 and 110, the left-hand side of Equation 107 involves only the streamline correction quantities, δn, and the right-hand side is the error term computed in the flow balance section. Equation 107 is used with Equations 86, 87 and 89 to obtain the matrix equation for δn_M for M = 1, 2 .... NM where NM is the total number of grid points in the field.

5.6.5 The Curvature Influence Coefficients

To complete the formulation of the system of correction equations, it is necessary to relate the change in curvature to the movement of the streamline. Specifically the values of G in Equation 85 (repeated below) are desired.

$$-\delta C_{4,k} = G_1 \delta n_{1,k} + G_2 \delta n_{2,k} \quad G_3 \delta n_{3,k} + G_4 \delta n_{4,k} + G_5 \delta n_{5,k}$$

$$+ G_6 \delta n_{6,k} = \Sigma G_i \delta n_{i,k}$$

An illustration of the notation is provided in Figure 33. To a very good approximation, the curvature variation is equal to the variation of the second streamwise derivative of δn.

$$-\delta C_{4,k} \approx \left(\frac{D^2 \delta n_k}{Ds^2} \right)_4 \qquad \text{(Repeat of Equation 86)}$$

To evaluate this second derivative, the linear spline equations are employed, maintaining compatibility with the beam curve fits of Section 5.2. The method for calculating the spline influence coefficients is presented in Appendix B. Since only small adjustments from the given curve are to be made, the arc length along the curve, s, and the normal point adjustment,

Corrected k^{th} Streamline

$\delta n_{1,k}$ $\delta n_{2,k}$ $\delta n_{3,k}$ $\delta n_{4,k}$ $\delta n_{5,k}$ $\delta n_{6,k}$

S

Assumed k^{th} Streamline

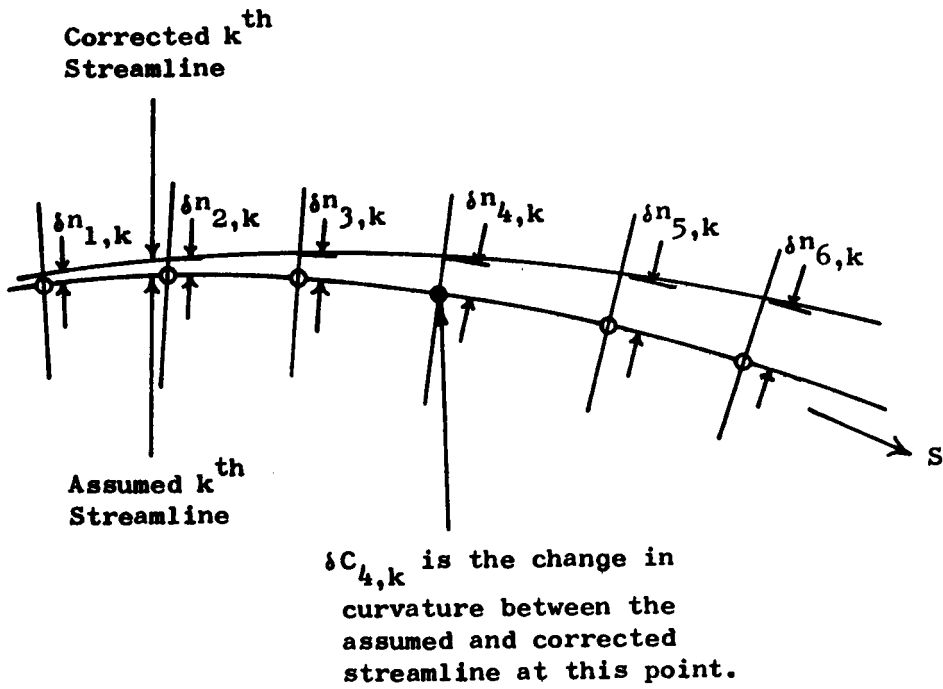$\delta C_{4,k}$ is the change in curvature between the assumed and corrected streamline at this point.

Figure 33. Notation for Section 5.6.5.

δn, are replaced by x and y in that development. The resulting values of the influence coefficients are tabulated in Table II for the specific case of a uniform spacing where $\Delta x = \Delta s = 1$.

As indicated in Table II, the influence coefficients for a point on a spline curve involve all of the other points on the spline. That is, the movement of any one point affects the curvature at all of the points, although the effect on the curvature at distant points is small. To include the entire set of spline influence coefficients is impractical, because it would lead to a completely dense, rather than sparce, coefficient matrix for the correction equation. Therefore, the curvature influence coefficients are always truncated to 5 points, or less near boundaries. The method of truncating is to simply replace the one long spline with a series of short splines. Each short spline passes through only the point in question and the two upstream and two downstream neighbors, if they exist. If the local velocity is supersonic, then three (or two) upstream points and no downstream points are included to duplicate, in effect, the supersonic curve fit of Section 5.2.3.

Artificial boundary conditions are enforced at the upstream and downstream ends of this truncated spline. For subsonic flow, the selected boundary condition is that $y'' = 0$ at each end (remember $y = \delta n$). However, if the truncated spline end point is also a streamline end point, then the boundary condition is chosen to agree with the curvature end condition discussed in Section 5.2.2. For supersonic points, the end options are again chosen to be equivalent to those used for the calculation of curvature.

It is interesting to notice how different the spline coefficients are from those of a polynominal. This is illustrated in Table II. Although the 3-point parabola formula is commonly used for subsonic flow, the spline formula is found to be considerably different and, we believe, more accurate.

5.7 MATRIX SOLUTION PROCEDURE

In the previous section, equations for the streamline position correction, δn, were developed for each grid point. At interior points and flow inlet/exit boundary points, Equation 86 is used together with Equations 84 and 85. And either Equation 89 or Equation 107 through 110 are used at the orthogonal line boundary points. This yields a system of simultaneous equations where at any "central" point the applicable equation can be written in the form:

$$A_1\delta_1 + A_2\delta_2 + A_3\delta_3 + \left[A_4^{(1)} + A_4^{(2)}\right]\delta_4 + A_5\delta_5 + A_6\delta_6 + A_7\delta_7 + A_8\delta_8 = \text{RHS}$$

$$(111)$$

The notation δ is used in place of δn for brevity and the subscripts refer to neighboring points as indicated in Figure 34. If the velocity at point 4 is subsonic, then point 1 is not included ($A_1 = 0$); if the velocity is supersonic then points 5 and 6 are both omitted ($A_5 = A_6 = 0$).

Table II. Influence Coefficients for Several Curvature Formulas.

Type of Curvature Formula	Point Number												
	$-\infty$	-1	0	1	2	3	4	5	6	7	8	9	$+\infty$
SUBSONIC													
Parabola/Cubic	---	---	---	---	---	1.0	-2.0	1.0	---	---	---	---	---
Quartic/Quinitic	---	---	---	---	-0.083	1.333	-2.5	1.333	-0.083	---	---	---	---
10th Order Polynomial	---	0.0003	-0.005	0.040	-0.283	1.667	-2.927	1.667	-0.238	0.040	-0.005	0.0003	---
Infinite Cubic Spline	≈ 0	0.0065	-0.046	0.196	-0.745	2.784	-4.392	2.784	-0.751	0.196	-0.046	0.0065	≈ 0
Truncated Cubic Spline	---	---	---	---	-0.429	2.571	-4.286	2.571	-0.429	---	---	---	---
SUPERSONIC													
Parabola	---	---	---	---	1.0	-2.0	1.0	---	---	---	---	---	---
Cubic	---	---	---	-1.0	4.0	-5.0	2.0	---	---	---	---	---	---

Note: Values given are the influence on the second derivative of a unit ordinate change at the given point. The numbering of the points is illustrated in Figure 34. Point 4 is the central point. Spacing between points is unity.
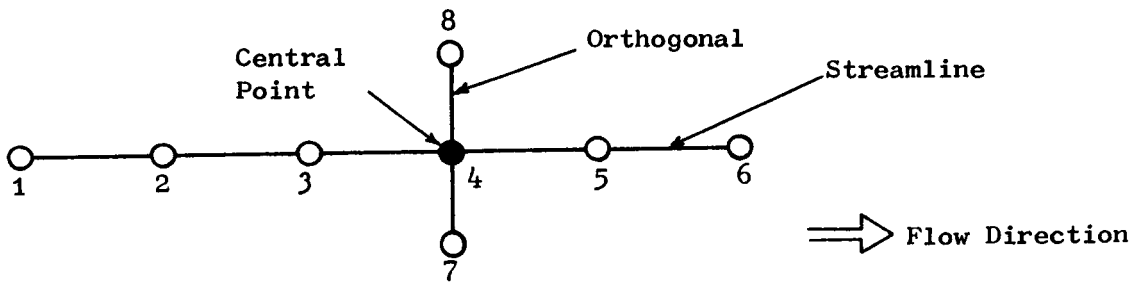
Figure 34. Arrangement of Neighboring Points for the General Subsonic/Supersonic Star.

It should be noted that points 1 to 6, as shown in Figure 34, never include any of the special points which terminate a partial orthogonal. These points are skipped by extending the star, as required, to the next point in either the downstream or upstream direction.

In all cases, A_1, A_2, A_3, $A_4^{(1)}$, A_5, and A_6 are the curvature influence coefficients times the coefficient B_1. For example:

$$A_1 = B_1 \, G_1$$

$$A_2 = B_1 \, G_2$$

$$A_4^{(1)} = B_1 \, G_4$$

etc.

The values of A_7, A_8, and $A_4^{(2)}$, for interior points, are related to the flow difference between streamlines. These coefficients, given by Equation 84 for axisymmetric geometry, are:

$$A_7 = \frac{2\pi \, r_{k-1}}{W_k - W_{k-1}} \quad , \qquad A_8 = \frac{2\pi \, r_{k+1}}{W_{k+1} - W_k} \quad ,$$

$$A_4^{(2)} = -2\pi \, r_k \left[\frac{1}{W_{k+1} - W_k} + \frac{1}{W_k - W_{k-1}} \right]$$

(112)

For a two-dimensional configuration, the $(2\pi \, r)$ factors are replaced by unity. Double streamlines (which separate two adjacent channels) are disconnected; the finite difference equation of the form of Equation 111 is only written for the second of the two coincident lines. For the first line, the following equation is employed:

$$\delta_{4b} - \delta_{4a} = (n_x - n_o)_{4b} - (n_x - n_o)_{4a}$$

The "4b" and "4a" subscripts indicate the points which belong to the lower and upper channel, respectively. For noninterior points, the values of A_1 to A_8 are similarly defined according to the equations of the previous section.

The set of equations defined by Equation 111 are solved by a "block" relaxation method. In this procedure, an initial guess for the values of δ is successively relaxed until the solution does not change; viz, the solution is constant within a specified tolerance. The options available for sweeping the field are:

a) Solving orthogonal line blocks, sweeping upstream to downstream

b) Solving streamline blocks, sweeping from the centerline to the outer radius (or from small y to large y)

c) Alternate use of a) and b)

Included in the relaxation procedure is an acceleration factor, ρ, which serves the same purpose as the overrelaxation factor in the point-relaxation method. For the two types of block relaxation, Equation 111 is rewritten as follows:

Orthogonal Blocks:

$$A_7\delta_7 + \left[A_4^{(2)} + \rho A_4^{(1)} \right]\delta_4 + A_8\delta_8 = \text{RHS} - \left[A_1\,\delta_1 + A_2\delta_2 + A_3\delta_3 + \right.$$

$$\left. (1-\rho)\,A_4^{(1)}\,\delta_4 + A_5\delta_5 + A_6\delta_6 \right] \tag{113a}$$

Streamline Blocks:

$$A_1\delta_1 + A_2\delta_2 + A_3\delta_3 + \left[A_4^{(1)} + \rho A_4^{(2)} \right]\delta_4 + A_5\delta_5 + A_6\delta_6 = \text{RHS}$$

$$-\left[A_7\delta_7 + (1-\rho)\,A_4^{(2)}\,\delta_4 + A_8\delta_8 \right] \tag{113b}$$

The terms involving the streamline adjustments on the modified right-hand side of each equation are evaluated using the results of the previous iterate. Orthogonal line blocks require the solution of a tridiagonal matrix, while streamline blocks require the solution of a pentadiagonal matrix. In both instances, the solution is obtained by a left-right decomposition of the coefficient matrix followed by back-substitution The solution is assumed to be converged when the maximum change from one iteration to the next is within a specified tolerance. Specifically it is required that:

$$\text{Max}|\Delta\delta| \leq \text{TOLRL} * \text{Max}|\delta|$$

where $\Delta\delta$ is the change in δ between two successive sweeps at a given point.

The acceleration factor, ρ, may be either taken as constant or allowed to vary with the sweep number. Using the results of Peaceman and Rachford (ref. 14), the acceleration factor is determined as a function of the sweep number and the total number of points in the field. The latter parameter is tentative, since the STC program uses a nonuniform grid, and the Peaceman-Rachford relation was developed for a uniform grid.

$$\rho = \rho_B + 2\rho_A \sin^2 \frac{n\pi}{2\sqrt{NM}} \qquad (114)$$

where:

n $\quad$ = sweep number

ρ_B $\quad$ = base acceleration factor

ρ_A $\quad$ = half of the amplitude of the sinusoidal variation

NM $\quad$ = number of grid points in the field

The standard mode of operation is to alternate between the orthogonal and streamline block sweeping. When the sweep number reaches the stage where $n = 2\sqrt{NM}/\pi$ then n, as used in Equation 114, is reset to 1. The resulting variation in convergence factor is depicted in Figure 35.

As in the case of successive point overrelaxation (SOR), an optimum value of ρ corresponding to the minimum problem convergence time, may be determined. Selection of the optimum acceleration factors is discussed below.

An internal flow test case with $M_o = 0.09$ was chosen to optimize the acceleration factor for the alternating direction solution procedure. The matrix solution time vs. ρ_B was established by systematically reducing ρ_B from unity to a minimum value of 0.45. The results are depicted in Figure 36.

As indicated, the optimum ρ_B setting occurs somewhere in the vicinity of 0.5 to 0.6. With $\rho_B = 0.4$, the block relaxation diverged. For $\rho_B = 0.5$, the matrix solution time was 42.4 percent of the total iteration cycle time which includes one pass through Steps 3 through 12 of Section 3.0.

Based on this test and other results similar to this, ρ_B and ρ_A have both been initialized to 0.5 in the computer code. Alternate values may be input by the user.

5.8 STREAMLINE ADJUSTMENT

To adjust the streamline position, the coordinates are moved in the normal direction by the computed δn's.

$$z^{p+1} = z^p - C_v \, \delta n \sin \phi_1$$

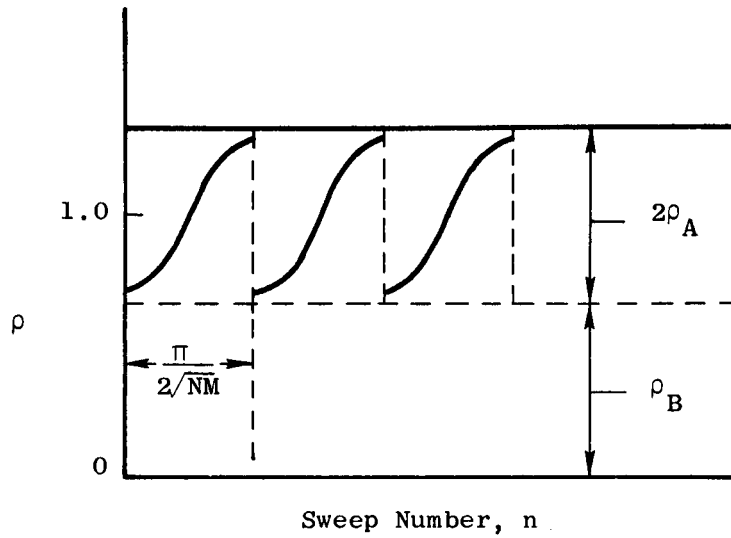$$r^{p+1} = r^p + C_v \, \delta n \cos \phi_1$$

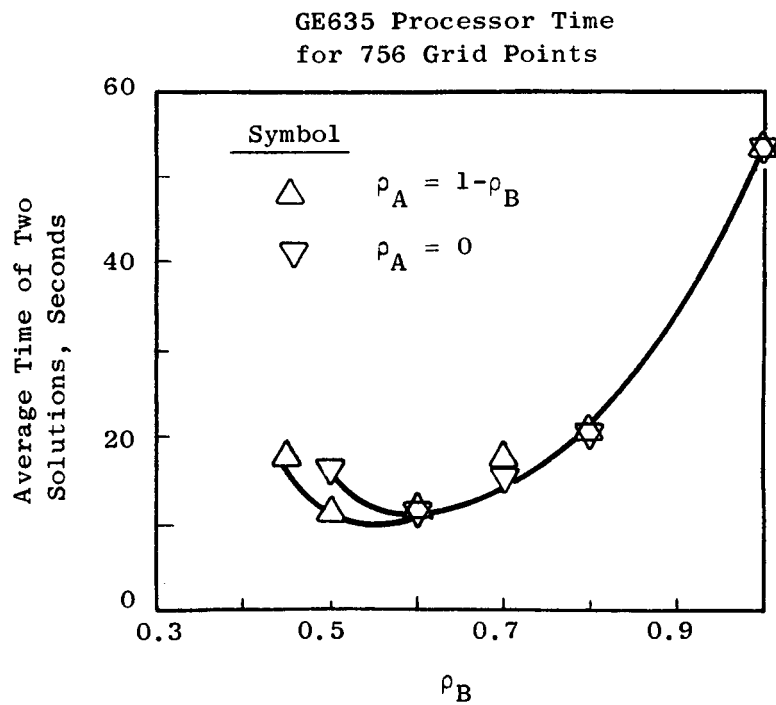Figure 35.   Typical Variation of the
Acceleration Factor.

Figure 36.   Matrix Relaxation Time as a Function
of the Base Acceleration Factor.

The streamline angles, ϕ_1, are those found from the curve fits of Section 5.2. The superscript p is the iteration sequence number, and C_v is a convergence factor which is generally equal to unity.

The new values of z and r then form the basis for the next iteration, or for the solution which is printed out. The next step in the procedure is to again compute the curvatures and from these compute the velocities and flow balance errors.

5.9 BOW SHOCK WAVE

The original intent of the analysis development was to include the approximate bow wave method of Moeckel (Reference 15.) With the inclusion of the bow wave, it would have been possible to analyze nacelles at transonic Mach numbers above 1.0. During the development of STC with the bow wave, serious difficulties were found and a reliable computer solution was not practical. Accordingly, two versions of the STC computer program were furnished; 1) a standard, fully functional STC computer analysis without the Moeckel bow wave and 2) a status level program incorporating the bow wave which was provided for the purpose of future investigation.

Technically, the approximate nature of the Moeckel method compromises the quality of the STC solution. The assumed hyperbolic shock shape and the empirically specified stand-off distance force continuity to be violated between the shock and the body. In addition, once the Moeckel bow shock is added to the flow field (after three initial flow field refinements to stabilize the streamlines and orthogonals), further refinement of the flow field in the vicinity of the shock is stopped. At the same time, streamline curvature near the shock is preset to zero. The good features of STC are not part of the bow wave solution. Hence, the STC results are not enhanced by including the approximate bow wave solution.

The STC solution with the bow shock has been programmed as a separate computer program since extensive changes were necessary. The difficulties that developed during checkout preclude a useful solution, but Volume II of the User's Manual (Reference 16) shows how to use this version of STC.

For Mach numbers up to 1.2, it is recommended that the standard version of STC be run in the supersonic mode with grid refinement suppressed near the shock. At Mach 1.2, the nominal streamline deflection through the shock is 4° with a maximum total pressure loss coefficient of 0.007. These conditions can be approximated using the standard STC program.

5.10 INTEGRAL MOMENTUM CHECKS AND PRESSURE DRAG EVALUATION

The STC Program evaluates the thrust/drag on each boundary surface and then verifies these forces by performing "overall" momentum balance checks for each of the fluid streams. For a typical nacelle configuration, a momentum balance is computed for the inlet stream, the external stream, and

the jet exhaust stream. For the inlet stream, as an example, the entering momentum (or ram drag) calculated using fluid properties at the most upstream station is first determined. Second, the pressure times the projected area of the cowl stagnation streamline is computed. This is added to the axial pressure force on the underside of the inlet lip from the stagnation point to the last calculation station (near the fan face). Third, a similar pressure-area integration to include the axial forces on the spinner is performed. Finally, the sum of the entering momentum and the integrated upper and lower boundary forces (including the additive drag of the cowl approach streamline) is compared to the integrated axial momentum flux at the last station inside the inlet. A discrepancy will indicate inaccuracies in the computed pressure distributions or, perhaps, insufficient refinement of the calculation grid for adequate resolution. It has been found that these momentum checks are quite valuable for quickly assessing the computed result.

6.0 CONCLUSIONS

The Streamtube Curvature Analysis has been developed and a computer solution has been utilized to solve the transonic flow field over an isolated nacelle. The analysis includes the capabilities to:

- Analyze the stagnation region of an inlet with grid refinement as needed so that the stagnation streamline is properly predicted.

- Handle multiple streams of differing stagnation properties with a static pressure balance at the interface.

- Predict the location and strength of imbedded shock waves on the external nacelle surface.

- Define an analytical far-field boundary so that free-flight conditions are predicted.

- Achieve greater solution economy for the transonic flight speed regime in that the computational times are 5 to 10 times faster than state-of-the-art time-dependent methods for the same number of grid points.

- Provide a user-oriented design analysis tool for responsive solutions to engineering problems.

The inviscid pressure distributions predicted by the Streamtube Curvature Analysis compare very well with test results when viscous interactions are minimal. When shocks are predicted, the viscous interactions and boundary layer separation regions prevent good correlations with test data.

The computer analysis fills a void in that several techniques are available for solving the inviscid equations of motion about arbitrary two- or three-dimensional bodies at transonic speeds, but none have handled the complete nacelle with inlet flow and exhaust flow. The Streamtube Curvature Analysis provides the capability to predict the transonic flow field about typical aircraft engine installations in isolated nacelles at transonic speeds. The solution technique provides a design analysis tool which will provide guidance for wind tunnel testing to develop nacelle shapes to minimize drag within given design restraints.

The details of the computer program operation, usage, and structure are documented in the Users Manual (Reference 16).

7.0 APPENDIX A

SECOND-ORDER STREAMLINE CURVATURE EQUATIONS FOR ISENTROPIC PLANAR FLOW

In this section the second-order equation which describes the shape of the streamline is derived. An orthogonal system is chosen. The variable n is a measure of the distance across the streamlines and s is the distance along a streamline. The partial differential operator ∂ indicates that the direction of differentiation is normal to the streamline. The operator D indicates that the direction of differentiation is along a streamline. The basic equations are:

Continuity: $\qquad\qquad\qquad \rho V\, \partial n = \partial \Psi \qquad\qquad\qquad (115)$

Crocco Form of Normal
Momentum Equation for $\qquad \dfrac{\partial V}{\partial n} = -CV \qquad\qquad\qquad (116)$
Irrotational Flow:

where:

$\quad V \;=\;$ velocity

$\quad \rho \;=\;$ density

$\quad C \;=\;$ streamline curvature $= -\dfrac{\partial \phi}{\partial s}$

$\quad s \;=\;$ streamwise coordinate

$\quad n \;=\;$ cross-stream coordinate

$\quad \phi \;=\;$ streamline angle measured from horizontal

Equation 115 is differentiated as follows:

$$\frac{\partial n}{\partial \Psi} = \frac{1}{\rho V} \qquad\qquad\qquad (117)$$

$$\frac{\partial^2 n}{\partial \Psi 2} = -\frac{1}{\rho V}\left(\frac{1}{V} + \frac{1}{\rho}\frac{\partial \rho}{\partial V}\right)\frac{\partial V}{\partial n}\frac{\partial n}{\partial \Psi} \qquad\qquad (118)$$

Equation 117 is substituted into Equation 118 and the result rearranged:

$$\frac{\partial^2 n}{\partial \Psi^2} + \frac{1}{(\rho V)^2} \left(1 + \frac{V}{\rho} \frac{\partial \rho}{\partial V}\right) \frac{1}{V} \frac{\partial V}{\partial n} = 0 \tag{119}$$

Now Equation 116 is substituted into Equation 119:

$$\frac{\partial^2 n}{\partial \Psi^2} - \frac{1}{(\rho V)^2} \left(1 + \frac{V}{\rho} \frac{\partial \rho}{\partial V}\right) C = 0 \tag{120}$$

Equation 120 is the desired second-order equation for n, where the curvature is analogous to a derivative of the form $(D^2 n / Ds^2)$. Since the flow is isentropic, the coefficient in parenthesis may be expressed as follows:

$$1 + \frac{V}{\rho} \left(\frac{\partial \rho}{\partial V}\right)_s = 1 - M^2 \tag{121}$$

thus, the equation reduces to:

$$\frac{\partial^2 n}{\partial \Psi^2} - \frac{1 - M^2}{(\rho V)^2} C = 0 \tag{122}$$

Clearly, the elliptic and hyperbolic nature of the equation is evident when the Mach number is less than and greater than unity.

Equation 120 is now written in the following abbreviated form:

$$\frac{\partial^2 n}{\partial \Psi^2} - B C = 0 \tag{123}$$

where:

$$B = \frac{1}{(\rho V)^2} \left(1 + \frac{V}{\rho} \frac{\partial \rho}{\partial V}\right)$$

The equation in its present form cannot be applied directly to obtain a solution for n because of the difficulty of relating the radius of curvature to the second streamwise derivative of n. Instead, it is used to calculate the streamline adjustments (in the cross-stream direction) for an assumed streamline pattern.

To illustrate, we consider an assumed set of streamlines which pass through the small circles in the adjoining sketch.
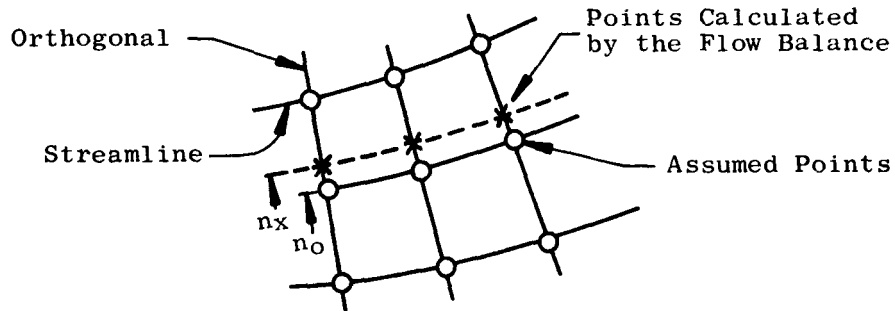
By a curve-fitting process, the values of streamline angle and curvature, C_o, are determined. (The circle points are also orthogonalized. That is, they are moved along the streamlines so that the "orthogonal lines" are truly normal to the given streamlines.) Equations 115 and 116 are integrated along the orthogonal lines, assuming the value of C_o is valid, and from this "flow balance" the x-positions of the streamline are determined. We have then the following equation satisfied:

$$\frac{\partial^2 n_x}{\partial \Psi^2} - B\, C_o = 0 \qquad (124)$$

The "o" subscript denotes values related to the assumed streamline positions and curvatures. The "x" subscript refers to the streamline position as calculated by the continuity equation. The true solution to Equation 123 is sought; "true solution values" are unsubscripted.

Equation 124 is subtracted from Equation 123. The result is:

$$\left(\frac{\partial^2 n}{\partial \Psi^2} - \frac{\partial^2 n_x}{\partial \Psi^2} \right) + B \left(- C + C_o \right) = 0$$

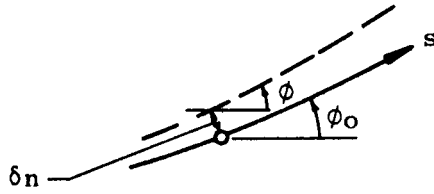The adjustment to be made in streamline position is $\delta n = n-n_o$. Hence, the above can be written:

$$\frac{\partial^2 (\delta n)}{\partial \Psi^2} + B \left(- C + C_o \right) = \frac{\partial^2 (n_x - n_o)}{\partial \Psi^2} \qquad (125)$$

Finally, we note that:

$$- C_o + C_o = \frac{D\phi}{D_s} - \frac{D\phi_o}{D_s} \tag{126}$$

$$\approx \frac{D(\phi - \phi_o)}{Ds}$$

$$\approx \frac{D}{Ds}\left[\frac{D}{Ds}(\delta n)\right] = \frac{D^2(\delta n)}{Ds^2}$$

So the differential equation becomes:

$$\frac{\partial^2(\delta n)}{\partial \psi^2} + B\ \frac{D^2(\delta n)}{Ds^2} = \frac{\partial^2}{\partial \psi^2}\ (n_x - n_o) \tag{127}$$

8.0 APPENDIX B

SECOND DERIVATIVE INFLUENCE COEFFICIENTS FOR A SPLINE

For the interval between points i and i+1, a cubic equation may be written in the form:

$$y = y_i + b_i(x - x_i) + 1/2 \, c_i(x - x_i)^2 + 1/6 \, d_i(x - x_i)^3 \qquad (128)$$

Alternately, this same cubic may be expressed in terms of the ordinates (y_i and y_{i+1}) and the second derivatives (c_i and c_{i+1}) at the points x_i and x_{i+1}, namely:

$$y = \frac{1}{6\Delta x_i}\left[c_i(x_{i+1}-x)^3 + c_{i+1}(x-x_i)^3\right] \qquad (129)$$

$$+\left(\frac{y_i}{\Delta x_i} - \frac{c_i\Delta x_i}{6}\right)(x_{i+1} - x) + \left(\frac{y_{i+1}}{\Delta x_i} - \frac{c_{i+1}\Delta x_i}{6}\right)(x-x_i)$$

where $\Delta x_i = x_{i+1} - x_i$. By requiring a match in the first derivative at the interval boundaries, Equation 129 may be used to derive a set of N-2 equations for the c's:

$$\Delta x_{i-1} \, c_{i-1} + 2(\Delta x_{i-1} + \Delta x_i)c_i + \Delta x_i \, c_{i+1}$$

$$= \frac{6}{\Delta x_{i-1}} \, y_{i-1} - \left(\frac{6}{\Delta x_{i-1}} + \frac{6}{\Delta x_i}\right)y_i + \frac{6}{\Delta x_i} \, y_{i+1} \qquad (130)$$

Two additional end conditions then yield a total of N equations. A variety of end conditions is possible. The following are available as standard options:

(1) The first derivatives y_1' and/or y_N' are zero:

$$2\Delta x_1 c_1 + \Delta x_1 c_2 = - \frac{6}{\Delta x_1} \, y_1 + \frac{6}{\Delta x_1} \, y_2 \qquad (131)$$

$$\Delta x_{N-1}c_{N-1} + 2\Delta x_{N-1}c_N = \frac{6}{\Delta x_{N-1}} \, y_{N-1} - \frac{6}{\Delta x_{N-1}} \, y_N \qquad (132)$$

(2) The second derivatives y_1'' and/or y_N'' are zero:

$$c_1 = 0 \tag{133}$$

$$c_N = 0 \tag{134}$$

(3) The third derivative of the end polynominal is a specified fraction, F, of the third derivative of the polynominal second from the end:

$$-\frac{1}{\Delta x_1}\, c_1 + \left(\frac{1}{\Delta x_1} + \frac{F}{\Delta x_2}\right) c_2 - \frac{F}{\Delta x_2}\, c_3 = 0 \tag{135}$$

$$\frac{F}{\Delta x_{N-2}}\, c_{N-2} + \left(\frac{F}{\Delta x_{N-2}} + \frac{1}{\Delta x_{N-1}}\right) c_{N-1} - \frac{1}{\Delta x_{N-1}}\, c_N = 0 \tag{136}$$

(4) Same as Option 3 except that y_N is not chosen arbitrarily. Instead it is required that $y_{N'} = -\alpha y_N$. (Note this option is coded only for the downstream end of the spline.)

$$\left[\Delta x_{N-2} + \frac{F\left(\Delta x_{N-1}\right)^2 \left(3 + \alpha\Delta x_{N-1}\right)}{\Delta x_{N-2} \left(1 + \alpha\Delta x_{N-1}\right)}\right] c_{N-2}$$

$$+ \left[2\Delta x_{N-2} + \frac{F\left(\Delta x_{N-1}\right)^2 \left(3 + \alpha\Delta x_{N-1}\right)}{\Delta x_{N-2} \left(1 + \alpha\Delta x_{N-1}\right)} + \frac{3\Delta x_{N-1}\left(2 + \alpha\Delta x_{N-1}\right)}{\left(1 + \alpha\Delta x_{N-1}\right)}\right] c_{N-1}$$

$$= \frac{6}{\Delta x_{N-2}}\, y_{N-2} - 6\left[\frac{1}{\Delta x_{N-2}} + \frac{\alpha}{1 + \alpha\Delta x_{N-1}}\right] y_{N-1} \tag{137}$$

Equations 130 through 136 can be written in matrix form:

$$A_{j,i}\, c_i = B_{j,i}\, y_i \tag{138}$$

where A and B are square coefficient matrices, and c and y are column vectors of length N. If Option (4) is used, then Equation 137 replaces Equation 130 for $i = N-1$, and the size of the arrays are reduced by one. Generally, splines are fitted to given sets of data and Y is known. Here, we find the influence coefficients G by premultiplying Equation 138 by the inverse of A.

$$c_j = G_{j,i} \; y_i \tag{139}$$

where:

$$G = A^{-1}B \tag{140}$$

G is the array of coefficients which give the influence of y_i $i = 1$, $2\ldots N$ on the second derivative c_j.

We comment that G, as used in this section, is a square matrix. The desired set of influence coefficients for the second derivative at point j is the jth row of the matrix. In section 5.6.5, the notation G_j is used to indicate a vector which is the jth row of the matrix $G_{j,i}$ of this section.

9.0 APPENDIX C

NOMENCLATURE

Symbols

A	flow area measure normal to the streamline $= \int 2\pi r dn$
A	coefficient matrix
A_o/A_{HL}	mass flow ratio
a	unperturbed interface streamline radius
B, B_1, B_2, B_{3j}	coefficients in the streamline correction equation
b	first derivative
C	curvature, $= - d\phi_1/ds$
c	second derivative
C_D	inlet drag coefficient
C_P	pressure coefficient
c_p	specific heat at constant pressure
C_{DP}	integrated pressure drag coefficient
$D_{HL}/D_{Max.}$	diameter ratio
F	streamline curvature curve-fitting parameter, see Section 5.2.2
f	fractional position in the interval
g	1-f
G	curvature influence coefficients
H	enthalpy
M	Mach number
M_o	free-stream Mach number
n	distant measure along an orthogonal

n	matrix relaxation sweep number
P	pressure
Q	parameter defined by Equation 104
q	dynamic pressure
R_g	perfect gas constant
r	radius
S	entropy
s	distance measured along a streamline
T	temperature
u	axial component of velocity
v	vertical component of velocity
V	total component of velocity
W	cumulative flow rate
$X/D_{Max.}$	normalized inlet length
x,y	rectangular coordinate axis
z	axial position
α	angle of the chord between two adjacent points on the curve
α_j	parameter relating velocity corrections on the two sides of the jth slip line
β	compressible similarity parameter, $(1-M^2)^{1/2}$
γ	ratio of specific heats
ζ	dummy z-variable
η	dummy y-variable
ξ	dummy x-variable
ξ, ξ_1	coordinate system in the streamline direction

ξ_2	coordinate system in the direction normal to streamline
ρ	fluid density
ρ	matrix relaxation acceleration factor (Section 5.7)
σ	source density
ϕ_1, ϕ	streamline angle
ϕ_2	orthogonal line angle
Φ	velocity potential
Ψ	stream function
ω	vorticity

Subscripts

a	first end of the interval
a	evaluated above a slip line
b	second end of the interval
b	evaluated below a slip line
FF	far-field interface streamline
i	orthogonal line index (Section 5.5 & 5.6)
k,j	streamline index
M	field point index
o	initial or assumed values
∞	free stream
s	static
s	unperturbed interface streamline position
T	total
x	calculated by using the assumed streamline curvatures
1	streamline direction
2	orthogonal line direction

99

Superscripts

(1)   Denotes streamwise connection

(2)   Denotes crosswise connection

'   1st derivative

''   2nd derivative

'''   3rd derivative

p   iteration sequence number

10.0 ADDENDUM - PART II, TURBULENT BOUNDARY LAYER AND TURBULENT SEPARATION PREDICTION METHODS, By D.J. Lahti and P.H. Heck, General Electric, Aircraft Engine Group, Cincinnati, Ohio 45215

10.1 INTRODUCTION

The current state of the art of computing the development of turbulent boundary layers on arbitrary axisymmetric and/or planar bodies does not allow for the complete solution of the governing equations without some assumptions being made. These assumptions define the relationship of the fluctuating quantities to the mean flow quantities in determining the turbulent transport properties. As a result, many computational methods have evolved over the past few years, each method depending on the closure assumptions and, to some extent, the limited data available to support those assumptions. Without enough valid data to positively substantiate or disprove these closure assumptions it becomes difficult, if not impossible, to assess their true merits.

Although there is general wide-scale agreement that the finite difference methods do possess several advantages in computing turbulent boundary layers, they also possess some disadvantages. The primary disadvantages from the practical or engineering point of view is their relatively long computational times and the attendant higher costs.

There is general agreement within the General Electric Aircraft Engine Group that not all problems require the detailed solutions provided by the finite difference boundary layer methods. A large majority of the design decisions made can be accurately and confidently supported by the less expensive, yet accurate, integral boundary layer solutions. As a direct result of their rapid computational times and demonstrated accuracy, they are very attractive for coupling with inviscid flow analysis programs. This coupled inviscid/viscous computer program provides a very valuable and efficient engineering tool. The integral boundary layer method selected for coupling with the Streamtube Curvature Program incorporates the method of Stratford and Beavers (Reference 17) and is discussed in the following section.

10.2 TECHNICAL DISCUSSION

10.2.1 Turbulent Boundary Layer Method

Reference 18 examines several well-known integral methods for calculating the boundary layer characteristics and correlates the results as functions of free-stream Mach number and Reynolds number based upon an equivalent flat plate length (see References 18 through 25). This examination finds that all the methods concur in the conclusion that the momentum thickness may be expressed in the form:

$$\theta = f(M) \, X \, R_X^{-b} \tag{141}$$

where:

$$X = \frac{1}{P} \int_0^x P \, dx \tag{142}$$

For the flow on a flat plate, the Mach number, and thus the function P, would be constant so that $X = x$ and $\theta = f(M) \, x \, R_x^{-b}$. In effect, then, all the methods agree in saying that the momentum thickness in a flow with pressure gradient may be obtained from the expression for a flat plate, provided that actual distance x is replaced by an equivalent distance X, according to Equation 142. Consequently, the methods can only differ from one another in the expression for the flow on a flat plate and in the value of the function P. The only part of the result which can differ due to differences in each of the analytical treatments is, therefore, the function P.

Five of the methods employ transformations, each being some form of Stewartson's transformation from compressible to incompressible flow. Therefore, differences in P are due to differences carried over from incompressible solutions. Stratford and Beavers then conclude that rather than trying to assign any priority due to the merit of the incompressible solutions, they rather choose to represent P by a reasonable average of all the solutions. This is the concept employed by Thwaites (Reference 26) for incompressible laminar flow, and it proves to be the most expedient method under the circumstances.

In summary, the calculation procedure is as follows.

The boundary layer momentum thickness is expressible in the form:

$$\theta = f(M) \, X \, R_X^{-b} \tag{143}$$

where X is the equivalent flat plate length. It is defined as the length over which a boundary layer growing on a flat plate at the given Mach number would acquire the same thickness as the real boundary layer at that given location.

Stratford and Beavers propose the following equations as the provisional working formulas from which the following integral parameters may be calculated.

For $\quad\underline{1 \times 10^6 \le R_X \le 1 \times 10^7}$

$$\theta = 0.036 \ (1 + M^2/10)^{-0.7} \ XR_X^{-1/5} \tag{144a}$$

$$\delta = 0.37 \ XR_X^{-1/5} \tag{144b}$$

$$\delta^* = 0.046 \ (1 + 0.8 \ M^2)^{0.44} \ XR_X^{-1/5} \tag{144c}$$

For $\quad\underline{1 \times 10^7 \le R_X \le 1 \times 10^8}$

$$\theta = 0.022 \ (1 + M^2/10)^{-0.7} \ XR_X^{-1/6} \tag{144d}$$

$$\delta = 0.23 \ XR_X^{-1/6} \tag{144e}$$

$$\delta^* = 0.028 \ (1 + 0.8 \ M^2)^{0.44} \ XR_X^{-1/6} \tag{144f}$$

$$\text{where } X = \frac{1}{P} \int_0^x P \ dx \qquad \text{for planar flow} \tag{145a}$$

$$\text{and} \quad X = \frac{1}{Pr^a} \int_0^x Pr^a \ dx \quad \text{for axisymmetric flow} \tag{145b}$$

$$P = [M/(1 + M^2/5)]^4 \tag{146}$$

$$\text{and } a = \begin{cases} 1.25 \text{ for } R_X \approx 10^6 \\ 1.20 \text{ for } R_X \approx 10^7 \end{cases} \tag{147}$$

Having these expressions, the distributions of $\theta(x)$ and $\delta^*(x)$ can be calculated, given the boundary layer edge pressure distribution. Once the distributions of $\theta(x)$ and $\delta^*(x)$ are known, the integral momentum equation can be solved numerically to determine the local skin friction coefficient.

That is:

$$C_f = 2\frac{d\theta}{dx} + \frac{2}{U}\frac{dU}{dx}(2\theta + \delta^*) + \epsilon\frac{2}{r}\frac{dr}{dx} + \frac{2\theta}{\rho}\frac{d\rho}{dx} \qquad (148)$$

where, $\qquad \epsilon = \begin{cases} 0 & \text{for planar flow} \\ 1 & \text{for axisymmetric} \end{cases} \qquad (149)$

Equations 144 through 149 are those employed in the boundary layer solution.

10.2.2 Example Cases - Boundary Layer

The simplicity of the above method is quite obvious; and, as discussed in the Introduction section, it provides accurate and reliable estimates of the boundary layer effects so long as the assumptions of an adiabatic wall and turbulent flow throughout are not violated. In particular, it is ideal for calculating the integral displacement thickness distribution along a surface when an inviscid/viscous iterative calculation is being performed.

Several sample cases which demonstrate the ability of this integral method to predict turbulent boundary layers are discussed in this section. In the examples which follow, the predictions of the Stratford and Beavers method are designated S-B. In order to provide some comparison of relative accuracy of this method with a finite difference solution, some of the examples were also analyzed using the General Electric Aero Boundary Layer Program. This program, designed B.L., is very similar to the program developed at NASA-Langley by Beckwith and Bushnell (Reference 27). The results of the B.L. solutions on the various example cases are shown to provide a reference from which the quality of the S-B solutions can be judged.

10.2.2.1 Incompressible Flat Plate

The incompressible flat plate data of Wiegart (Reference 28) is shown in Figure 37 along with the S-B and B.L. predictions. The agreement is good over the full range of momentum thickness Reynold's numbers. Reference 28 suggests that the first data point is at about the minimum Reynolds number for turbulent flow.

This is further verified by the B.L. solution which shows this to be at about the same location as the downstream end of the transition region.
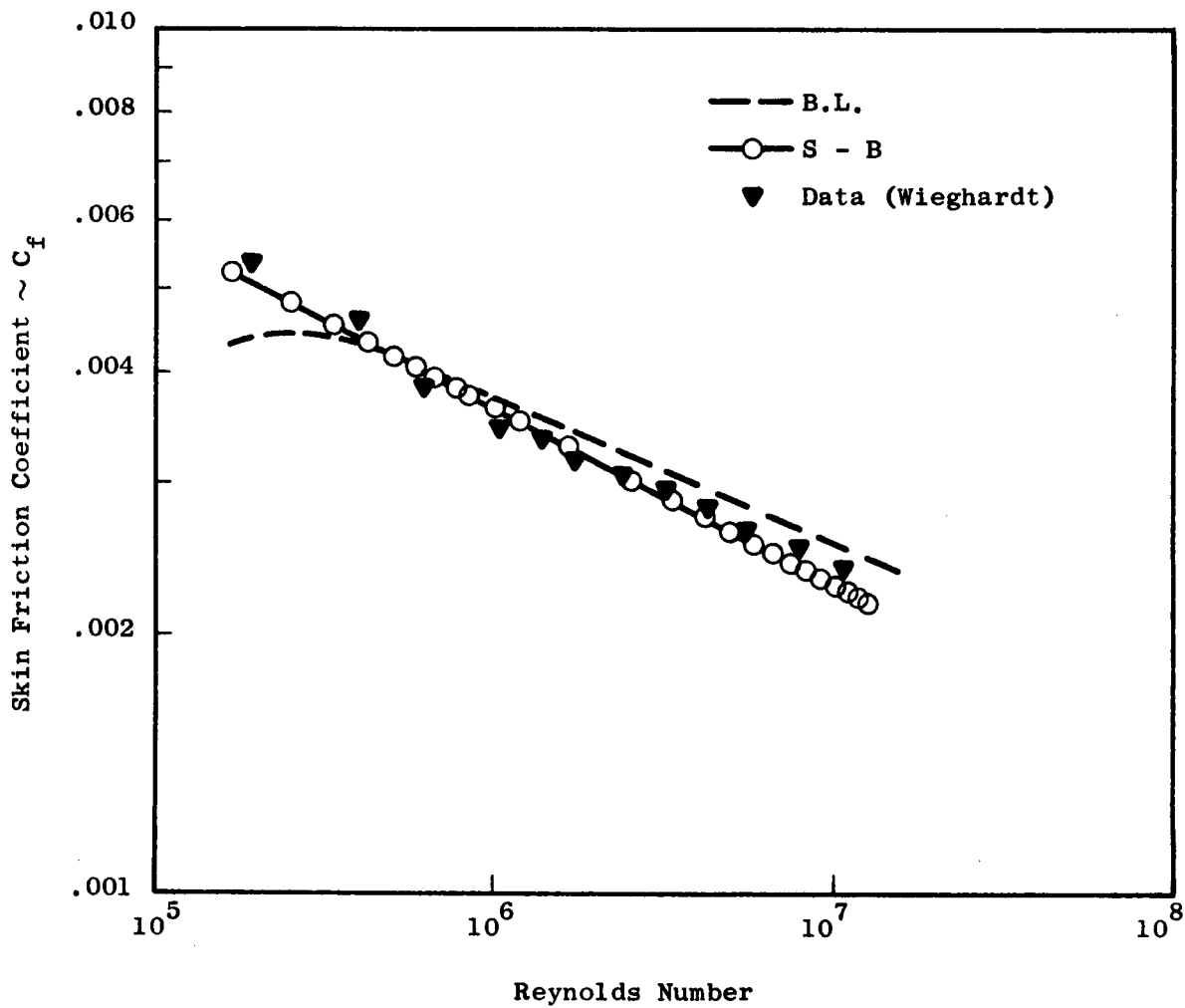
104

Figure 37. Incompressible Flat Plate.

10.2.2.2 Flat Plate with Pressure Gradient

Reference 29 reports the results of a study to experimentally determine the Reynolds Analogy factor on a flat plate mounted in the diverging section of a supersonic nozzle. Although most of the data taken in this study contained the effects of wall heat transfer, measurements of the momentum and displacement thickness distributions were made for the adiabatic wall case. These data are shown on Figures 38 and 39 along with the S-B predictions. The experimental pressure distribution started about 25% of the length of the plate from the leading edge. Therefore, the experimental pressure distribution was extrapolated to the leading edge, and the boundary layer was assumed to start from there. The predictions indicate good agreement with the data.

10.2.2.3 Waisted Body of Revolution

Figure 40 is a sketch of the waisted body tested by Winter, Rotta, and Smith (Reference 30). This work is usually recognized as one of the best available sources of compressible turbulent boundary layer data on a surface other than a flat plate. In addition, these data are frequently used as a basis for comparison for the various boundary layer prediction methods. Therefore, it serves as a standard reference from which the quality of these methods may be compared.

Figures 41 through 43 show the S-B and B.L. predictions of momentum thickness, displacement thickness, and skin friction coefficient, respectively, for a free-stream Mach number of 0.597. In general, the agreement with the data is very good for the momentum thickness and displacement thickness distributions of both S-B and B.L. However, at this Mach number, the skin friction predictions tend to be somewhat higher than the data. The B.L. predictions are closer to the data between $X/L = 0.3$ and $X/L = 0.7$, and the S-B predictions are closer between $X/L = 0.7$ and $X/L = 1.0$.

Similar predictions are made for free-stream Mach numbers of 1.404, 1.7, and 2.0. These predictions are compared with the data in Figures 44 through 52. In general, it can be said that in all cases the agreement is very good for both the S-B and the B.L. predictions. For engineering purposes, the primary advantage to using the S-B method is its extreme simplicity and almost negligible expense as compared to the finite difference method.

10.2.2.4 Supersonic Ramp - Adverse Pressure Gradient

Reference 31 reports the results of measurements of the turbulent boundary layer on each of three supersonic compression ramps. Although not a large quantity of data was taken, the skin friction coefficients were measured. Predictions using S-B are shown in Figure 53 along with the test data. The agreement is seen to be very good in all three cases.
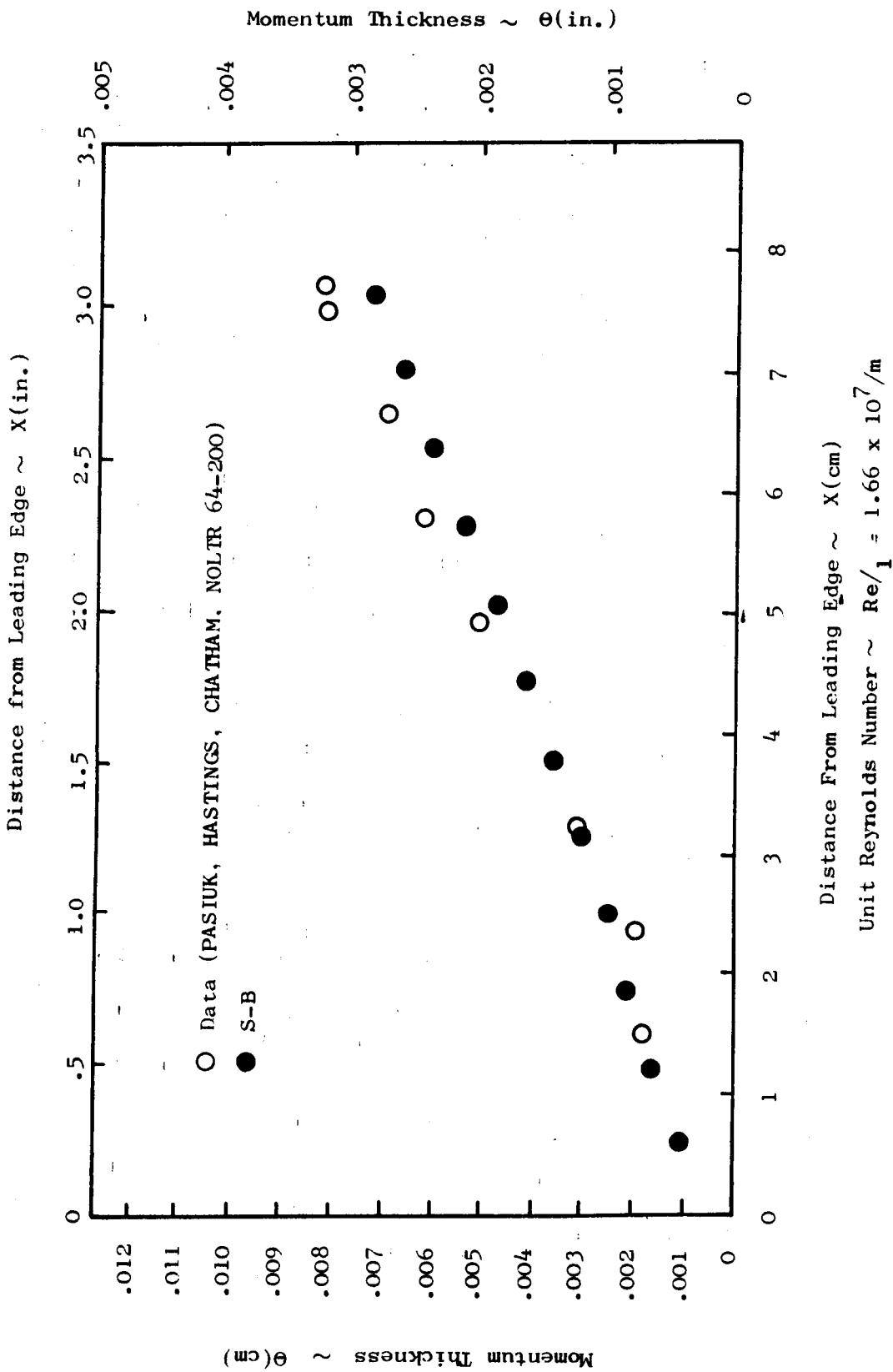
Figure 38. Flat Plate with Pressure Gradient, Momentum Thickness Vs. Distance from Leading Edge.
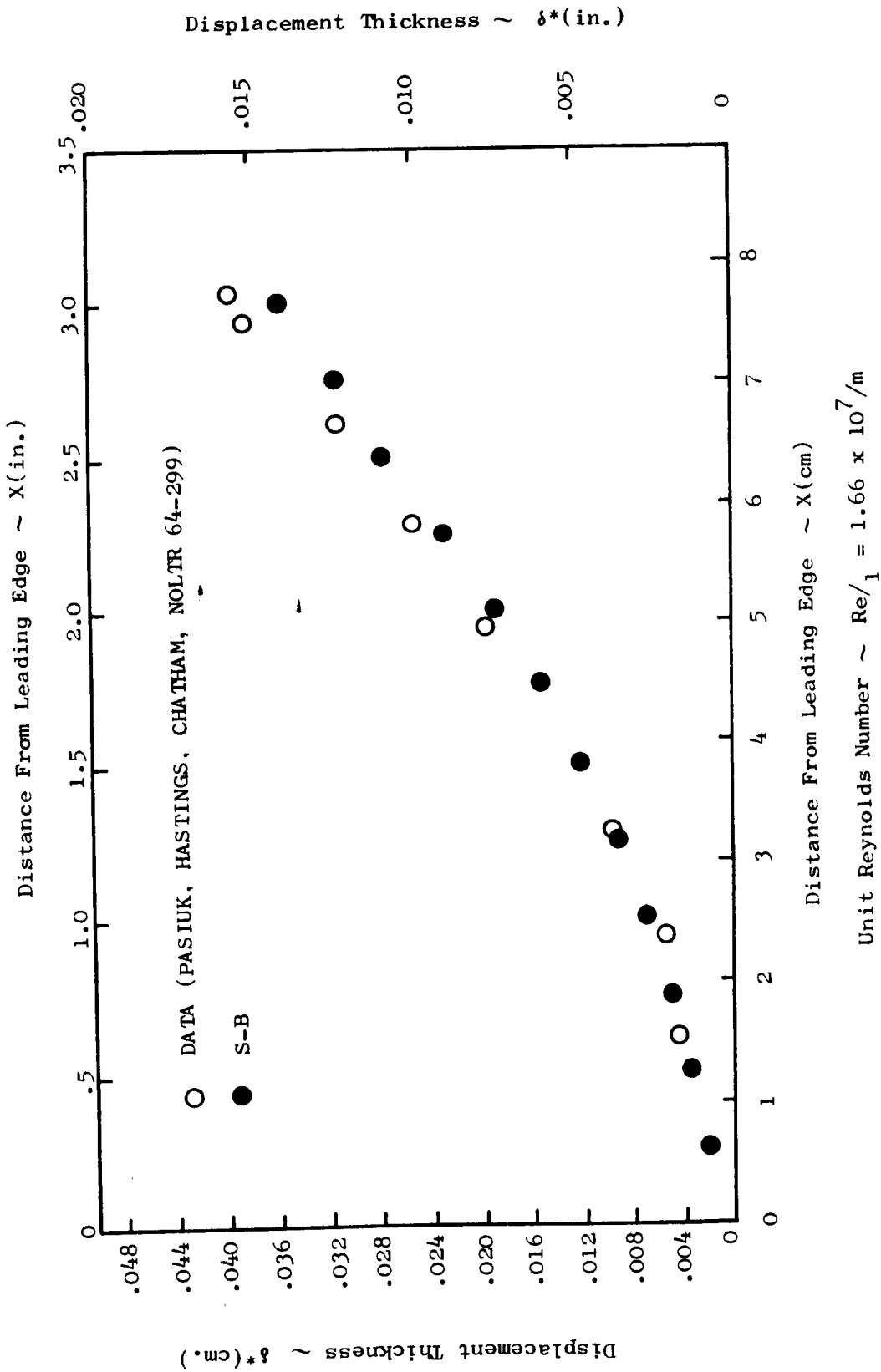
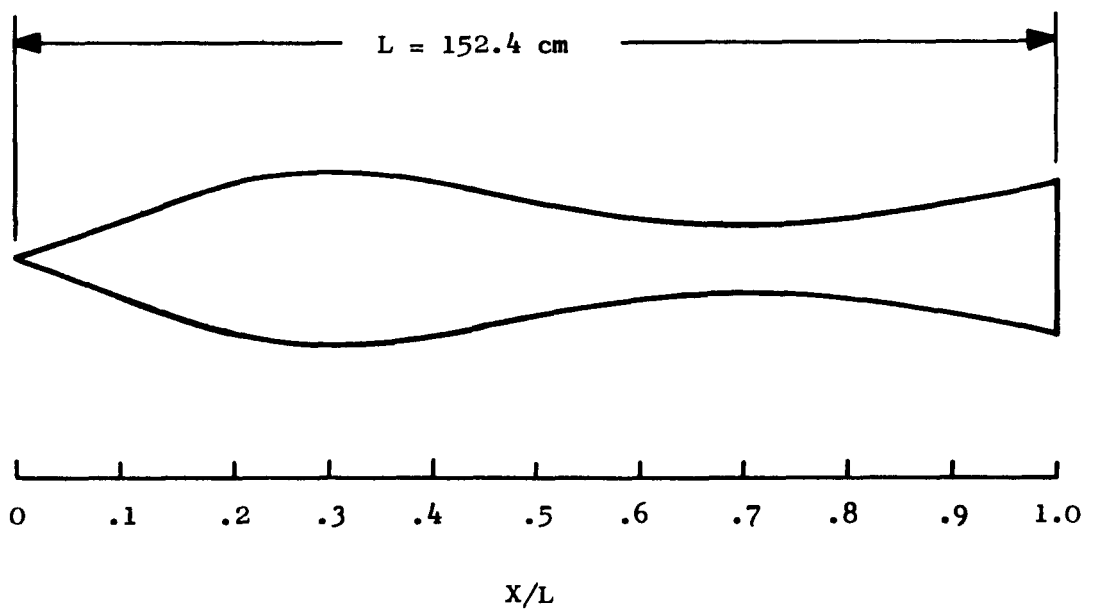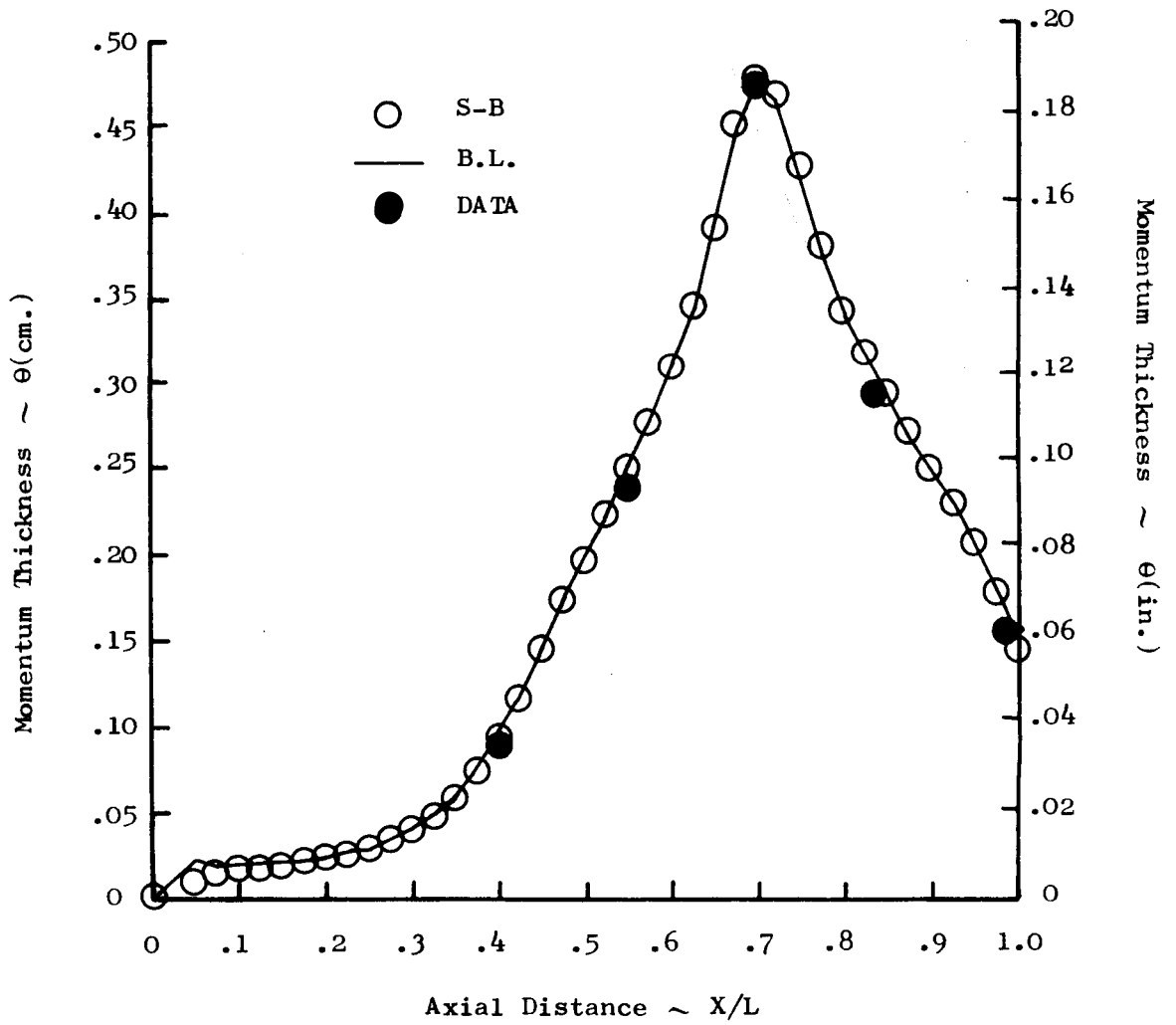Figure 39.   Flat Plate with Pressure Gradient, Displacement Thickness Vs. Distance from Leading Edge.

Figure 40. Waisted Body of Revolution.

Figure 41. Waisted Body Revolution, Momentum Thickness Vs. Axial Distance, $M_o = 0.597$.
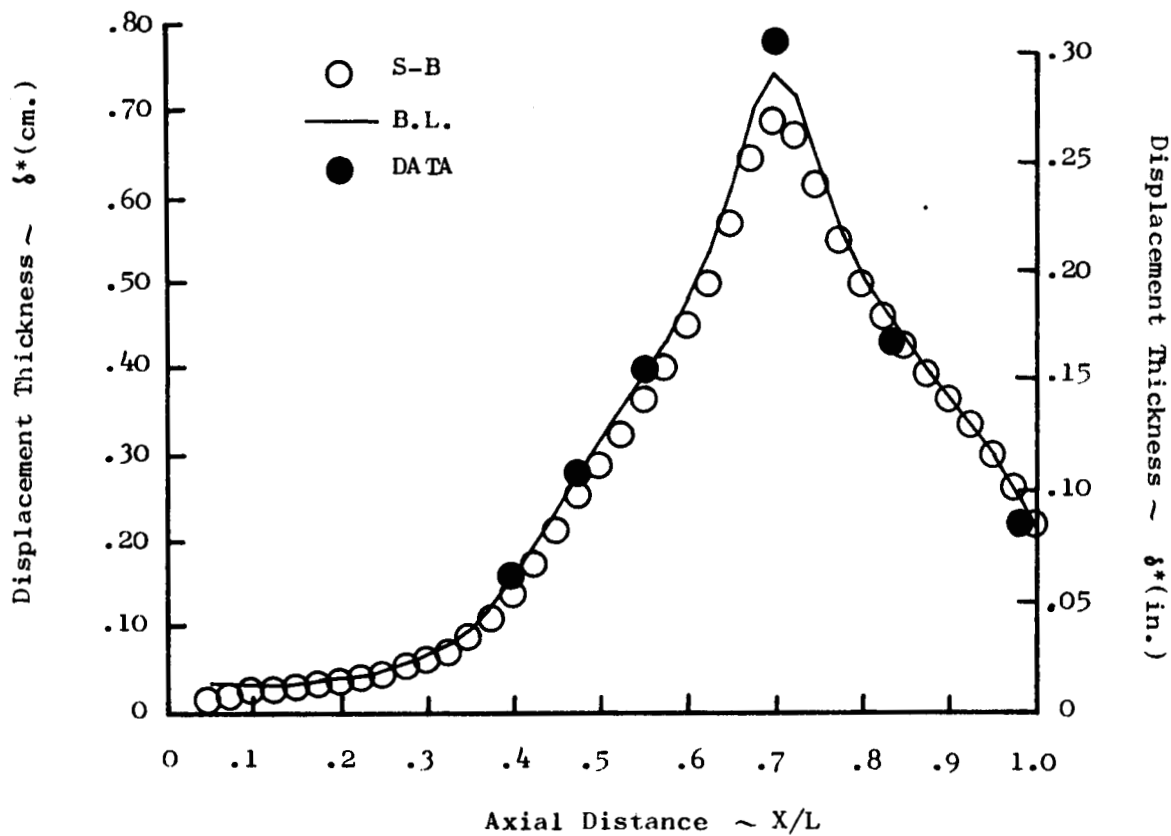
Figure 42. Waisted Body of Revolution, Displacement Thickness Vs. Axial Distance, $M_o = 0.597$.

The figure shows a plot of Skin Friction Coefficient ~ c_f (vertical axis, ranging from 0 to .006) versus Axial Distance ~ X/L (horizontal axis, ranging from 0 to 1.0).

Legend:
- ○ S-B
- —— B.L.
- ● DATA
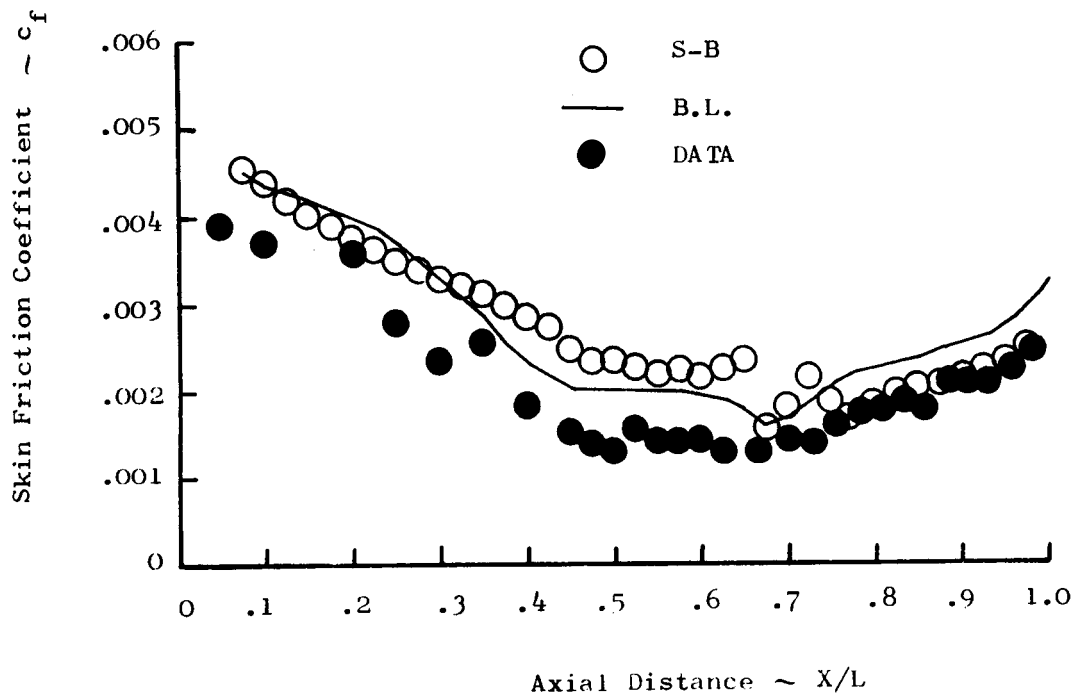
$$M_o = .597$$
$$Re/_l = 6.46 \times 10^6/m.$$

Figure 43. Waisted Body of Revolution, Skin Friction Coefficient Vs. Axial Distance, $M_o = 0.597$.
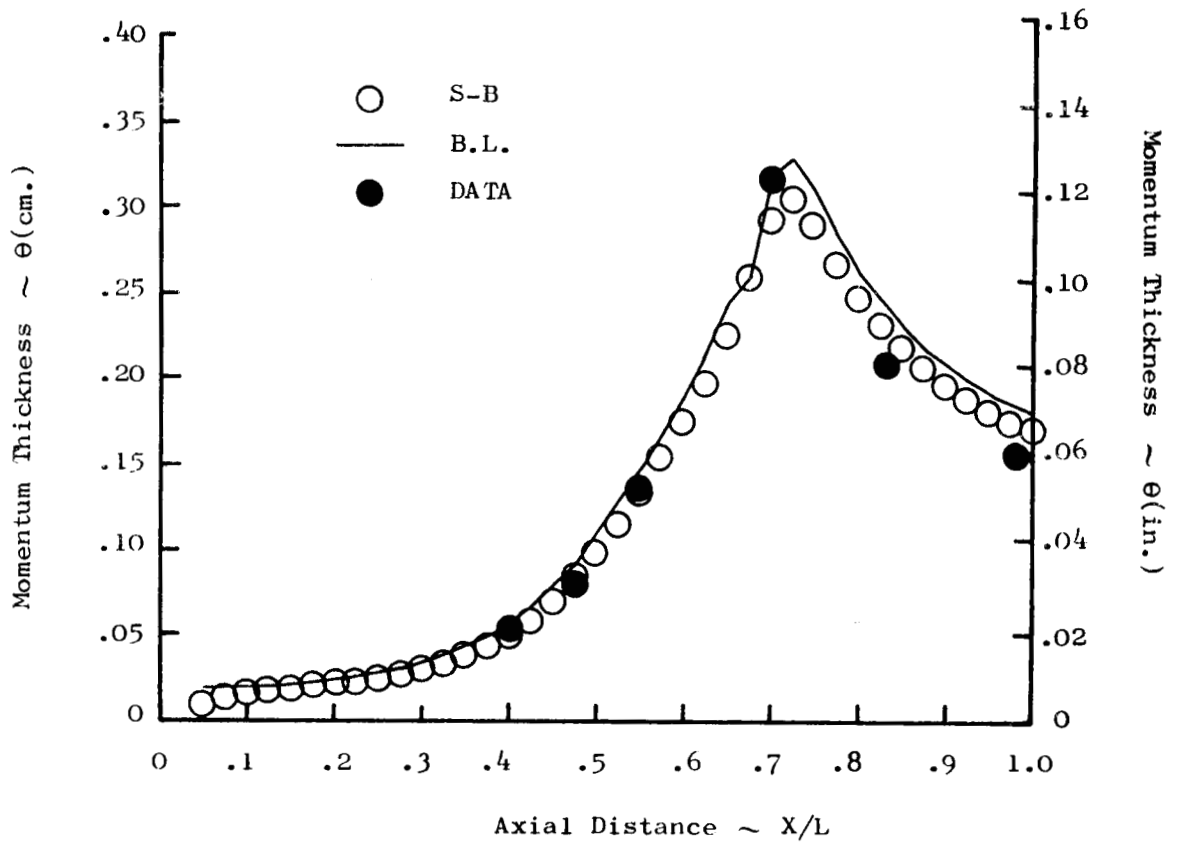
Figure 44. Waisted Body of Revolution, Momentum Thickness Vs. Axial Distance, $M_o = 1.404$.
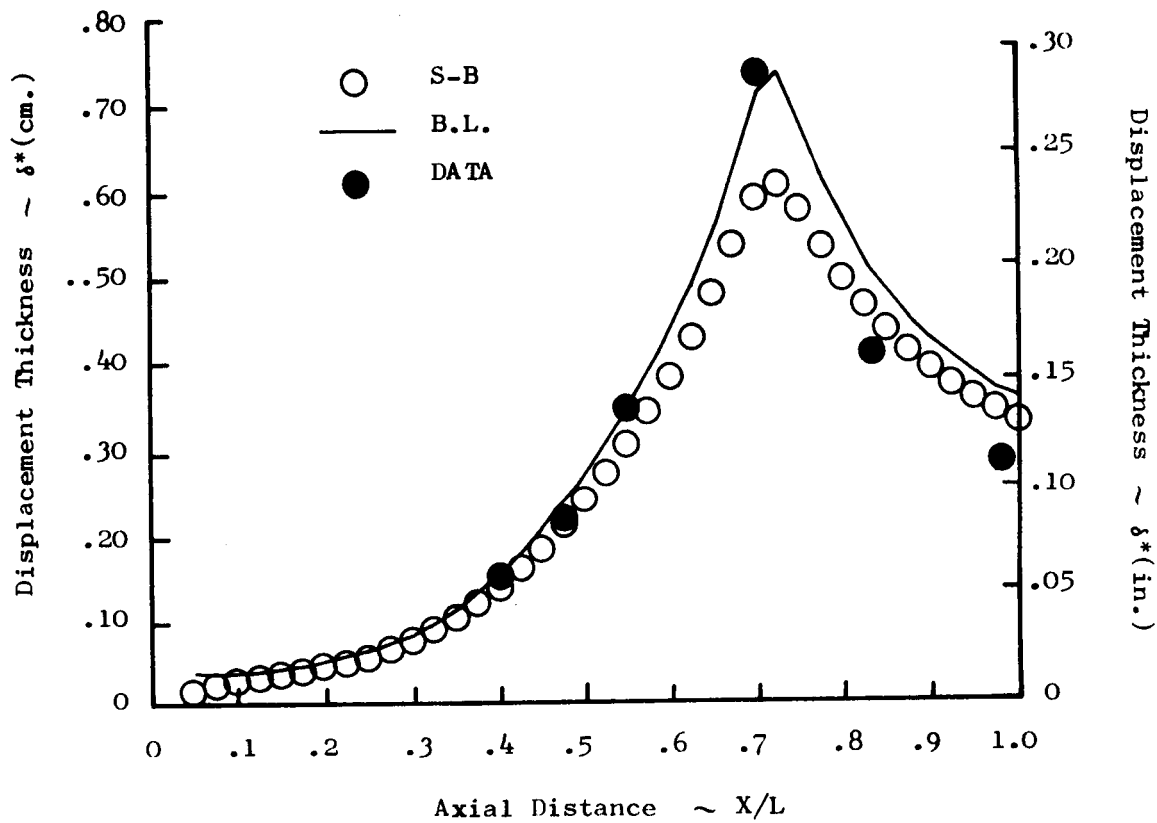
Figure 45. Waisted Body of Revolution, Displacement Thickness Vs. Axial Distribution, $M_o = 1.404$.
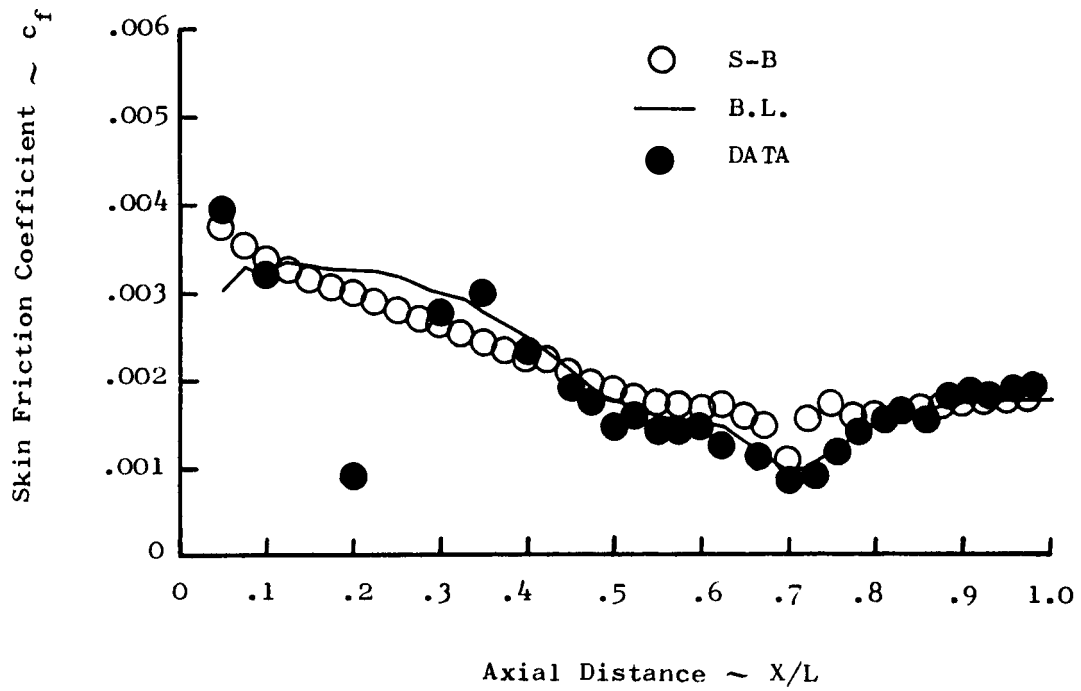
Figure 46. Waisted Body of Revolution, Skin Friction Coefficient Vs. Axial Distance, M_o = 1.404.

The plot's vertical axis is labeled "Skin Friction Coefficient $\sim c_f$" with values 0, .001, .002, .003, .004, .005, .006. The horizontal axis is labeled "Axial Distance $\sim$ X/L" with values 0, .1, .2, .3, .4, .5, .6, .7, .8, .9, 1.0.

Legend:
○ S-B
— B.L.
● DATA

M_o = 1.404
$Re/_1$ = 1.31 x 10^7/m.

Figure 47. Waisted Body of Revolution, Momentum Thickness Vs. Axial Distance, $M_o = 1.7$.
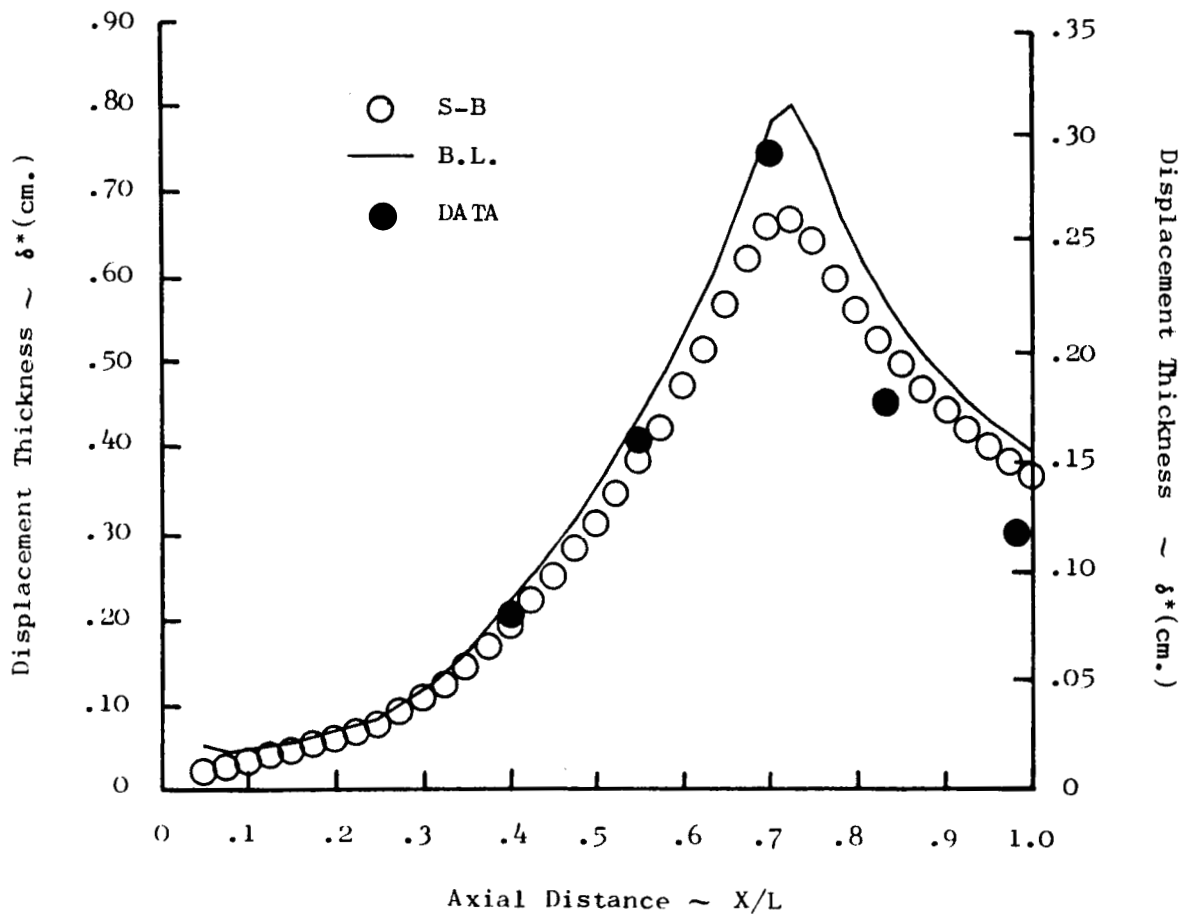
Figure 48.   Waisted Body of Revolution, Displacement Thickness Vs. Axial Distance, M_o = 1.7.

$$M_o = 1.7$$
$$Re/_l = 6.61 \times 10^6/m.$$

Figure 49. Waisted Body of Revolution, Skin Friction Coefficient Vs. Axial Distance, $M_o = 1.7$.
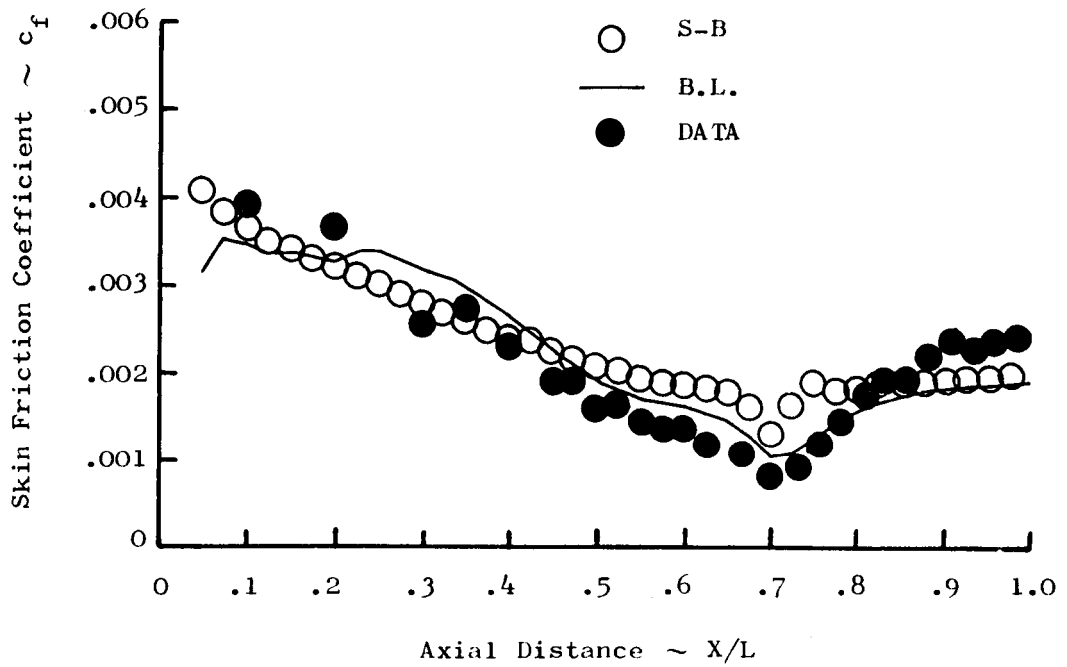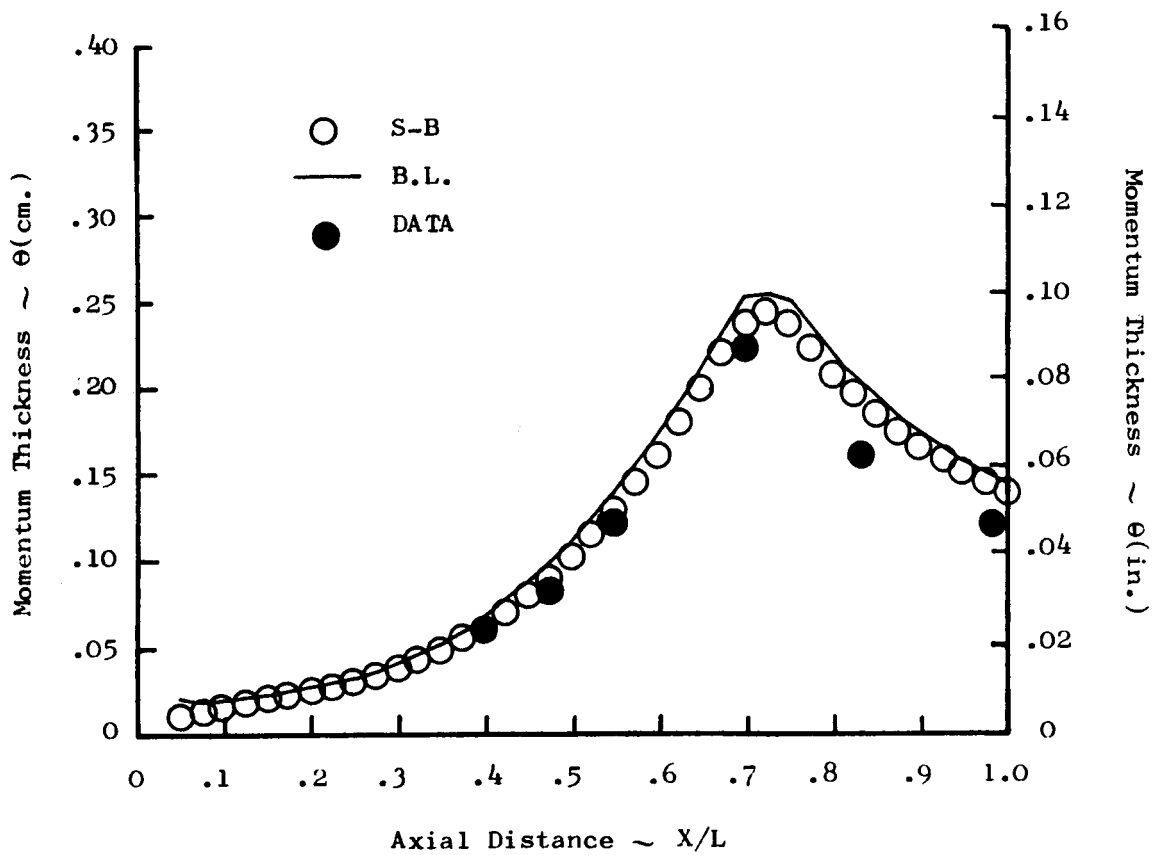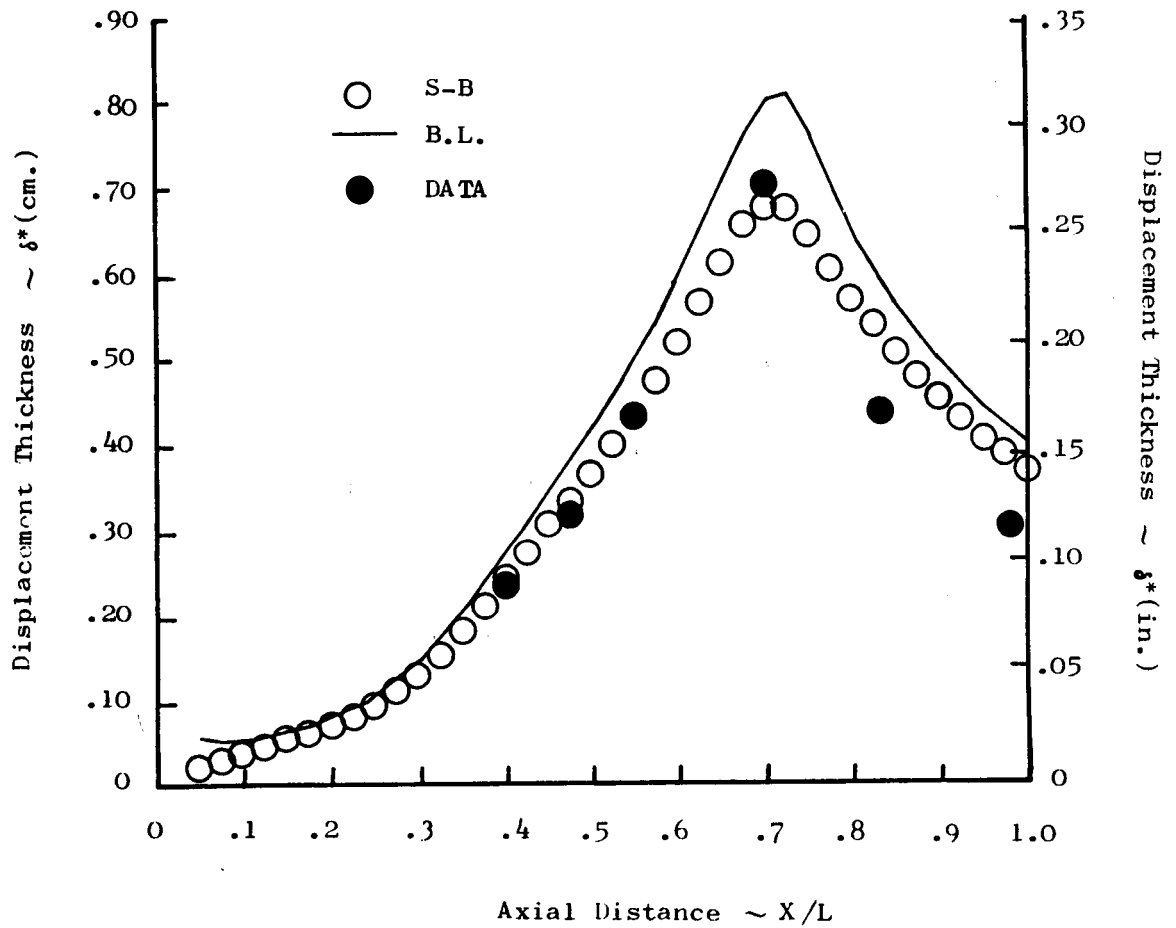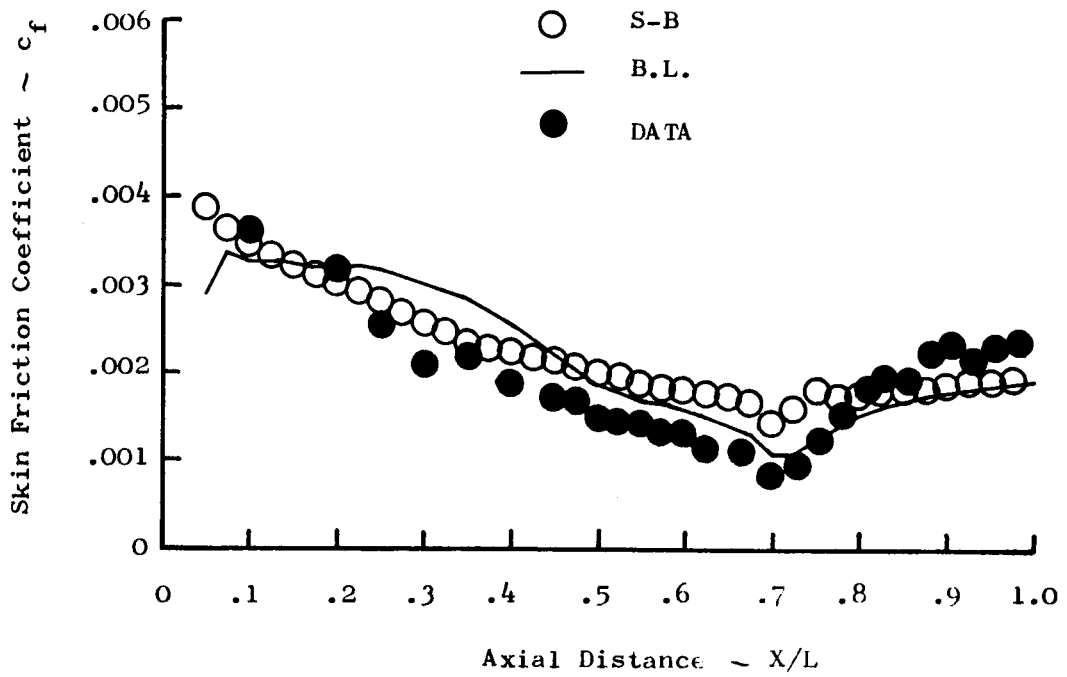
$$M_o = 2.0$$
$$Re/_1 = 6.54 \times 10^6/m.$$

Figure 50. Waisted Body of Revolution, Momentum Thickness Vs. Axial Distance, $M_O = 2.0$.

Figure 51.   Waisted Body of Revolution, Displacement Thickness Vs. Axial
Distance, M_o = 2.0.

$M_o = 2.0$

$Re/_1 = 6.54 \times 10^6/m.$

Figure 52. Waisted Body of Revolution, Skin Friction Coefficient Vs. Axial Distance, $M_o = 2.0$.

RAMP 1

C_f

.002 ━

.001

0

M_o ≈ 2.32
$Re/_1$ = 3.834 x 10^7/m.

○ DATA

── S-B

RAMP 2

C_f

.002 ━

.001

0

M_o = 2.31
$Re/_1$ = 3.85 x 10^7/m.

○ DATA

── S-B

RAMP 3

C_f

.002 ━

.001

1

M_o = 2.32
$Re/_1$ = 3.834 x 10^7/m.

○ DATA

── S-B

0   5   10   15   20   25

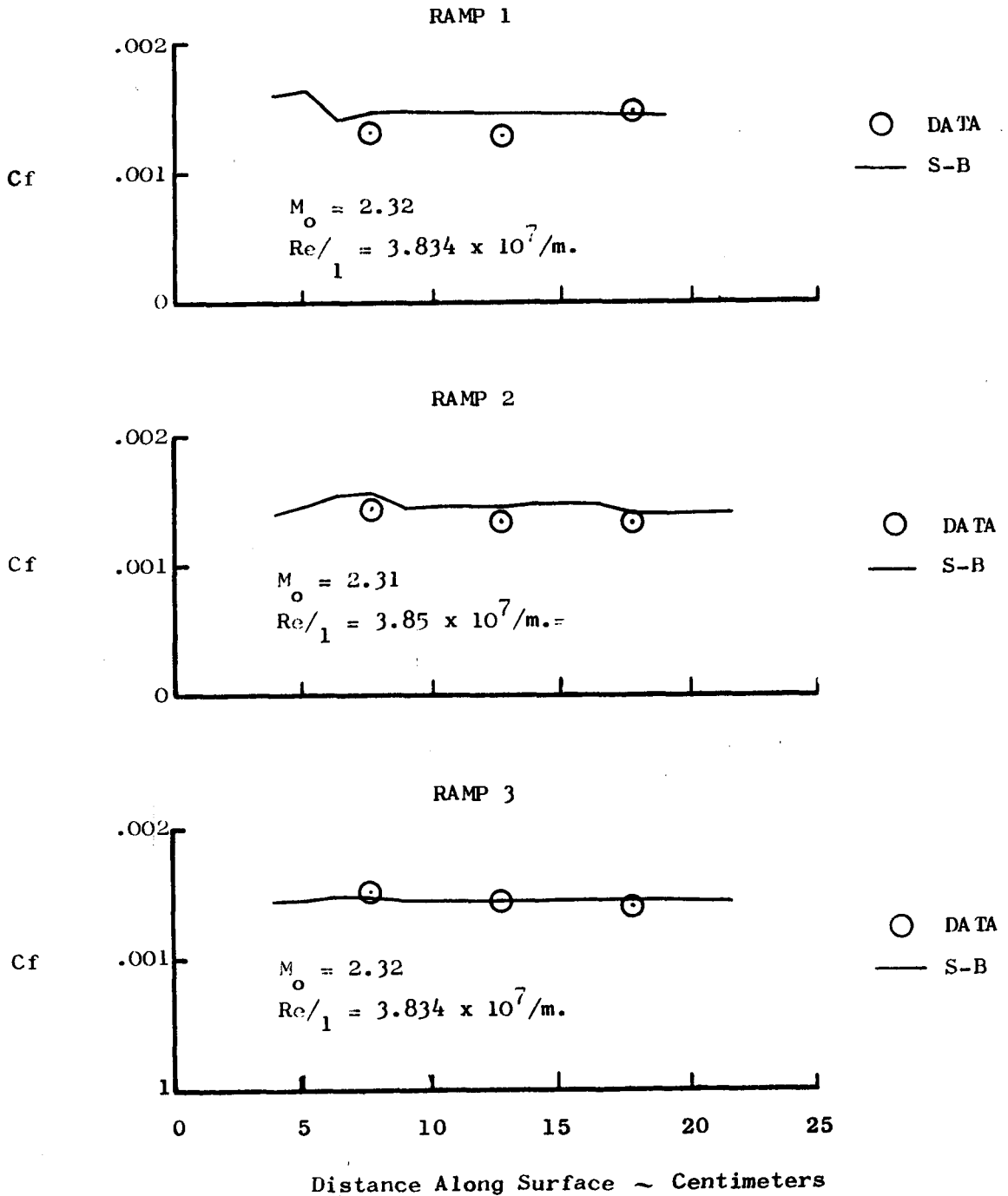Distance Along Surface ∼ Centimeters

Figure 53.   Skin Friction Coefficient on Supersonic Ramps.

10.2.3 Separation Prediction Method

In general, the prediction of turbulent boundary layer separation is best accomplished by performing a finite difference boundary layer solution over the given body surface. Separation is predicted at the point where the local skin friction coefficient becomes zero. Although this method provides reasonably accurate results, it requires a complete boundary layer solution which may not always be desired or necessary.

In the past the only other alternatives to a complete finite difference boundary layer solution were: 1) a complete integral boundary layer solution, or 2) the determination of some pressure gradient parameter which takes on a certain value at or near the separation point. The integral boundary layer solutions were known to give relatively large errors in skin friction coefficient near the separation point; and, as a result, predictions of separation were unreliable and inconsistent. Subsequent improvements in the integral methods allowed more accurate boundary layer skin friction calculations and, thus, separation predictions; however, they were accompanied by increased cost and complexity. The simple pressure gradient parameter methods of predicting separation have been used with some success for some flows. However, they have not received widespread use because they also have been unreliable and inconsistent.

Reference 32 reviews several methods for calculating incompressible turbulent boundary layer separation, and concludes that the Stratford method (Reference 33) quite satisfactorily predicts it. However, as is often the case, there is very little information regarding its usefulness for compressible flows. Therefore, the Stratford method was modified for compressibility and exercised on several compressible flow configurations where boundary layer separation was measured. In addition, General Electric's finite difference AERO Boundary Layer program was also run on several of these configurations to establish some sort of reference from which the quality of the Stratford predictions could be judged. Finally, this method has been incorporated into the NASA-Langley version of the STC/viscous analysis program.

Reference 33 presents the complete development of the basic theory for predicting the separation of an incompressible turbulent boundary layer. Only the basic ideas will be discussed here.

The method postulates that the turbulent layer can be divided into two distinct regions. In the outer region, the pressure rise just causes a lowering of the dynamic pressure profile, but does not change its shape. The losses due to shear stresses within this region are assumed to be almost the same as those on a flat plate under the influence of the same pressure rise. In the inner region, however, the inertia forces are too small to overcome the pressure gradient, and the velocity profile is distorted. In this region the pressure forces are balanced primarily by the tranverse gradient of shear.

Basically, Stratford pieces these two regions together, describing the outer region using the similarity power-law profile:

$$\frac{u}{U_o} = \left(\frac{y}{\delta}\right)^{1/n} \tag{150}$$

and the inner region using the reduced boundary layer momentum equation:

$$\frac{\partial \tau}{\partial y} = \frac{dP}{dx} \tag{151}$$

Utilizing Equation 150 and the definition of the stream function $\Psi = \int u\,dy$, one can arrive at the following expressions for the outer region:

$$\frac{\partial u}{\partial y} = \frac{U_o}{n\delta}\left(\frac{y}{\delta}\right)^{1/n - 1} \tag{152}$$

$$u = U_o\left(\frac{y}{\delta}\right)^{1/n} \tag{153}$$

and,

$$\Psi = \frac{n\,U_o\delta}{n + 1}\left(\frac{y}{\delta}\right)^{1 + 1/n} \tag{154}$$

Integrating Equation 151 and utilizing Prandtl's mixing length expression, one can arrive at the following expressions for the inner region when the shear stress is equal to zero:

$$\frac{du}{dy} = \left(\frac{1}{\beta^2 K^2}\ \frac{dP}{dx}\ \frac{1}{\rho y}\right)^{1/2} \tag{155}$$

$$u = \left(\frac{4}{\beta^2 K^2}\ \frac{dP}{dx}\ \frac{y}{\rho}\right)^{1/2} \tag{156}$$

$$\Psi = \frac{4}{3}\left(\frac{1}{\rho\beta^2 K^2}\ \frac{dp}{dx}\right)^{1/2} y^{3/2} \tag{157}$$

124

The K is the Karman constant, and β is an empirical constant introduced to account for the fact that Equation 151 is only approximate near the wall and exact only at the wall. In addition, the mixing length expression changes with increasing distance from the wall. Therefore, it is expedient to account for these effects by incorporating the single empirical factor β, whose value is determined by experiment.

At the interface between the inner and outer layers, u, du/dy, and Ψ must be continuous. Therefore, equating them and performing some algebraic manipulations one finally arrives at the expression:

$$\left(\frac{y}{\delta}\right)^{(2n-4)/n} = \frac{3(K\beta)^4}{(n+1)\left(n\delta \frac{dc_p}{dx}\right)^2} \tag{158}$$

where $C_p = \dfrac{P-P_o}{1/2\,\rho U_o^2} = 1 - \dfrac{u_e^2}{U_o^2}$ for incompressible flow.

If it is assumed that:

$$\frac{\delta}{x} = 0.37\,Re_x^{-1/5} \tag{159}$$

$\beta = 0.66$

$K = 0.41$ and $n = 6$

then Equation 158 can be written as:

$$C_p\left(x\frac{dc_p}{dx}\right)^{1/2}\left(10^{-6}\,Re_x\right)^{-0.10} = F(x) \cong 0.35 \tag{160}$$

This equation assumes turbulent flow throughout and is only applicable in an adverse pressure gradient. When there is a region of favorable pressure gradient or the turbulent boundary layer starts at other than a leading edge, the surface length coordinate X is replaced by $S = X + X'$. The distance X' represents the virtual origin of the turbulent boundary layer at the minimum pressure point prior to the start of the pressure rise

or adverse pressure gradient. The virtual origin X' is calculated by using Equation 145a or 145b as shown in Figure 54. Hence, the upstream history of the boundary layer is included in the definition of the separation parameter.

According to the analysis, Equation 160 will predict separation when $F(x) = 0.35$ for incompressible flow. However, for a typical turbulent boundary layer flow, $F(x)$ increases prior to separation and decreases after separation. Therefore, after applying this method to several flows with turbulent separation, Stratford observed that if the maximum value of $F(x)$,

a. is greater than 0.4, separation is predicted when $F(x) = 0.4$,

b. lies between 0.35 and 0.4, separation occurs at the maximum value,

c. is less than 0.35, separation does not occur.

This method works quite well for incompressible flows as shown in Reference 32. However, in order that the method be useful for solving problems of more current interest, it must be extended to account for compressibility. The approach taken here is one dictated by expediency and physical reasoning rather than mathematical rigor. Basically the philosophy of the approach is as follows.

The physical ideas postulated for the incompressible case are expected to apply in the compressible case. Therefore, rather than quantitatively alter the formulation of the problem to account for variable density, assume that Equation 160 is still valid but with the following exceptions. First:

$$C_p = 1 - \frac{ue^2}{U_o^2} \text{ is replaced by } C_p = 1 - \frac{M_e^2}{M_o^2}, \text{ and second, the}$$

critical range of the function $F(x)$ is now different from that for incompressible flows.

Now, the only remaining task is to determine the new critical range for $F(x)$. This is accomplished in the following way. By computing $F(x)$ using Equation 160 and the pressure distribution for a compressible separated flow, determine the value of $F(x)$ corresponding to the measured separation point. Once this is done for a number of cases, one can determine the upper limit for $F(x)$. The lower limit is determined in the same manner, however, this time the calculations are done for compressible flows with adverse pressure gradient where it is known that the boundary layer does not separate. The greatest difficulty encountered in trying to determine the appropriate critical range for $F(x)$ is the general lack of good compressible separated flow experimental data. Even though this difficulty exists, it is felt that there is enough good data available with which to determine this critical range. Figure 55 was derived from the data of References 32 through 38.

Figure 54. Definition of Lengths in Separation Function.
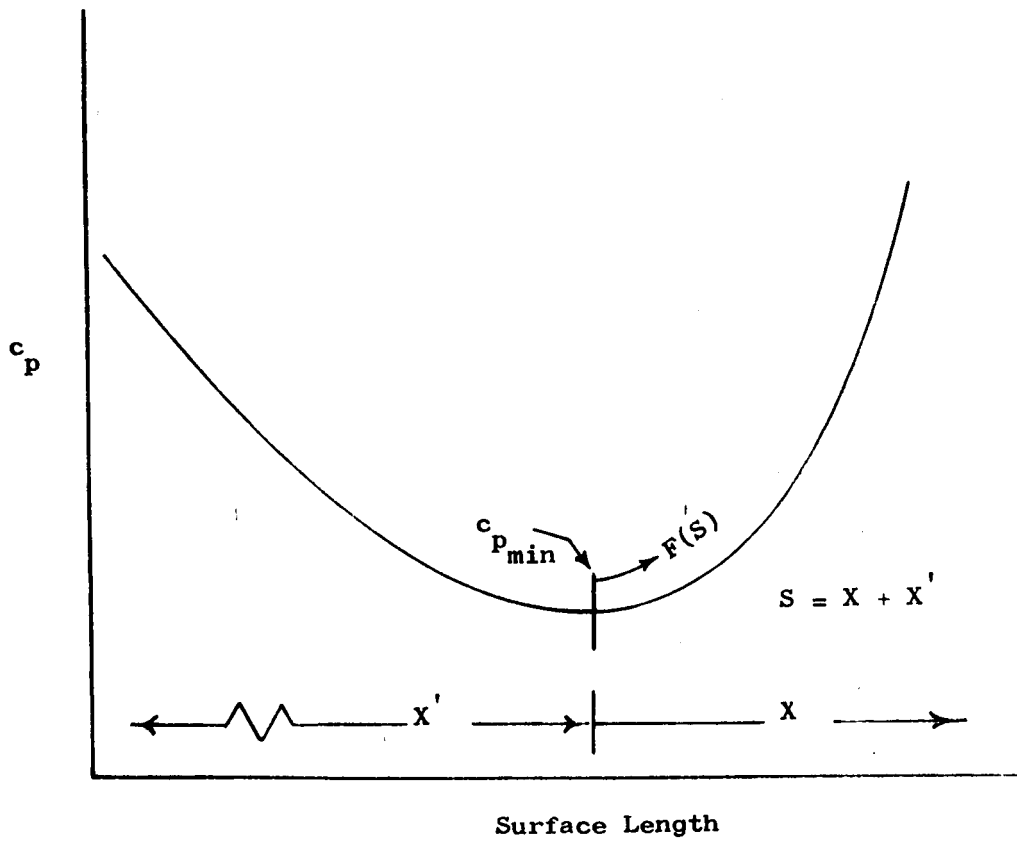
$$X' = X_{x=0} = \frac{1}{Pr^a} \int_{x=-1}^{x=0} Pr^a \, dx$$
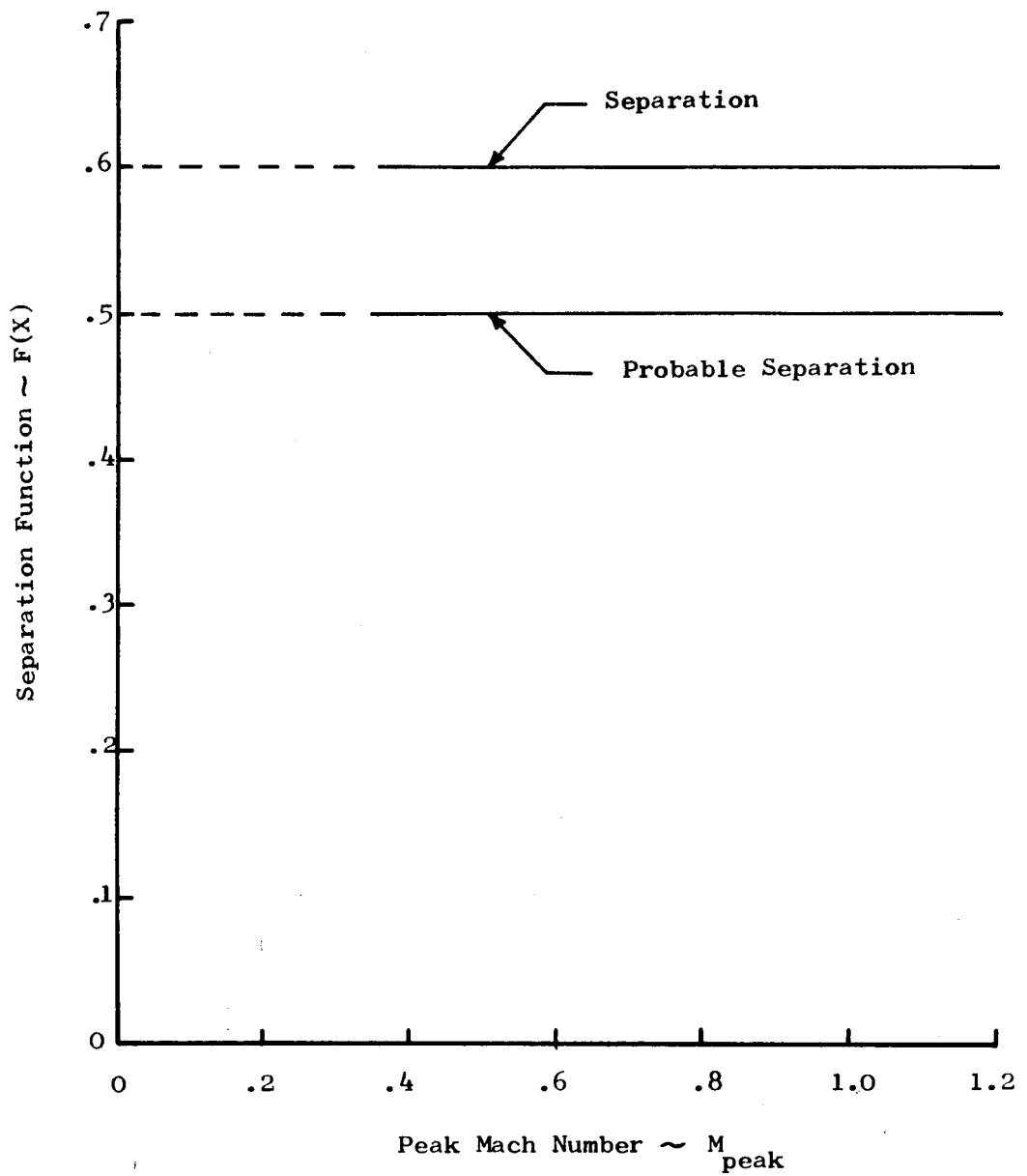
Figure 55. Separation Functions Vs. Peak Mach Number.

It shows the critical range of $F(x)$ for determining if separation occurs. The only region for which no data were found is that region between $M = 0$ and $M_{peak} = 0.354$. This region is bracketed by the dashed lines; however, it is expected that, for peak Mach numbers within this range, reliable engineering estimates can be made using the assumed linear variations shown.

10.2.4 Example Cases - Separation

The Stratford method has been used to evaluate several experimentally derived pressure distributions to determine how well it predicted the measured separations. Cases have been found between incompressible flows and compressible flows at Mach numbers as high as 4.92. Each of these cases will be discussed.

10.2.4.1 Airfoil - Incompressible Flow

The well-known airfoil-type body tested by Schubaur and Klebanoff (Reference 34) was selected to check out the program. First the S-B boundary layer program was run using the test pressure distribution. At the minimum pressure point, the equivalent flat plate length is obtained directly from the boundary layer output. This then serves as the length to the boundary layer virtual origin which is required in the separation calculation. Figure 56 shows the airfoil, measured pressure distribution, and the predicted and measured separation locations. The agreement is seen to be very good. The AERO Boundary Layer Program did not predict separation to occur on the airfoil.

10.2.4.2 Forward Facing Step - Subsonic Flow

The subsonic compressible data of Chapman, Kuehn, and Larson (Reference 35) is ideal for determining how well the Stratford method is able to predict separation because the exact boundary layer origin is known. The measured pressure distribution and predicted and measured separation locations are shown in Figure 57. The agreement is seen to be excellent.

10.2.4.3 Circular Arc Airfoil - Subsonic Flow

The circular arc airfoil data of Reference 36 were analyzed in a manner similar to that of the Shubaur and Klebanoff airfoil. That is, the measured pressure distribution was used to compute the boundary layer origin at the minimum pressure point. This equivalent flat plate length is then input into the STRTFD (S-B) program. This procedure was used for each of the four free-stream Mach numbers shown in Figure 58. The fact that the predicted separation locations are closer to the measured ones for the 0.354 and 0.663 free-stream Mach numbers is probably due to the somewhat uncertain initial boundary layer conditions. Since the airfoil is just a bump on the wind tunnel wall, with suction and blowing slots upstream of the leading edge, the actual boundary layer height is not known as accurately as is desired. This affects the equivalent flat plate length which is calculated at the minimum pressure point on the airfoil, which, in turn, affects the value of the predicted
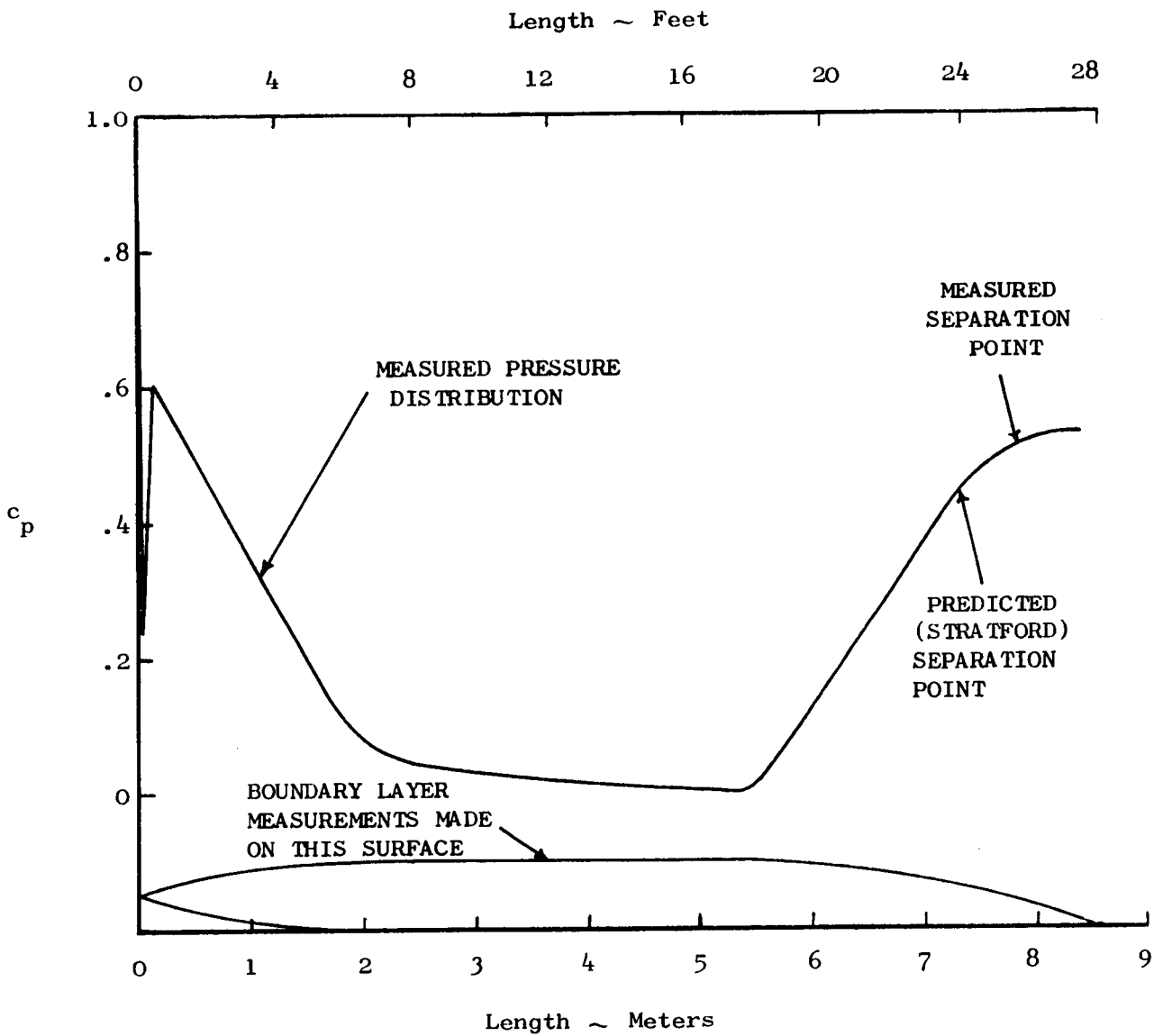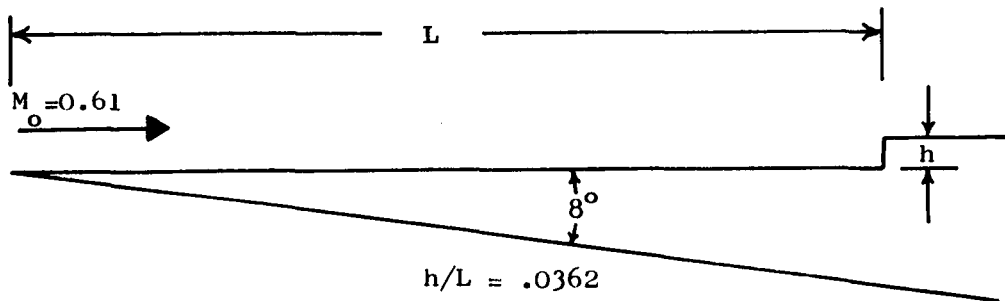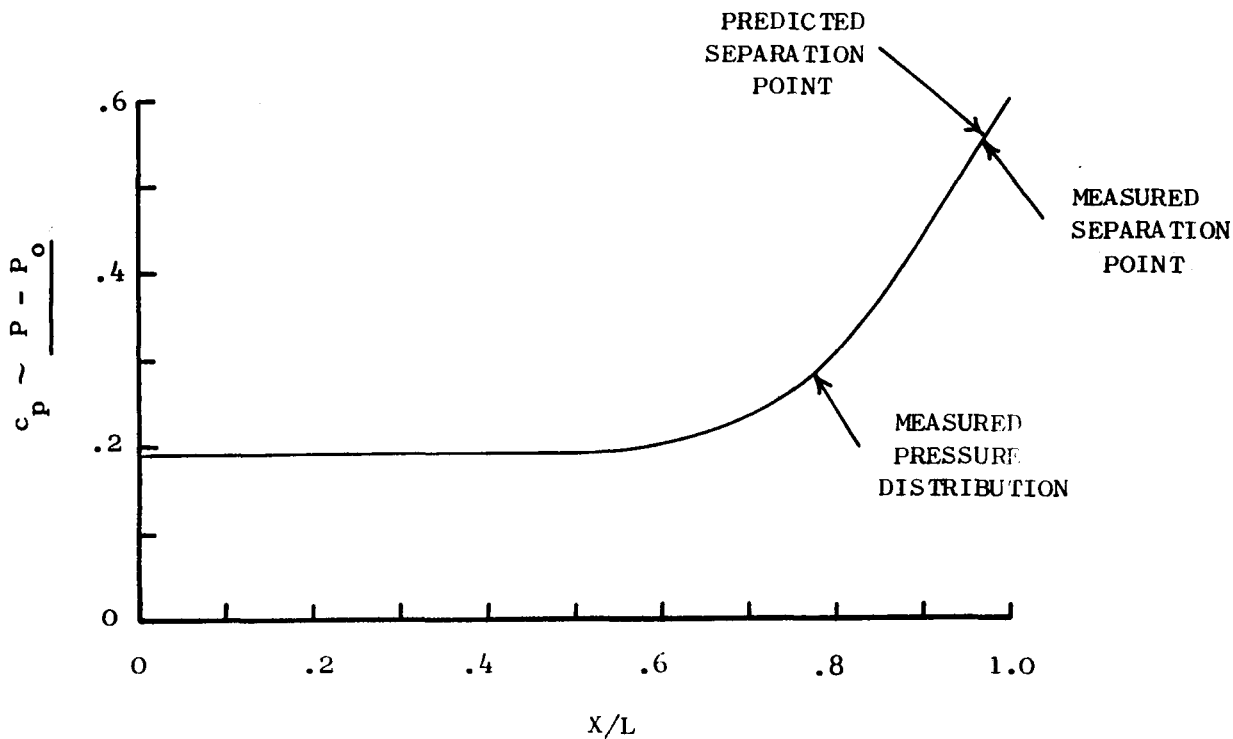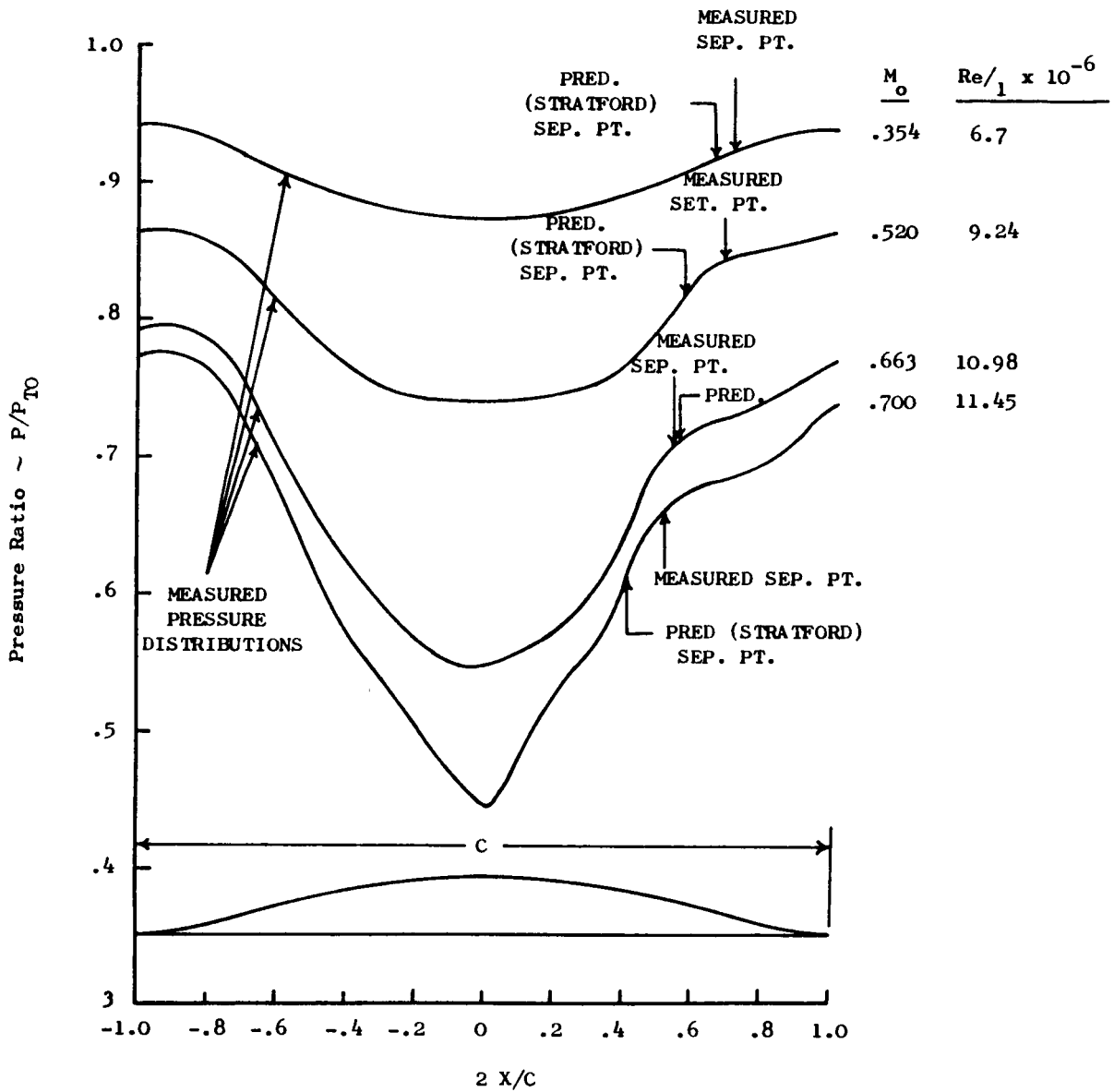
129

Figure 56. Data of Schubaur and Klebanoff.

$$c_p = \frac{P - P_{Min}}{\frac{1}{2}\, \rho U^2_{Max}}$$

Incompressible Flow

$$Re/_1 = 2.9 \times 10^6/m.$$

Figure 57. Data of Chapman, Kuehn, and Larson.

Figure 58.   Data of Alber, Bacon Masson, and Collins.

separation point. Even though these differences occur, they introduced only small inaccuracies.

10.2.4.4 Flat Plate Shock Boundary Layer Interaction - Supersonic Flow

Seddon (Reference 37) has studied the shock boundary layer inter-action on a flat plate. The mechanism for introducing the pressure gradient on the flat plate is the normal/oblique shock created by a second plate located above the first. The incident shock wave interacts with the plate boundary layer and causes a steep, but not discontinuous pressure rise. The measured pressure distribution and measured separation point are shown on Figure 59 along with the predicted separation point. Again the agreement is seen to be excellent.
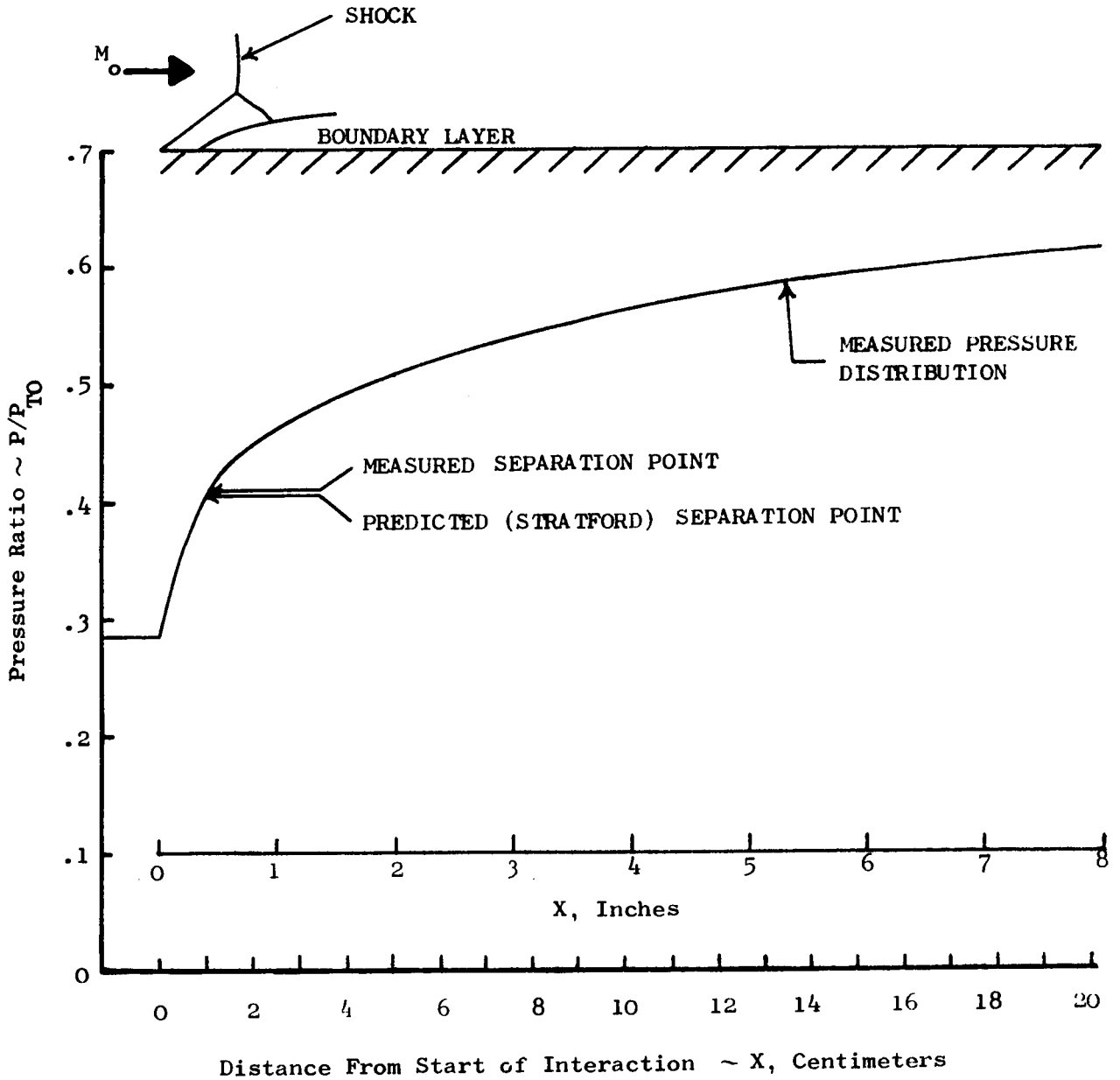
10.2.4.5 Wedge - Supersonic Flow

An experimental study of the conditions necessary to promote boundary layer separation in the compression corner created by the intersection of a wedge and a plane wall at very high Reynolds numbers is reported in Reference 38. In this study the wedge/wall intersection was formed by a forward hinged plate in the wind tunnel floor. Changing the wedge angle was accomplished by simply swinging the hinged plate through the desired angle. There were many conditions simulated in this test, and only three were ana-lyzed with the Stratford method. These were selected randomly from all the available cases. Figures 60 and 61 show the measured pressure distributions along with the predicted and measured separation points for a free-stream Mach number of 2.95. The only difference between the two figures is the wedge angle. Figure 62 shows these same variables at a free-stream Mach number of 4.92. These cases were selected to demonstrate the ability of the method to predict turbulent separations even for very high Mach numbers and Reynolds numbers. One should also note in Figure 62 that the finite difference Boundary Layer Program tends to predict separation sooner than does the Stratford method.

10.2.5 Data Comparisons - Axisymmetric Inlets

The predicted pressure distributions on the NASA ATT inlet No. 8 (NASA 1-85-100) have been compared with the measured surface pressures recorded on the through-flow nacelle during testing in the 16-foot tunnel at NASA-Langley. In Section 4.3, at the beginning of this book, the emphasis was on the predicted results from the Streamtube Curvature analysis. It was evident then that the boundary layer displacement effects and separation had a significant influence near the leading edge of the inlet lip. Now, the viscous characteristics will be discussed in more detail. Two figures from Section 4.3 at the beginning of this book will be repeated with ad-ditional information noted.
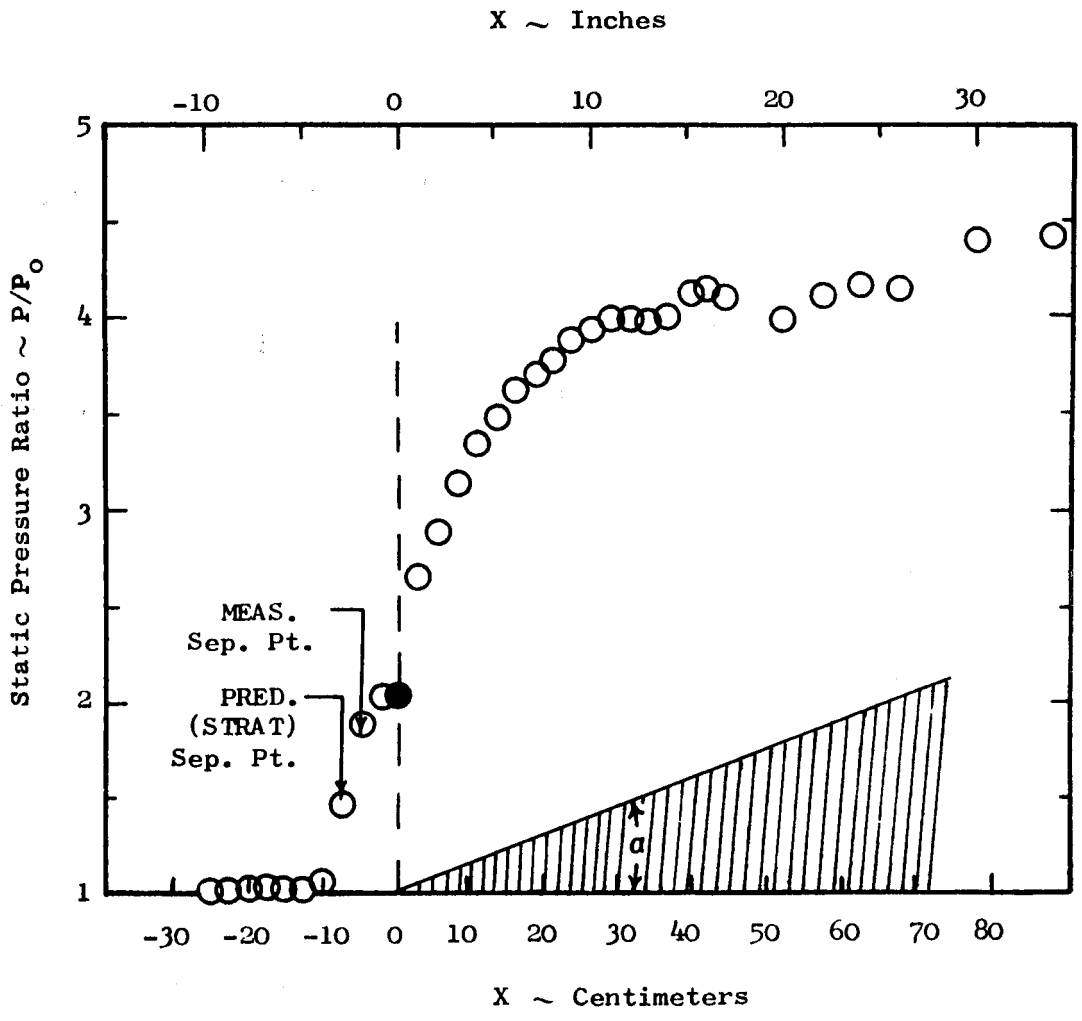
At a free-stream Mach number of $M_o = 0.8$ and a mass flow ratio of 0.81, the streamtube curvature analysis with viscous effects included pre-dicts the surface pressures shown in Figure 63. On the internal surface

SHOCK

M_o

BOUNDARY LAYER

MEASURED PRESSURE
DISTRIBUTION

MEASURED SEPARATION POINT

PREDICTED (STRATFORD) SEPARATION POINT

Pressure Ratio ~ P/P_{TO}

X, Inches

Distance From Start of Interaction ~ X, Centimeters

$M_o = 1.47$

$Re/_1 = 1.31 \times 10^7/m.$

Figure 59. Basic Interaction Data of Seddon.

Figure 60. Data of Rhomke and Roshko.

X ~ Inches

Static Pressure Ratio ~ P/P$_o$

MEAS.
Sep. Pt.

PRED.
(STRATFORD)
Sep. Pt.

X ~ Centimeters

M$_o$ = 2.95

Re/$_1$ = 1.62 x 10^6/m.
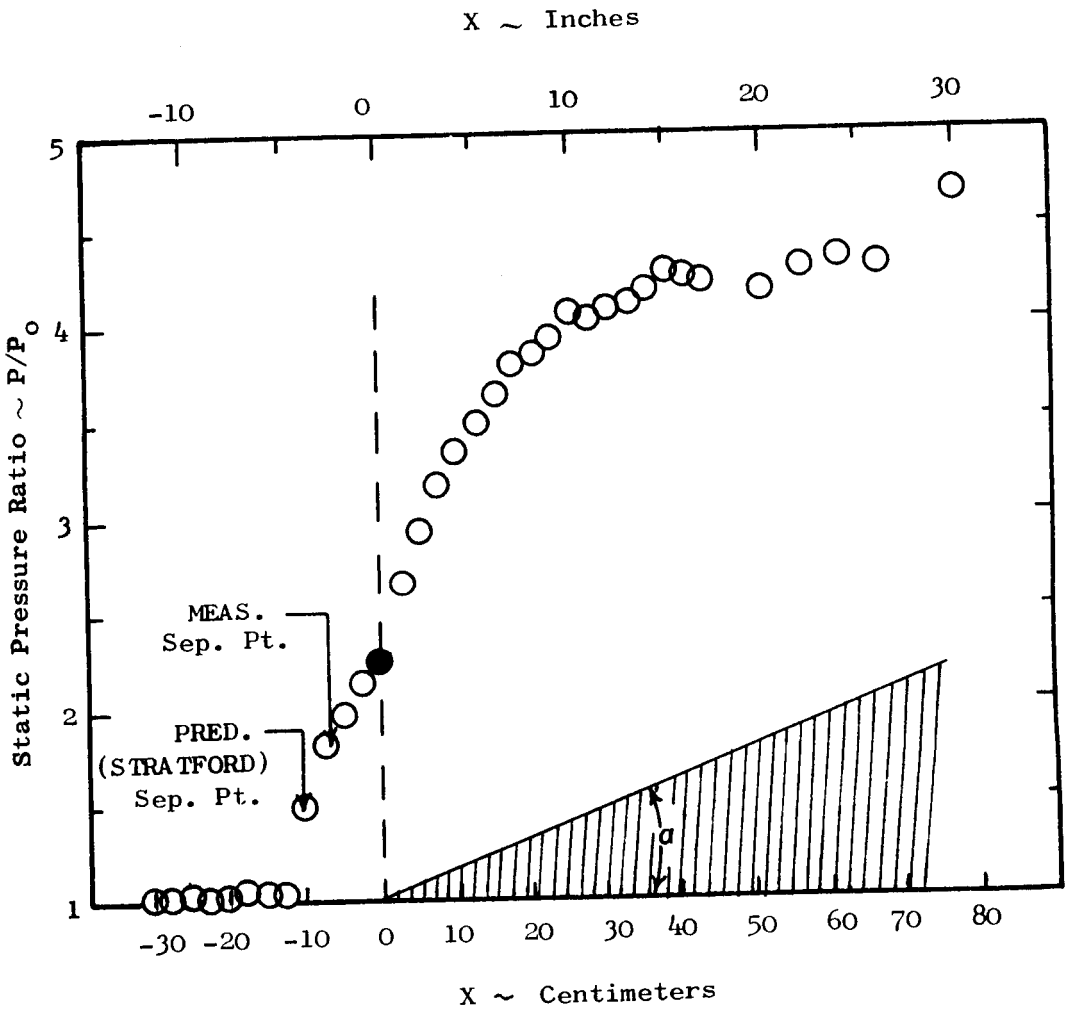
Wedge Angle (α) = 21.88^o

Figure 61.   Data of Thomke and Roshko.

Figure 62. Data of Thomke and Roshko.
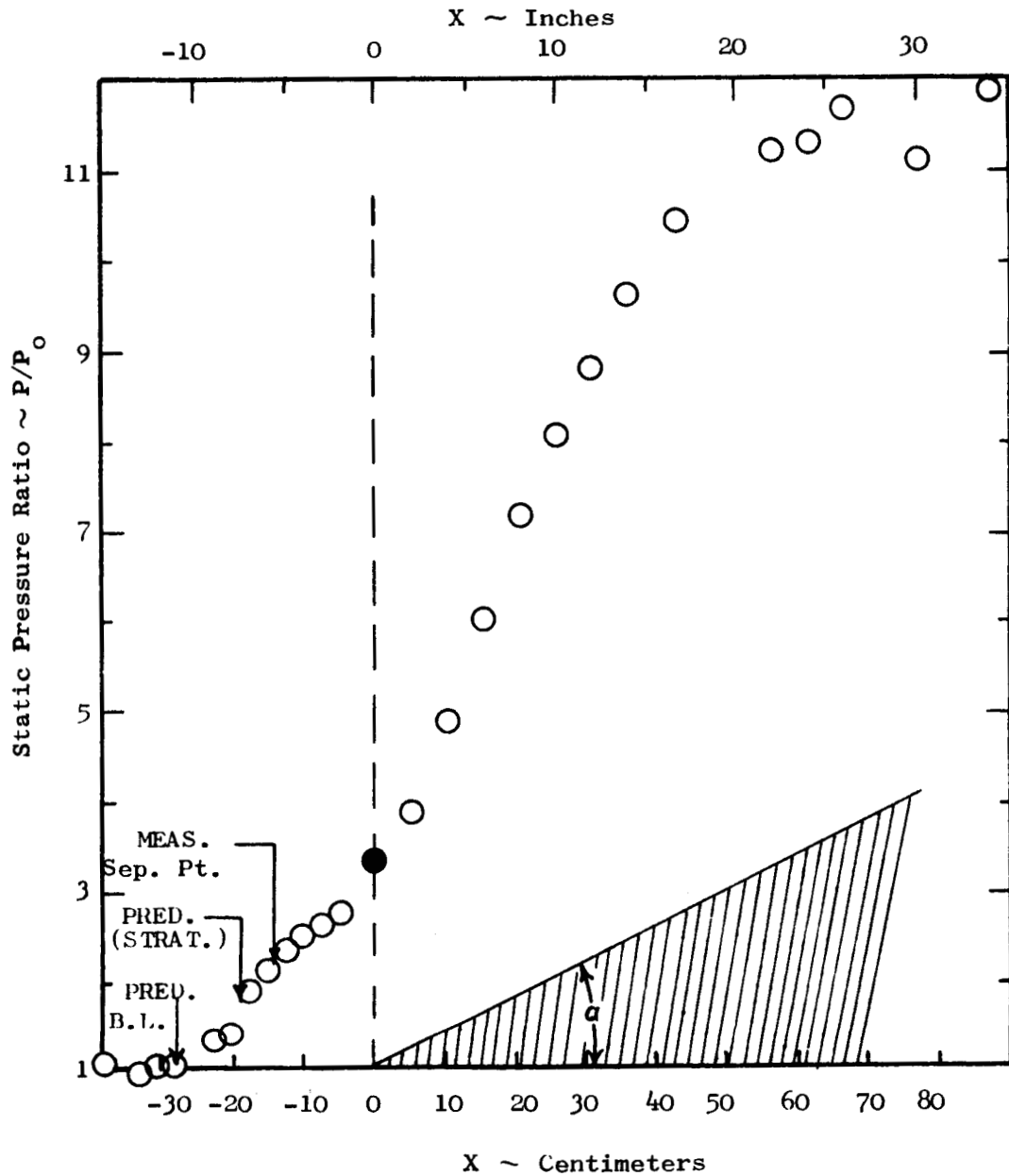
$M_o = 4.92$

$Re/_1 = 3.78 \times 10^6/m.$
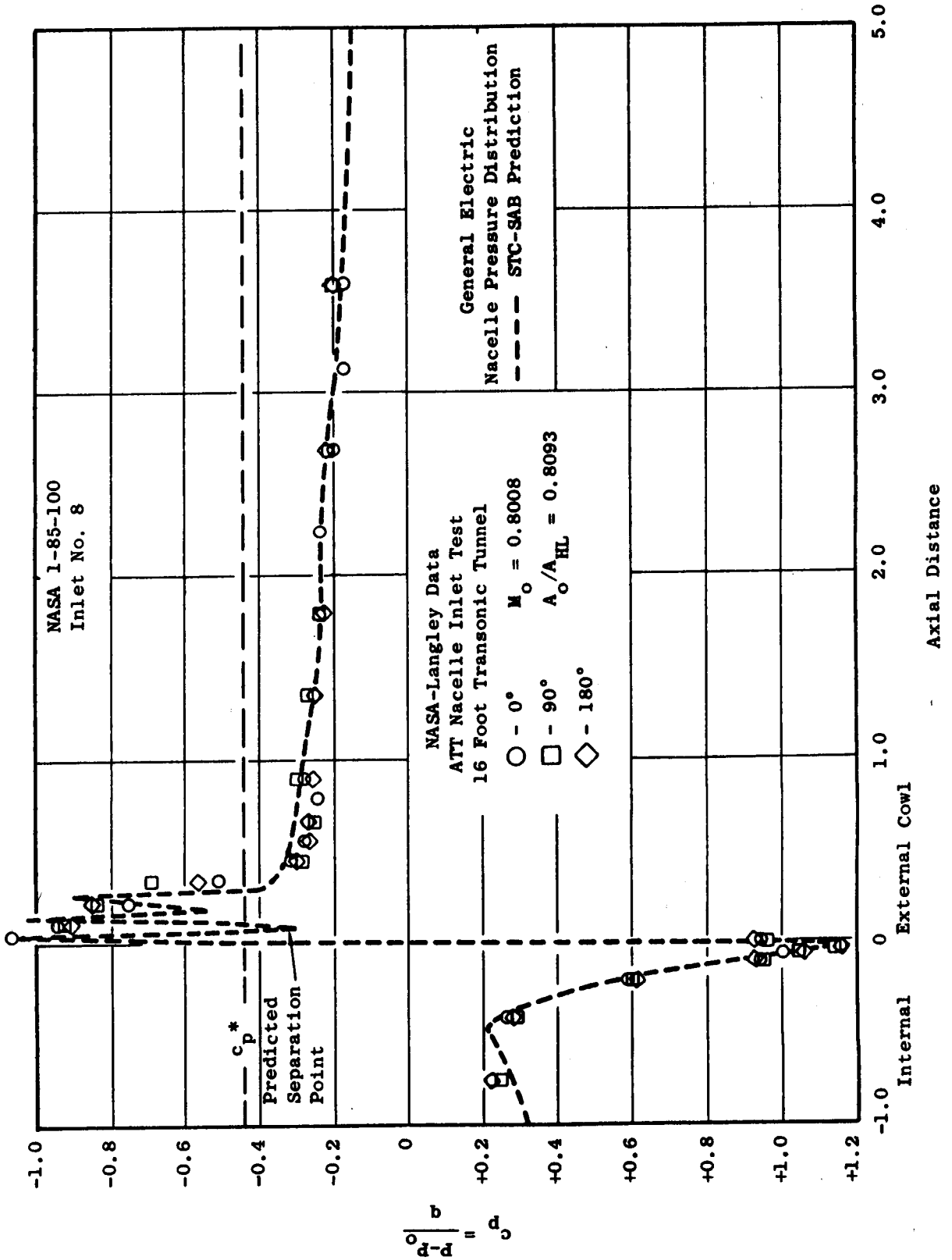
Wedge Angle (α) = $26.96°$

Figure 63. Inlet Pressure Comparison @ M_O = 0.8008.

of the cowl lip, the comparison with test data is excellent and the effects of the boundary layer displacement thickness are not noticeable (see Figure 15). On the external surface, the initial acceleration around the cowl lip is followed by a sharp pressure rise, and incipient separation is predicted. Once the separation point is predicted, the boundary layer displacement thickness becomes a constant from there on (the viscous analysis is not applicable to flow in a separation region or reattachment). The streamtube curvature analysis oscillates in the region where the test data indicate a separation bubble has been formed. When the flow reattaches the predicted pressures and the measured pressures agree very well. Overall, the measured pressure force on the cowl outer surface was $C_{D_P} = -0.039$ and the predicted pressure force was $C_{D_P} = -0.047$.

The predicted and measured cowl pressures are shown in Figure 64, at $M_o = 0.85$ and a mass ratio of 0.81. The trends are very similar to those at $M_o = 0.80$ in that a separation bubble is still present but it is extended. The pressure comparison is very good on the surfaces where attached flow exists.

The NASA No. 8 inlet was analyzed at $M_o = 0.9$ and a mass flow ratio of 0.885 with the viscous effects included. The flow remained attached on the outer cowl surface. On the internal surface, the flow became supersonic locally and then shocked back to subsonic. Again, the comparison between measured and predicted surface pressures is excellent (Figure 65). The overall integrated pressure force on the outer cowl was measured as -0.026 and predicted as -0.031. The streamtube curvature analysis, with viscous effects included, matches the test results more closely than the inviscid analysis alone.

10.3 CONCLUSIONS

The Stratford and Beavers integral boundary layer analysis has been integrated with the Streamtube Curvature inviscid flow analysis. The analysis has been linked so that the inviscid flow field provides the free-stream boundary conditions, including pressure gradients, for the boundary layer analysis. The viscous analysis, in turn, modifies the nacelle geometry for boundary layer displacement thickness effects. The comparisons with test data and another finite difference analysis show that the method is an accurate and reliable predictor of turbulent boundary layers.

The Stratford separation method, modified for compressibility, has been developed to predict incipient separation in the adverse pressure gradient associated with the flow about a nacelle and that associated with embedded shocks. Its validity has been demonstrated by theory to data comparisons for two Reynolds numbers. This combined set of flow analysis methods provides a very useful and reliable engineering analysis tool.
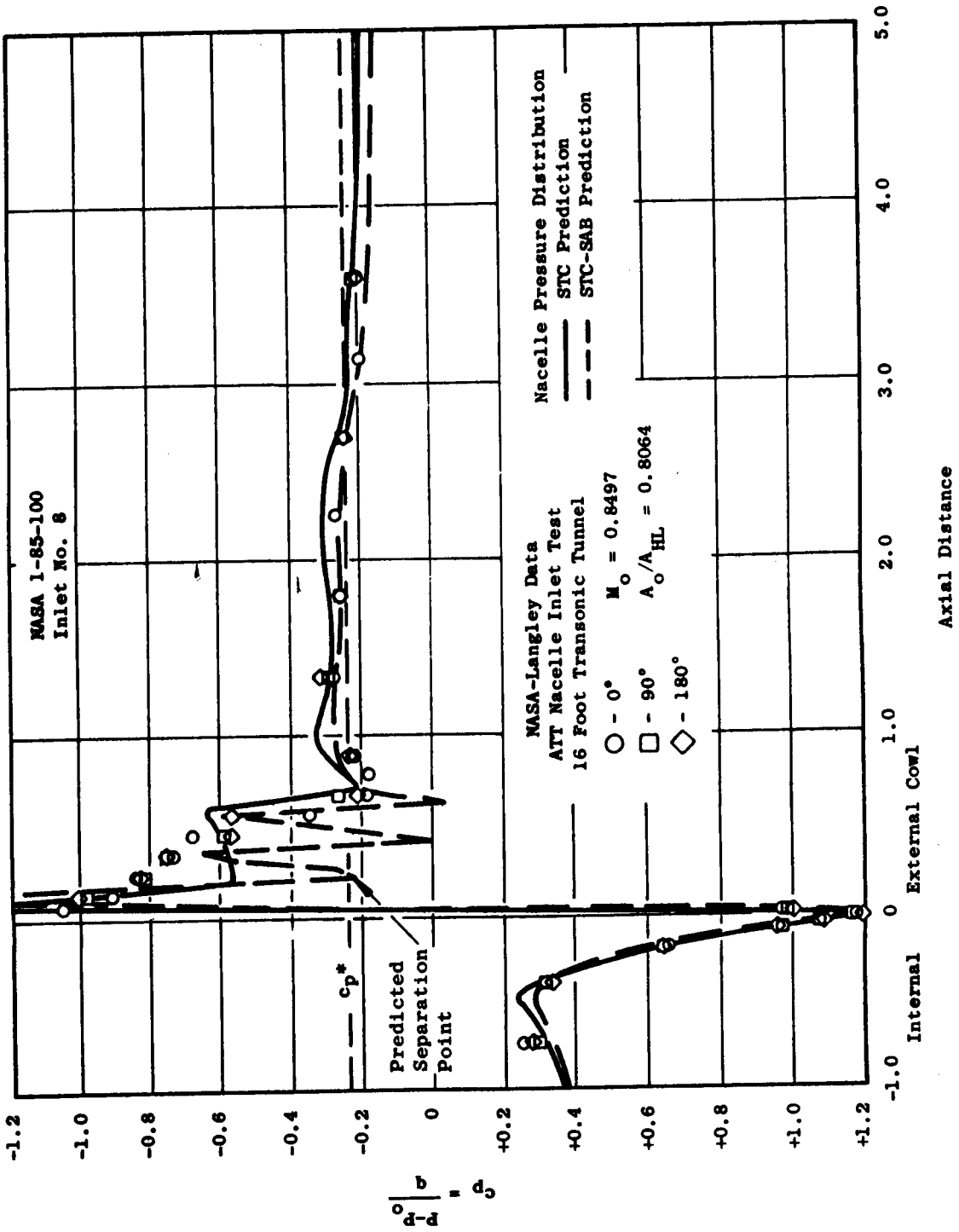
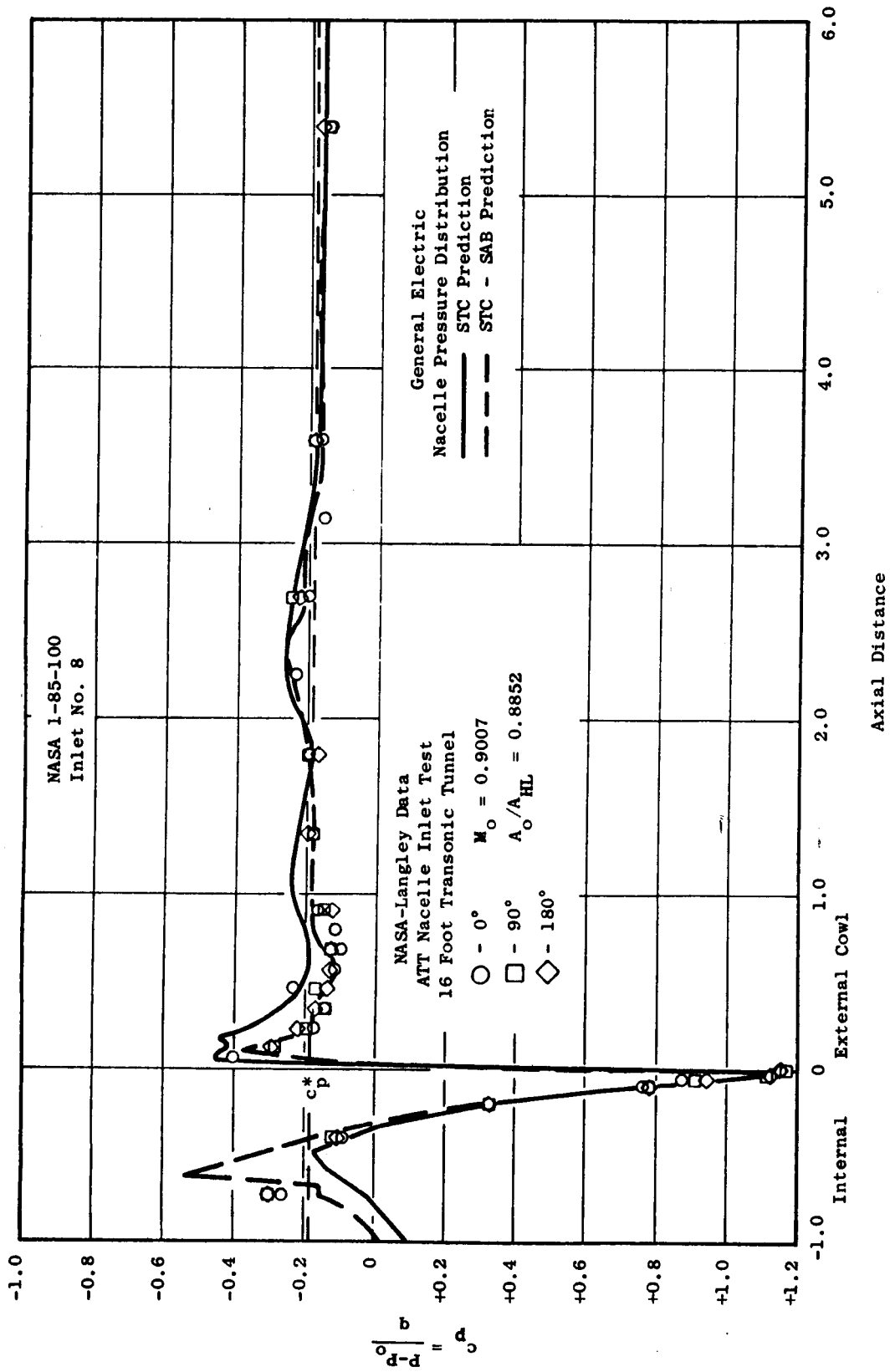Figure 64. Inlet Pressure Comparisons @ $M_O = 0.8497$.

Figure 65. Inlet Pressure Comparisons @ M_O = 0.9007.

10.4   NOMENCLATURE

Symbols	Description
β	Empirical constant
c_f	Skin friction coefficient
c_p	$c_p = 1 - \dfrac{M^2}{M_o^2}$
δ	Boundary layer thickness
$\delta*$	Boundary layer displacement thickness
K	Karman constant; $K = 0.41$
M	Mach number
n	Exponent in power law profile
P	Pressure; also a function of Mach number (see Equation 146)
Ψ	Stream function
r	Radius from centerline
R_{ex}	Reynolds number based on reference velocity and local x
R	Reynolds number based on local velocity and local x
ρ	Density
	Shear stress
θ	Boundary layer momentum thickness
u	Velocity
U	Velocity at outer edge of boundary layer
U_o	Reference velocity
x	Coordinate along wall

X	Equivalent flat plate length
y	Coordinate normal to wall

SUBSCRIPTS

e	Conditions at outer edge
o	Denotes free-stream or reference conditions
T	Stagnation condition

11.0 REFERENCES

1. Murman, E.M. and Cole, J.D., "Calculation of Plane Steady Transonic Flows," AIAA Journal, Vol. 9, No. 1, Jan. 1971, pp. 114-121.

2. Steger, J.L. and Lomax, H., "Transonic Flows About Two-Dimensional Airfoils by Relaxation Procedures," AIAA Journal, Vol. 10, No. 1, Jan. 1972, pp. 49-54.

3. Smith, L.H., Jr., "The Radial-Equilibrium Equation of Turbo-Machinery," Journal of Engineering for Powere, Trans. ASME, Series A, Vol. 88, 1966, pp. 1-12.

4. Novak, R.A., "Streamline Curvature Computing Procedures for Fluid Flow Problems," ASME Paper 66 -- WA/GE-3, 1966.

5. Katsanis, T., "Use of Arbitrary Quasi-Orthogonals for Calculating Flow Distribution in the Meridinal Plane of a Turbomachine," NASA TN D-2546, 1964.

6. Van Dyke, M., "Perturbation Methods in Fluid Mechanics," Vol. VIII of Applied Mathematics and Mechanics, Academic Press, 1964.

7. Smith, A.M.O. and Pierce, J., "Exact Solution of the Neumann Problem. Calculation of Non-Circulatory Plane and Axially Symmetric Flows About or Within Arbitrary Boundaries," Douglas Aircraft Report No. ES 26988, 1958.

8. Hess, J.L. and Smith, A.M.O., "Calculation of Non-Lifting Potential Flow About Arbitrary Three-Dimensional Bodies," Douglas Aircraft Report No. ES 40622, 1962.

9. Oswatitsch, K., "Gas Dynamics," Vol. I of Applied Mathematics and Mechanics, Academic Press, 1956.

10. Krupp, J.A. and Murman, E.M., "The Numerical Calculation of Steady Transonic Flows Past Thin Lifting Airfoils and Slender Bodies," AIAA Preprint No. 71-566, 1971.

11. Spreiter, J.R. and Alksne, A.Y., "Slender-Body Theory Based on Approximate Solution of the Transonic Flow Equation," NASA Technical Report R-2, 1959.

12. Spreiter, J.R. and Alksne, A.Y., "Thin Airfoil Theory Based on Approximate Solution of the Transonic Flow Equations," NACA TN-3970, 1957.

13. Heaslet, M.A. and Spreiter, J.R., "Three-Dimensional Transonic Flow Theory Applied to Slender Bodies and Wings," NACA TN-3717, 1956

14. Peaceman, D.W. and Rachford, D.H., Jr., "The Numerical Solution of the Parabolic and Elliptic Differential Equations," J. Soc, Indust. Appl. Math., Vol. 3, pp. 28-41, 1955.

15. Moeckel, W.E., "Approximate Method for Predicting Form and Location of Detached Shock Waves Ahead of Plane or Axially Symmetric Bodies," NACA TN 1921, July 1949.

16. Keith, J.S., Ferguson, D.R., and Heck, P.H., "Users Manual for Streamtube Curvature Analysis - Analytical Method for Predicting the Pressure Distribution about a Nacelle at Transonic Speeds," NASA CR-112239, General Electric Company.

17. Stratford, B.S. and Beavers, G.S., "The Calculation of the Compressible Turbulent Boundary Layer in an Arbitrary Pressure Gradient - A Correlation of Certain Previous Methods," ARC R&M No. 3207, September 1959.

18. Tucker, M., "Approximate Calculation of Turbulent Boundary Layer Development in Compressible Flow," NACA TN 2337, 1951.

19. Young, A.D., "The Calculation of the Profile Drag of Aerofoils and Bodies of Revolution at Supersonic Speeds College of Aeronautics," Rep. No. 73, ARC 15, 970, 1957.

20. Englert, G.W., "Estimation of Compressible Boundary Layer Growth Over Insulated Surfaces with Pressure Gradient," NACA TN 4022, 1957.

21. Mager, A., "Transformation of the Compressible Turbulent Boundary Layer," Journal of the Aeronautical Sciences, Vol. 25, No. 5, May 1958, pp. 305-311.

22. Reshotko, E., and Tucker, M., "Approximate Calculation of the Compressible Turbulent Boundary Layer with Heat Transfer and Arbitrary Pressure Gradient," NACA TN 4154, 1957.

23. Culick, F.E.C., and Hill, J.A.F., "A Turbulent Analog of the Stewartson-Illingworth Transformation," Journal of the Aerospace Science, Vol. 25, No. 4, pp 259-262, 1958.

24. Michel, R., "Calcul Pratique de la Couche Limite Turbulente Compressible," Principe et Applications, ONERA Note Technique No. 49, 1959.

25. Spence, D.A., "The Growth of Compressible Turbulent Boundary Layers on Isothermal and Adiabatic Walls," ARC R&M No. 3191, 1959.

26. Thwaites, B., "Approximate Calculation of the Laminar Boundary Layer," The Aeronautical Quarterly, Vol. 1, pp. 245-280, November 1959.

27. Beckwith, I.E., and Bushnell, D.M., "Detailed Description and Results of a Method For Computing Mean and Fluctuating Quantities in Turbulent Boundary Layers," NASA TN D-4815, October 1968.

28. Coles, D.E., and Hirst, E.A., "Computation of Turbulent Boundary Layers," 1968 AFOSR-IFP-Stanford Conference, Vol. II, August 1968.

29. Pasiuk, L., Hastings, S.M., and Chatham, R., "Experimental Reynolds Analogy Factor For a Compressible Turbulent Boundary Layer With a Pressure Gradient," Aerodynamics Research Report No. 234, NOLTR 64-200, November 27, 1964.

30. Winter, K.G., Rotta, J.C., and Smith, K.G., "Studies of the Turbulent Boundary Layer on a Waisted Body of Revolution in Subsonic and Supersonic Flow," ARC R&M No. 3633, 1968.

31. Waltrup, P.J., and Schetz, J.A., "An Experimental Investigation of a Supersonic Turbulent Boundary Layer Subjected to a Systematic Variation of Adverse Pressure Gradients," AIAA Paper 72-311, April 1972.

32. Cebici, T., Mosinskis, G.J., and Smith, A.M.O., "Calculation of Viscous Drag and Turbulent Boundary Layer Separation on Two-Dimensional and Axisymmetric Bodies in Incompressible Flows," Report No. MDC J0973-01, November 1970.

33. Stratford, B.S., "The Prediction of Separation of the Turbulent Boundary Layer," Journal of Fluid Mechanics, Vol. 5, Part 1, January 1959.

34. Schubaur, G.B., and Klebanoff, P.S., "Investigation of Separation of the Turbulent Boundary Layer," NACA Report 1030, 1951.

35. Chapman, D.R., Kuehn, D.M., and Larson, H.K., "Investigation of Separated Flows in Supersonic and Subsonic Streams with Emphasis on the Effect of Transition," NACA Report 1356, 1958.

36. Alber, N.E., Bacon, J.W., Masson, B.S., and Collins, D.J., "An Experimental Investigation of Turbulent Transonic Viscous - Inviscid Interactions," AIAA Paper 71-565, June 1971.

37. Seddon, J., "The Flow Produced By Interaction of a Turbulent Boundary Layer with a Normal Shock Wave of Strength Sufficient to Cause Separation," Aeronautical Research Council R&M No. 3502, 1967.

38. Thomke, G.J., and Roshko, A., "Incipient Separation of a Turbulent Boundary Layer at High Reynolds Number in Two-Dimensional Supersonic Flow Over a Compression Corner," NASA CR 73308, January 1969.